ABSTRACT

Title of dissertation: DECOHERENCE AND
DYNAMICAL DECOUPLING IN
SOLID-STATE SPIN QUBITS

Wayne Martin Witzel
Doctor of Philosophy, 2007

Dissertation directed by: Professor Sankar Das Sarma
Department of Physics

This dissertation is a study of the decoherence of a solid-state spin qubit, either that of a localized electron spin or a donor nucleus, caused by a nuclear spin bath relevant to semiconductor quantum computer architectures. In the presence of an external magnetic field and at low temperatures, the dominant decoherence mechanism is the spectral diffusion of the qubit spin resonance frequency due to the temporally fluctuating random magnetic field associated with the dipolar interaction induced flip-flops of nuclear spin pairs. The qubit spin dephasing due to this random magnetic field depends intricately on the quantum dynamics of the nuclear spin bath, making the coupled decoherence problem difficult to solve. We provide a formally exact solution of this non-Markovian quantum decoherence problem which numerically calculates accurate spin decoherence at short times, of particular relevance in solid-state spin quantum computer architectures. A quantum cluster expansion method is motivated, developed, and tested for the spectral diffusion problem. The method is applicable to any ideal pulse sequence applied to the qubit.

Dynamical decoupling sequences, which aim to prolong qubit coherence, are analyzed. In particular, concatenated dynamical decoupling sequences are shown to prolong not only the coherence time over the entire sequence but also the length of time between pulses necessary to maintain coherence. This is shown to result from successive low-order cancellations in applicable perturbative expansions with each level of concatenation. Each cancellation, however, will require the inclusion, in the cluster expansion, of increasingly large clusters to obtain the lowest-order results. These larger clusters in the lowest order often dominate decoherence and therefore invalidate, as being overly optimistic, the pair approximation as a means to study the effect of concatenated dynamical decoupling. We present numerical results from our cluster expansion technique for echoes of single (Hahn), concatenated, and periodic pulse sequences using realistic models of a localized electron in phosphorus doped Si and in a GaAs quantum dot and of a P donor nucleus in Si or GaAs. In the Si:P electron spin decoherence problem, we consider, along with spectral diffusion, the effects of anisotropic hyperfine (AHF) interactions and suggest a technique to suppress electron spin echo envelope modulations (ESEEM), an additional source of decoherence resulting from the AHF interactions. Our calculations for the Si:P Hahn echoes, including the effects of both anisotropic hyperfine interactions and spectral diffusion, are in excellent agreement with experimental results. Our calculations of concatenated pulse sequence echoes offer important predictions for the effectiveness of a promising strategy to preserve qubit coherence in semiconductor quantum computer architectures.

Decoherence and Dynamical Decoupling
in Solid-State Spin Qubits

by

Wayne Martin Witzel

Dissertation submitted to the Faculty of the Graduate School of the
University of Maryland, College Park in partial fulfillment
of the requirements for the degree of
Doctor of Philosophy
2007

Advisory Committee:
Professor Sankar Das Sarma, Chair/Advisor
Professor Christopher Jarzynski
Professor Bei-Lok Hu
Professor Victor Yakovenko
Professor Theodore Einstein
Assistant Professor Victor Galitski

© Copyright by
Wayne Martin Witzel
2007

Dedication

To my mother, Donna Mae Bone Whitney, who instilled in me a curiosity about the physical and metaphysical world.

To my father, John Witzel III, who gave me an appreciation for science and technology and from whom I inherited an ability for logic and problem solving.

And to my beloved wife, Sarah, who brings me much joy and whose love and support during my graduate school years has been greatly appreciated.

Acknowledgements

I appreciate help that I have received from many people in order to accomplish this work. First of all, the Condensed Matter Theory Center (CMTC) has been an enriching environment for my graduate research. I have asked innumerable questions, from mundane to profound, of present and past CMTC post-docs; particularly pestering Donald Priour, Vito Scarola, and Chuanwei Zhang. Everybody has been very helpful and they have often offered profound or useful insight. I have enjoyed many discussions with Wang Kong (James) Tse, Shaffique Adam, and others; over lunch, we would often discuss, share, and offer advice pertaining to our current research or more general life interests and goals. I also enjoy friendships and correspondence with former and affiliated CMTC members such as Magdalena Constantin, Maria Calderon, Belita Koiller, Xuedong Hu, and Rogerio de Sousa. And, of course, my advisor, Sankar Das Sarma, is intricately linked to the enriching atmosphere of CMTC.

This work began from the launch-pad of Rogerio de Sousa's dissertation. He laid out the problem of spectral diffusion in an understandable way that I could pick up and carry forward; his insight into the physical process of spectral diffusion caused by flip-flopping dynamics of nuclear spins in the bath can be considered a prelude to the cluster expansion approach of this work (relating to the lowest order pair approximation). His collaboration and correspondence was crucial to this effort, and he was always asking me tough questions to make me think hard about the problem and force me to clarify my arguments.

I have also received help from members of other research groups; they have taken time to help answer my questions without obligation to do so. Members of Lu Sham's theory group at UC San Diego have been extremely helpful even while doing research in competition with our own; Ren-Bao Liu, Semion Saikin, and, in particular, Wang Yao have all taken time to help me. Experimentalists have also offered much help. Alexei Tyryshkin provided invaluable incite (pointing out the effects of strain, in particular) that has allowed me to match his experimental results so beautifully. Jason Petta was also very willing to entertain my questions regarding his experiments in double quantum dots in GaAs.

I must also acknowledge ARO, ARDA, and DTO for their generous QuaCGR (quantum computing graduate student) fellowship and LPS-NSA for their support. In addition, I appreciate the opportunity that I have had, as a QuaCGR, to attend their annual Quantum Computing Program Review meetings which were informative and helpful in terms of networking with people and sharing ideas in the field of quantum computation.

Finally, I also appreciate the love and support from family and friends. I have been fortunate in my life to be surrounded by many who have believed in my potential. Thank you.

Table of Contents

List of Tables vii

List of Figures viii

List of Abbreviations x

1 Introduction 1
  - 1.1 Quantum Computation 4
  - 1.2 Reduced Density Matrices and Decoherence 6
  - 1.3 Geometrical Representation of a Single Qubit 8
  - 1.4 Dynamical Decoupling 11
  - 1.5 Outline of the Dissertation 14

2 Background 16
  - 2.1 Solid State Qubit in a Spin Bath 16
  - 2.2 The Spectral Diffusion Problem 19
    - 2.2.1 Stochastic Theories 20
    - 2.2.2 Non-Markovian Quantum Theory 21

3 The Qubit, the Bath, and Control Pulses 25
  - 3.1 General Free Evolution Hamiltonian 25
  - 3.2 Types of Interactions (Energies) 27
    - 3.2.1 Zeeman 28
    - 3.2.2 Dipolar (Secular and Non-secular) 29
    - 3.2.3 Hyperfine (Contact and Anisotropic) 30
    - 3.2.4 Hyperfine-mediated (RKKY) 32
    - 3.2.5 Indirect Exchange 34
    - 3.2.6 Summary of Interactions 35
  - 3.3 The Decoherence Problem Given a Pulse Sequence 37

4 The Cluster Expansion 41
  - 4.1 Conceptual cluster expansion 42
  - 4.2 Initial Justification in Terms of Perturbation Theories 46
  - 4.3 Decoherence Via Cluster Contributions 48
    - 4.3.1 Decomposing into Cluster Contributions 49
    - 4.3.2 Ideal cluster expansion 53
    - 4.3.3 Practical implementation of the cluster expansion 55
  - 4.4 Cluster Expansion in Summary 60

5 Pulse Sequences for Dynamical Decoupling 63
  - 5.1 Concatenated Dynamical Decoupling 65
    - 5.1.1 Eliminating Successive Perturbative Orders 67
    - 5.1.2 Time Perturbation 69

5.1.3 Intra-bath Perturbation 71
5.1.4 Magnus Expansion 74
5.2 Periodic Dynamical Decoupling (e.g. CPMG) 76

6 Applications in Specific Systems 78
6.1 Phosphorus Donor in Silicon 79
6.1.1 Hahn echo spectral diffusion 81
6.1.2 Cluster expansion convergence 86
6.1.3 Anisotropic hyperfine modulations and comparison with experiment 93
6.1.3.1 Remarkable agreement with experiment 97
6.1.3.2 Suppressing anisotropic hyperfine modulations 101
6.2 Gallium Arsenide Quantum Dots 107
6.2.1 Hahn echo spectral diffusion 109
6.2.2 Cluster expansion convergence 114
6.2.3 Experiments in GaAs 116
6.3 Periodic and concatenated dynamical decoupling 119
6.4 Nuclear Spin Memory 125

7 Conclusion 135
7.1 Discussion 136
7.2 Future Work 139

Bibliography 142

List of Tables

3.1 Interactions and estimated energy scales 36

List of Figures

1.1 Bloch sphere represention of a single qubit in a pure state. 9

1.2 Dephasing decoherence of a Bloch sphere. 10

1.3 Hahn echo pulse sequence. 12

1.4 Pulse sequence for the Carr-Purcell-Meiboom-Gill (CPMG) experiment and resulting echoes. 13

2.1 Schematic for the spectral diffusion of a donor electron spin in Si:P. . 17

4.1 Processes in a nuclear spin bath. 42

4.2 Near (not nearest) neighbor approximation and definition of L. 44

4.3 Clusters of nuclei connected by interactions. 46

4.4 Graphical representation of terms in a cluster decomposition. 51

4.5 Graphical representation of one possible term in a pair approximation. 55

4.6 Overlapping pairs (2-clusters). 59

6.1 Theoretical and experimental comparison of the Hahn echo decay for a bound electron in Si:P. 82

6.2 Theoretical Hahn echo decay for a bound electron in Si:P as a function of the isotopic fraction, f, of ^{29}Si. 85

6.3 Estimated errors of the calculated Si:P electron Hahn echo decay due to overlapping clusters. 87

6.4 Successive contributions to the cluster expansion for the Si:P electron spin Hahn echo for 100% ^{29}Si. 89

6.5 Successive contributions to the cluster expansion for the Si:P electron spin Hahn echo for natural Si. 91

6.6 AHF-induced ESEEM in Si:P fit to the Hahn echo decay experiment for one particular applied magnetic field direction. 98

6.7 AHF-induced ESEEM in Si:P compared to Hahn echo decay experiments at different magnetic field angles with two fitting parameters per curve. 99

6.8 Comparison between the spectral diffusion fitting parameters of Fig. 6.7 and the theoretical predictions of Sec. 6.1.1. 100

6.9 Calculated maximum AHF-induced ESEEM modulations in natural Si as a function of applied magnetic field strength. 103

6.10 Special applied magnetic field directions that allow effective removal of ESEEM induced by AHF-interactions with the nearest P donor neighbors. 105

6.11 Calculated Si:P ESEEM as a function of τ showing periodic suppression due to decoupling from the nearest P donor neighbors. 106

6.12 Theoretical Hahn echo decay times for GaAs quantum dots of various sizes. 111

6.13 Theoretical Hahn echo decay times for GaAs quantum dots including and excluding indirect exchange interactions. 113

6.14 Successive contributions to the cluster expansion for the GaAs quantum dot spin Hahn echoes. 115

6.15 Theoretical periodic and concatenated pulse sequence echoes of a donor electron in Si:P. 120

6.16 Contributions to concatenated pulse sequence echoes of a donor electron in Si:P from different-sized clusters. 121

6.17 Theoretical periodic and concatenated pulse sequence echoes in GaAs quantum dots. 123

6.18 Contributions to concatenated pulse sequence echoes of a GaAs quantum dot from different-sized clusters. 124

6.19 Theoretical nuclear spin echo decay of a P donor nucleus in GaAs. . . 129

6.20 Theoretical nuclear spin echo decay of a P donor nucleus in natural Si. 131

6.21 Theoretical nuclear spin echo decay of a P donor nucleus in 100% pure ^{29}Si. 132

List of Symbols and Abbreviations

qubit	quantum bit.
SD	Spectral Diffusion, dephasing decoherence in a spin bath.
NMR	Nuclear magnetic resonance.
ESR	Electron spin resonance.
FID	Free induction decay.
DD	Dynamical Decoupling.
CDD	Concatenated Dynamical Decoupling.
CDD#	CDD with # levels of concatenation.
CPMG	Carr-Purcell-Meiboom-Gill; a periodic pulse sequence.
Si:P	Phosphorus-doped silicon.
GaAs	Gallium Arsenide.
$\hat{\boldsymbol{S}}$	Vector of x, y, and z electron spin operators.
$\hat{\boldsymbol{I}}$	Vector of x, y, and z nuclear spin operators.
$\hat{\mathcal{H}}_\pm$	Bath Hamiltonian given an up/down qubit, $\hat{\mathcal{H}}_\pm = \pm\hat{\mathcal{H}}_{qb} + \hat{\mathcal{H}}_b$.
$\hat{\mathcal{H}}_{qb}$	Defines qubit-bath interactions as $\hat{\mathcal{H}}_{qb} \otimes \hat{S}_z$.
$\hat{\mathcal{H}}_b$	Bath-only Hamiltonian, $\hat{\mathcal{H}}_b = \hat{\mathcal{H}}_{b0} + \epsilon\hat{\mathcal{H}}_{bb}$.
$\hat{\mathcal{H}}_{b0}$	Independent energies of nuclei in the bath (e.g., Zeeman).
$\hat{\mathcal{H}}_{bb}$	Hamiltonian of intra-bath interactions.
ϵ	Bookkeeping parameter counting intra-bath interactions.
$\hat{\mathcal{H}}_e^Z$	Zeeman energy of an electron.
$\hat{\mathcal{H}}_n^Z$	Zeeman energy of nucleus n.
$\hat{\mathcal{H}}_{nm}^D$	Dipolar interaction Hamiltonian between nuclei n and m.
b_{nm}	Coupling constant of intra-bath interactions.
HF	Hyperfine; interactions between spins of an electron and nucleus.
AHF	Anisotropic hyperfine.
$\hat{\mathcal{H}}_n^{HF}$	HF interaction Hamiltonian between the electron and nucleus n.
A_n	HF coupling constant between the electron and nucleus n.
$\hat{U}^\pm$	Evolution operator given an qubit spin initially up, $+$, or down $-$.
$\hat{U}_0^\pm(t)$	Free evolution for a time t with the qubit up, $+$, or down, $-$.
τ	Default time between pulses, $\hat{U}_0^\pm \equiv \hat{U}_0^\pm(\tau)$.
$\hat{W}$	$\hat{W} = \left[\hat{U}^-\right]^\dagger \hat{U}^+$.
$\langle\hat{W}\rangle$	Statistical average of $\hat{W}$ over initial bath states.
v_E	Echo of a generic pulse sequence, $v_E = \left\Vert\langle\hat{W}\rangle\right\Vert$.
v_{Hahn}	v_E for the Hahn echo sequence with $\hat{U}^\pm = \hat{U}^\pm_{\text{Hahn}} = \hat{U}_0^\mp(\tau)\hat{U}_0^\pm(\tau)$.
v_{CDD}	v_E for the CDD sequence; $\hat{U}^\pm = \hat{U}_l^\pm = \hat{U}_{l-1}^\mp\hat{U}_{l-1}^\pm$.
v_{CPMG}	v_E for the CPMG sequence; $\hat{U}^\pm = \left[\hat{U}_2^\pm\right]^\nu$ with 2ν pulses.
$\langle\hat{W}_{\mathcal{S}}\rangle$	$\langle\hat{W}\rangle$ when only considering nuclei in set S.
$\langle\hat{W}'_{\mathcal{C}}\rangle$	Cluster contribution from cluster $\mathcal{C}$.

L	Number of significantly interacting neighbors in the bath.
λ	General perturbation parameter (either τ or ϵ).
Σ_j	Sum of all cluster contributions of size j.
Σ_2^*, Σ_3^*	Overlapping pair corrections in the cluster expansion.
$\hat{V}$	Perturbation Hamiltonian, $\hat{V} = \epsilon\hat{\mathcal{H}}_{bb}$.
ESEEM	Electron spin echo envelope modulations

Chapter 1

Introduction

In order to motivate our work on decoherence, relevant to quantum computation and quantum information in general, we begin with a brief discussion of the difference between classical and quantum information. Classical information is represented by a sequence of ones and zeroes, each known as a bit. Today's digital computers process these bits using binary logic and the result is quite powerful. According to the quantum theory of physics, however, nature somehow stores information in a much richer, qualitatively different sense. The elements of quantum information are called qubits (quantum bits) and can represent a superposition (a mixture) of both zero and one. More importantly, multiple qubits, stored in the states of different subatomic particles for example, can become entangled so that their superposition states are interdependent; that is, the state of the system can be an arbitrary superposition of various possible system states in such a way that may not be factorable into individual qubit states. This will be explained in more detail in Sec. 1.1. The important consequence of entanglement for quantum information theory is that the potential information storage and processing of a quantum system grows exponentially with the number of qubits (as opposed to linearly, by definition, for classical bits).

Entanglement is, however, a double-edged sword. While it offers the potential for exponential scaling of information, entanglement - with an uncontrolled environment - causes quantum systems to lose coherent relationships among the superposition states. This process is called decoherence. Strictly speaking, quantum theory dictates that the quantum superposition and entanglement persists in the larger system that includes the environment; however, the information of the environment is assumed to be inaccessible due to its complexity so that the effect is a loss of quantum information.

Decoherence is inevitable, particularly in a complex environment that would be required in a quantum computer (a machine that would exploit the aforementioned exponential scaling of quantum information for computational tasks). On the other hand, quantum error correction [2] may be employed to allow arbitrarily long quantum computations in the presence of decoherence as long as the number of possible coherent quantum operations in a sequence (generally with some parallelism) is above some threshold (this threshold depends on the specific quantum computing architecture under investigation as well as theoretical assumptions made in the estimate but is usually in the range of 10^4 to 10^6 coherent operations [3]). This threshold is fairly stringent, and it therefore important to thoroughly study decoherence in specific systems that hold promise for quantum computation if the lofty goal of building a quantum computer is to be realized.

In this work, we study the decoherence of a solid-state spin quantum bit caused by its interaction with a bath of nuclear spins. Solid-state semiconductors have been extremely valuable in the digital revolution of classical computers because of their scalability (i.e., the vast number of transistors that can be produced per square inch surface of a computer chip). The solid-state environment also holds promise for quantum information processing and other promising spintronics applications [1]. Furthermore, spin coherence times are expected to be long ($\gtrsim$ μs) compared with charge coherence times ($\lesssim$ ns) in solids. At achievable mK temperatures, phonons in solids are frozen out. However, such temperatures are very high compared to the nK energy scale (relative to Boltzmann's constant) of dipolar interactions among nuclear spins (justifying a random-bath treatment for this environment). With this motivation, we study the decoherence induced by a nuclear spin bath in solid state materials for the candidate qubits of either a localized electron spin or central nuclear spin.

The important achievement of this work is our ability to computationally study nuclear spin bath-induced decoherence with a fully quantum mechanical, microscopic theory. It is truly remarkable that this is even possible since the state space of such a spin bath grows exponential with the number of spins (another consequence of the exponential scaling of quantum information). However, we have devised a prescription for decomposing such a problem into sub-problems that involve clusters of few nuclear spins, and an expansion that converges (in many relevant regimes) as we successively include contributions from clusters with increasing numbers of nuclei. In this way, we can study the rate of decoherence in various solid state environments as well as the effect of sequences of pulses (that manipulate the qubit at prescribed times) designed to decouple the qubit from the bath and prolong coherence.

1.1 Quantum Computation

A quantum computer is a machine that would exploit the exponential scaling, with the number of qubits, of quantum information. It is not as straight-forward as simply accessing this exponentially scaled information. The inputs and outputs of the machine must be classical, ones and zeroes, because this is all we, as macroscopic beings, can have access to directly. A quantum computer is still more powerful than a classical computer because in the interim between the classical input and output states, it may traverse the vast, exponentially expanded, quantum state space (Hilbert space). To make this mathematically concrete, we can think of the quantum computer as mapping classical inputs into a quantum state through a unitary (linear and normalization-preserving) transformation; such a transformation may be used to describe the time evolution of any quantum system. With N qubits, the input may be any one of 2^N possible bit sequences. The unitary transformation, $\hat{U}$, may be represented, using the classical states as basis states, by any $2^N \times 2^N$ complex-valued matrix such that $\hat{U}^\dagger \hat{U} = \hat{\mathbb{1}}$ (the superscript $\dagger$ indicates the adjoint operation or the transpose and complex conjugate of the matrix) so that the normalization of the transformed vector is preserved. The resulting quantum state can be any linear combination (superposition) of classical states with complex coefficients. The classical output is determined probabilistically with probabilities determined as the squared modulus of the complex coefficient for each corresponding classical state in the linear combination. In mathematical terms, a classical input, $|n\rangle$ (where n is one of 2^N possibilities) is transformed into a quantum state

$$|\psi\rangle = \hat{U}|n\rangle = \sum_m c_m|m\rangle, \tag{1.1}$$

where the c_m are complex coefficients of a representation of $|\psi\rangle$ as a linear combination of classical basis states, $|m\rangle$. The probability of the quantum computer producing an output of $|m\rangle$ is simply $P_m = \|c_m\|^2$.

This unitary transformation, $\hat{U}$, is the engine of the quantum computation and may be generated with quantum logic gates that operate on one or two qubits. Only a small set of these logic gates are necessary in order to generate any arbitrary unitary transformation; for example, universal quantum computation may be accomplished by performing the controlled-not two-qubit logic gate in addition to arbitrary single-qubit (rotation) gates [4]. An alternative approach to quantum computation that does not use logic gates is to manipulate the system of qubits into a highly entangled "cluster" state and then perform a sequence of measurements, each chosen based upon previous measurements [5]. The effect is the same, and which strategy to use will depend upon what is convenient to implement for a given physical system.

Although we can not have direct access to the exponentially scaled quantum information, a quantum computer can be much more powerful than a classical computer for solving certain problems. A quantum computer can factorize numbers with exponential speedup [6] (with respect to the number of bits in the number to be factorized) over a classical computer. It could also perform certain search tasks with a $\sqrt{n}$ (n being the number of objects in the search space) [7] improvement over a classical computer. A quantum computer would also be naturally useful to perform quantum mechanics simulations [8]. These applications, in addition to more recently discovered quantum algorithms [9], give ample justification for pursuing the goal of building an actual quantum computer.

1.2 Reduced Density Matrices and Decoherence

The potential information content of a quantum mechanical system is greater than the sum of the information content in its individual parts. This statement comes as a trivial corollary to the observation that quantum information scales exponentially with the number of qubits due to the possibility of entanglement. It is therefore not possible, even in principle, to ascribe a quantum state to part of a quantum system if it is entangled with another part of the system because, in a manner of speaking, there is information contained by the entanglement itself (not contained in either part independently). It is often desirable, however, to know as much as possible about part of a quantum system without caring about the rest, to which it may be entangled. For example, we want to study a quantum system (e.g., a collection of qubits in a quantum computer) that interacts with a large, complex bath, and we wish to study the effects of the interaction with the bath (i.e., decoherence) without caring about the state of the bath itself except to the extent that it affects the decoherence of the qubit. We can represent the incomplete information we have about the quantum system without regard to the bath by using a reduced density matrix.

A density matrix simply represents a probability distribution over all possible quantum mechanical states. For example, if, as far as we can say, a quantum system is in state $|\psi_j\rangle$ with probability P_j for some set of j's exhausting all possibilities, then we write the density matrix of this system as

$$\hat{\rho} = \sum_j P_j |\psi_j\rangle\langle\psi_j|, \tag{1.2}$$

where each $|\psi_j\rangle\langle\psi_j|$ is an outer vector product forming a second rank tensor. With $\langle n|\psi\rangle$ representing the projection of vector (state) $|\psi\rangle$ onto $|n\rangle$ (an inner product) and $\langle\psi|n\rangle$ its complex conjugate, we may extract the matrix elements of $\hat{\rho}$ via $\rho_{nm} = \langle n|\hat{\rho}|m\rangle$. If the state of the system is known with certainty, then the density matrix, of the form $\hat{\rho} = |\psi\rangle\langle\psi|$, is said to represent a pure state; otherwise, it is said to represent a mixed state [4].

Suppose we represent the initial state of our quantum system of interest combined with the bath as $\hat{\rho}_0$ in the general form of Eq. (1.2). For any quantum mechanical system, evolution through time can be defined by a unitary transformation map, $|\psi(t)\rangle = \hat{U}(t)|\psi_0\rangle$. It follows, then, from the form of Eq. (1.2) that

$$\hat{\rho}(t) = \hat{U}\hat{\rho}_0\hat{U}^\dagger. \tag{1.3}$$

This density matrix for the entire system that includes the bath contains much more information than we want or need and is in general immensely complicated. Instead, we want to work with a reduced density matrix that gives a probability distribution for the possible states of the quantum system without regard to the final state of the bath. This is done by tracing out the degrees of freedom of the bath using an operation called the partial trace. That is, given systems A and B, the reduced density matrix for system A is obtained from the combined density matrix using

$$\hat{\rho}_A = \mathrm{Tr}_B\,(\hat{\rho}_{AB}), \tag{1.4}$$

where the partial trace is defined by

$$\mathrm{Tr}_B\,(|a_1\rangle\langle a_2| \otimes |b_1\rangle\langle b_2|) = |a_1\rangle\langle a_2|\,\mathrm{Tr}\,(|b_1\rangle\langle b_2|), \tag{1.5}$$

for any states $|a_{1,2}\rangle$ of system A and any states $|b_{1,2}\rangle$ of system B [4]. Considering, again, our system interacting with a bath, our system may start out in a pure state independent from the bath such that $\hat{\rho}_0 = \hat{\rho}_S \otimes \hat{\rho}_B$ (with subscripts S and B for system and bath respectively), but if the system and bath become entangled through the evolution, $\hat{U}$, then the reduced density matrix of the system, $\mathrm{Tr}_B\,\{\hat{\rho}(t)\}$, will become a mixed state. The pure state becoming a mixed states through its interactions with a bath is the hallmark of decoherence and represents a loss of quantum information in the non-isolated system.

1.3 Geometrical Representation of a Single Qubit

A qubit is defined as a two-level quantum system. Given $|0\rangle$ and $|1\rangle$ as basis states, its quantum state may be any linear combination of these with complex coefficients, $|\psi\rangle = \alpha|0\rangle + \beta|1\rangle$, normalized such that $\langle\psi|\psi\rangle = 1 \Rightarrow \|\alpha\|^2 + \|\beta\|^2 = 1$. The overall complex phase of the state carries no physical meaning, but the relative phase between the two states is relevant in terms of quantum information. Thus,

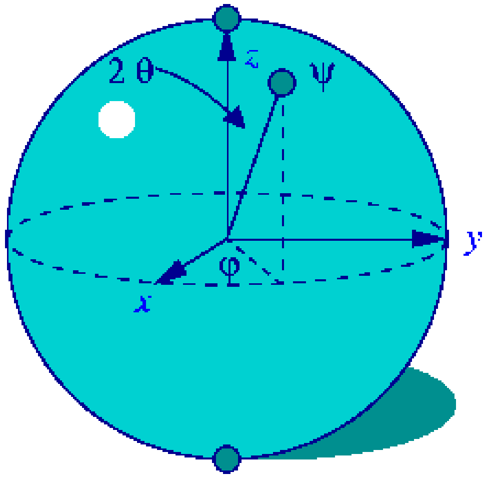

Figure 1.1: Source: www.wikipedia.org. Bloch sphere represention of a single qubit in a pure state.

we may write the general state of a qubit as,

$$|\psi\rangle = \cos\frac{\theta}{2}|0\rangle + e^{i\phi}\sin\frac{\theta}{2}|1\rangle. \tag{1.6}$$

The state is thus defined by two angles θ and ϕ which may be represented by a point on a sphere [Fig. 1.1]. The representation is conventionally called the Bloch sphere.

Subatomic particles with a spin of 1/2, such as an electron, are natural qubits in their spin degree of freedom. The spin state of such a particle may be any linear combination of up or down (with respect to any desired or convenient axis which is conventionally labelled as the z axis). We use $|0\rangle \equiv |\downarrow\rangle \equiv |-\rangle$ interchangeably to represent the down state and $|1\rangle \equiv |\uparrow\rangle \equiv |+\rangle$ to represent the up state. The point on the Bloch sphere that represents the state of this qubit may be literally interpreted as the direction of the spin.

Using the density matrix representation for a single qubit, allowing for mixed

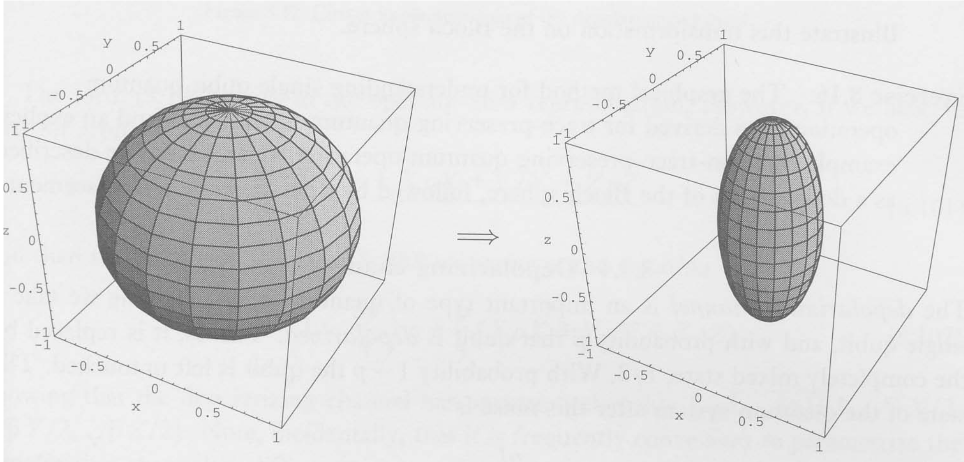

Figure 1.2: Source: M.A. Nielsen and I.L. Chuang, pg. 377, *Quantum Computation and Quantum Information* (Cambridge University Press, Cambridge, U.K., 2000). Dephasing decoherence maps a Bloch sphere into a form with reduced x and y components.

states as well as pure states, we may write

$$\hat{\rho} = \frac{1}{2}\begin{bmatrix} 1 + r_z & r_x - ir_y \\ r_x + ir_y & 1 - r_z \end{bmatrix}, \tag{1.7}$$

where $\vec{r} = (r_x, r_y, r_z)$ is a real-valued vector called the Bloch vector. For pure states, the vector has a length of one and is the point on the Bloch sphere representative of the state. For mixed states, it has a shorter length so that it lies within the Bloch sphere. For a spin-1/2 particle, this vector represents the expectation value of the spin. We can quantify the decoherence of an initially pure state according to the length of the Bloch vector corresponding to the reduced density matrix after the qubit and bath evolve. We can think of the decoherence of an arbitrary qubit state as a map of the Bloch sphere onto a surface within the Bloch sphere. Figure 1.2 shows how depolarization (decoherence processes that can flip the spin) and dephasing (decoherence processes that can change the relative phase, ϕ, of the up and down states) affect the Bloch sphere [4]. Using the nomenclature [10] of the literature, T_1 is a characteristic depolarization time while T_2 is a characteristic dephasing time for a qubit interacting with a bath.

1.4 Dynamical Decoupling

Quantum information in a system coupled to a bath may be preserved, to some extent, by applying rapid control pulses to the system of interest in order to decouple the system from the bath; typically the control is done with electromagnetic pulses that use spin resonance to “target” desired spins. Such techniques have developed over many (∼fifty) years in the field of nuclear magnetic resonance where there is a strong demand for precise spectroscopy of complex molecules [11, 12, 13]. Dynamical decoupling (DD) via pulse sequences has taken on a new role more recently in the context of quantum computing [14, 15, 17, 18, 19, 20, 16, 21].

In the simplest case, a Hahn echo [22] is observed by applying a π-rotation pulse to an ensemble of spins, about an axis perpendicular to a strong applied magnetic field, midway through the evolution; this is illustrated in Fig. 1.3. The strong applied magnetic field suppresses depolarization of the spins, so they only decohere via dephasing. The Hahn echo will recover a signal from an ensemble of spins that precess at different frequencies due to an inhomogeneous magnetic field (this dephasing is known as inhomogeneous broadening). That is, an ensemble of

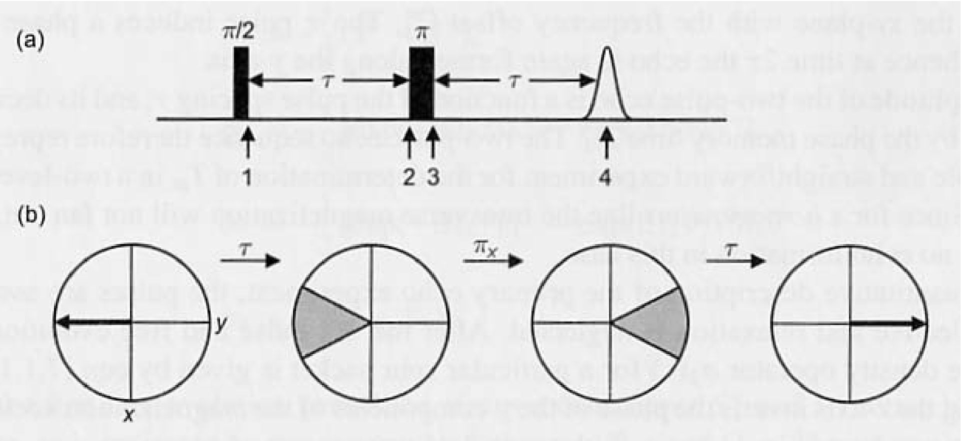

Figure 1.3: Source: A. Schweiger and G. Jeschke, pg. 183, *Principles of Pulse Electron Paramagnetic Resonance* (Oxford University Press, Oxford, NY, 2001). (a) Pulse sequence for the Hahn echo experiment including a $\pi/2$ pulse for initialization (not relevant in DD purposes). Numbers 1, 2, 3, and 4 label points in time shown in diagram (b); (b) In a typical experiment, after the spins relax to lie along an applied field, they are rotated by $\pi/2$ to lie perpendicular to the applied field [1], the ensemble of spins dephase via inhomogeneous broadening after waiting for a time τ [2], the spins are then rotated by π about an axis perpendicular to the applied field [3], the spins finally refocus after waiting again for time τ [4] resulting in the "echo" signal.

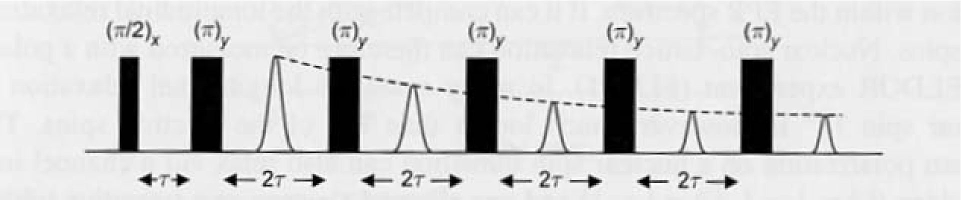

Figure 1.4: Source: A. Schweiger and G. Jeschke, pg. 229, *Principles of Pulse Electron Paramagnetic Resonance* (Oxford University Press, Oxford, NY, 2001). Pulse sequence for the Carr-Purcell-Meiboom-Gill (CPMG) experiment and resulting echoes including a $\pi/2$ pulse for initialization (not relevant in DD purposes).

spins that are initially in phase, with the same ϕ using notation of Sec. 1.3, will go out of phase, at a characteristic time-scale denoted [10] as T_2^*, because they experience different effective magnetic fields. The π-pulse of the Hahn echo will reverse the effect of the local magnetic fields and bring the spins back into phase. With static, inhomogeneous magnetic fields, there is no real decoherence that we are recovering from (the spins are not entangling with a bath); the qubits individually maintain coherence but dephase relative to each other in a way that is easily remedied with the Hahn echo.

If the qubits, on the other hand, interact with a dynamical bath, the Hahn echo also serves to partially decouple each qubit from its respective bath. It does this because the effective interaction Hamiltonian averages out to zero over the duration of the sequence (the first half before the π pulse is opposite that of the second half). This leads to a cancellation of the first order of a Magnus expansion [23] of the system's evolution operator and is the basis for DD schemes used in NMR and proposed for quantum computation [13]. If the bath causes depolarization as well as dephasing, the WAHUHA-4 sequence [24], which applies π-pulses about alternating directions, may be used for DD. Periodic sequences, such as the Carr-Purcell-Meiboom-Gill [25] sequence, illustrated in Fig. 1.4, are used in NMR and known as the "bang-bang" control in quantum information literature [14]; these sequences prolong overall coherence times with repetitions that are faster than the dynamics of the decoherence process. Concatenated sequences [18, 19], with a recursive structure, can do better by successively decoupling the system from the bath to higher perturbative orders as will be discussed in Ch. 5.

1.5 Outline of the Dissertation

In this introduction, we have presented basic concepts about the problem of decoherence as it pertains to quantum computation, and explained why the advent of a quantum computer would hold so much promise. In Ch. 2 we describe the class of qubit decoherence problems (that of solid-state spin qubits) for consideration in this dissertation and present some historical background. In Ch. 3 we concretely formulate the decoherence problems by specifying the various qubit-bath and bath-bath interactions and discuss how we treat applied pulse sequences. Chapter 4 formulates our cluster expansion that will, quite remarkably, allow us to solve problems involving mesoscopic baths with full quantum mechanical rigor. Chapter 5 discusses specific pulse sequences that we may apply as a control to the qubit in order to decouple the qubit from the bath and prolong qubit coherence. In Ch. 6, we present and describe results of applying our developed formalism and techniques to some specific physical systems. We give concluding remarks in Ch. 7 and discuss possible future work.

Chapter 2

Background

In this chapter, we describe the type of decoherence problem being consider in this dissertation, and we provide some historical background of the literature pertaining to this problem. We consider a qubit represented by the spin of a localized electron in a solid or by the spin of a donor nucleus in a solid. For now, we describe the problem in terms of a localized electron spin qubit but nuclear spins have also been proposed [26, 27, 28] for quantum memory storage and will be discussed later in Sec. 6.4 where we demonstrate applications to specific systems. In Sec. 2.1, we discuss the environment of a localized electron spin qubit in a solid state material at low temperature (required to have any hope of implementing a solid state spin quantum computer) and with a strong applied magnetic field that will suppress longitudinal decoherence (e.g., decay in the z direction of the Bloch sphere). In Sec. 2.2, we discuss some of the history in the study of decoherence for this system; the applicable decoherence mechanism is known as spectral diffusion (SD).

2.1 Solid State Qubit in a Spin Bath

The spin decoherence mechanism known as spectral diffusion (SD) has a long history [29, 30, 31, 32, 33, 34], and has been much-studied recently [35, 36, 37, 38, 39, 40, 41, 42, 43, 44, 45] in the context of spin qubit decoherence. To provide a physical

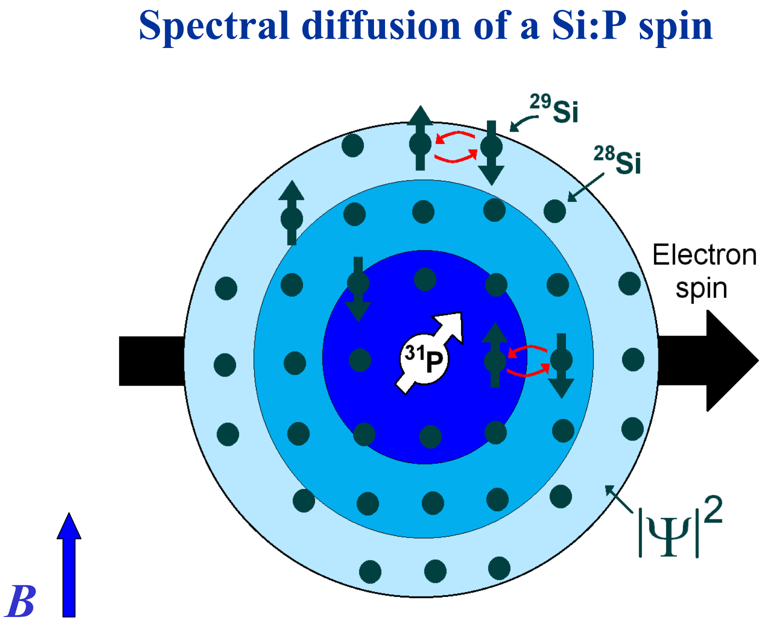
Spectral diffusion of a Si:P spin
^{29}Si
^{28}Si
Electron spin
^{31}P
$|\Psi|^2$
B

Figure 2.1: The electron of a P donor in Si experiences spectral diffusion due to the spin dynamics of the enveloped bath of Si nuclei. Of the naturally occurring isotopes of Si, only ^{29}Si has a net nuclear spin which may contribute to spectral diffusion by flip-flopping with nearby ^{29}Si. Natural Si contains about 5% ^{29}Si or less through isotopic purification. Isotopic purification or nuclear polarization will suppress spectral diffusion in Si.

picture for the theory to be presented in this dissertation we start by considering a localized electron in a solid, for example, a donor-bound electron in a semiconductor as in the doped Si:P system. Such a Si:P system is the basis of the Kane quantum computer architecture [26] although this architecture exploits the P donor nucleus for quantum information storage as well as the donor electron spin and our current focus is the electron spin qubit. The electron spin could decohere through a number of mechanisms. In particular, spin relaxation would occur via phonon or impurity scattering in the presence of spin-orbit coupling, but these relaxation processes are strongly suppressed in localized systems and can be arbitrarily reduced by lowering the temperature. In the dilute doping regime of interest in quantum computation, where the localized electron spins are well-separated spatially, direct magnetic dipolar interaction between the electrons themselves is not an important dephasing mechanism [46]. Interaction between the electron spin and the nuclear spin bath is therefore the important decoherence mechanism at low temperatures and for localized electron spins. Now we restrict ourselves to a situation in the presence of an external magnetic field (which is the situation of interest to us in this dissertation) and consider the spin decoherence channels for the localized electron spin interacting with the lattice nuclear spin bath. Since the gyromagnetic ratios (and hence the Zeeman energies) for the electron spin and the nuclear spins are typically a factor of 2000 different (the electron Zeeman energy being larger), hyperfine-induced direct spin-flip transitions between electron and nuclear spins would be impossible (except as virtual transitions as will be discussed in Sec. 3.2.4) at low temperature since phonons would be required for energy conservation. This leaves the indirect SD mechanism as the most effective electron spin decoherence mechanism at low temperatures and finite magnetic fields. The SD process is associated with the dephasing of the electron spin resonance due to the temporally fluctuating nuclear magnetic field at the localized electron site. These temporal fluctuations cause the electron spin resonance frequency to diffuse in the frequency space, hence the name spectral diffusion. These fluctuations result from the dynamics of the nuclear spin bath due to dipolar interactions between each other along with their hyperfine interactions with the qubit. This scenario is illustrated by Fig. 2.1.

Spectral diffusion is, in principle, not a limiting decoherence process for silicon or germanium based quantum computer architectures because these can, in principle, be fabricated free of nuclear spins using isotopic purification. Unfortunately this is not true for the important class of materials based on III-V compounds, where SD has been shown to play a major role [46, 35]. There is as yet no direct (e.g., GaAs quantum dots) experimental measurement of localized spin dephasing in III-V materials, but such experimental results are anticipated in the near future. Indirect spin echo measurements based on singlet-triplet transitions in coupled GaAs quantum dot systems [38] give T_2 times consistent with our theoretical results.

2.2 The Spectral Diffusion Problem

Spectral diffusion is a dephasing decoherence (i.e., a transverse or T_2-type relaxation) process, affecting only component of the Bloch vector that is perpendicular to the magnetic field. It thus contributes T_2 decoherence time rather than T_1 the decoherence time (Ref. [10] details our definition of T_1, T_2, and T_2^*). The T_1 time for these systems at low temperature is known to be much longer than this T_2 time. Experimentally, this T_2-type decay is observed from Hahn echoes in order to remove the effect of inhomogeneous broadening of an ensemble of spins that is associated with T_2^*. There are many different pulse sequences that can remove inhomogeneous broadening effects and yield different T_2 decoherence times, making its definition somewhat arbitrary. We can, however, define the T_2 time as the FID (with no applied pulses) for a single qubit instead of an ensemble [40, 43, 44]. This characteristic decay time would be relevant, for example, in a quantum computer that addresses individual qubits in a calibrated way (to account for the different phase precession of each qubit). On the other hand, defining such characteristic decay times is an oversimplification that may hold little relevance in an architecture that employs sophisticated DD and error correction schemes. The important question for us to consider with regard to SD is, rather, how the qubit will decohere given a specific DD pulse sequence.

2.2.1 Stochastic Theories

Previous attempts at analyzing this SD decoherence have been based on quasi-classical stochastic modeling. Herzog and Hahn [29] assigned a phenomenological Gaussian probability distribution function for the Zeeman frequency of the investigated spin without considering the dynamics of the nuclear bath. Later, Klauder and Anderson [32] used a Lorentzian distribution function instead in order to account for a power-law time dependence observed in experiments by Mims and Nassau [31]. Zhidomirov and Salikhov [33] devised a more sophisticated theory, with a wider range of applicability, in which the flip rate of each spin in the bath was characterized by Poisson distributions. Very recently de Sousa and Das Sarma [35], in considering SD by nuclear spin flip-flops, extended this theory to characterize flip-flop rates of pairs rather than individual spins within a phenomenological model.

2.2.2 Non-Markovian Quantum Theory

In this dissertation, we present a microscopic theory that is based entirely on the quantum mechanics of the system without resorting to phenomenological distribution functions. No Markovian assumption nor any assumption about the form of the solution was used to obtain our results. We formulate the problem in terms of the reduced density matrix of the qubit that results from time evolution produced by an approximate but microscopic Hamiltonian. The problem obviously involves too many nuclear spins to solve directly using exact Hamiltonian diagonalization (with a state space that grows exponentially with the number of bath spins); however, the cluster expansion method we devise can give successive approximations to the exact solution (convergent for short times, but often out to the tail of the decay such that the full solution is obtained for practical purposes). This cluster expansion, described in Ch. 4, breaks the problem into smaller problems involving small subsets of nuclei in the bath and is derived from a mathematically formal cluster decomposition. The fact that we only consider dephasing of the qubit, with no longitudinal relaxation, is important to the derivation of this cluster decomposition because it allows us to formulate the problem solely in terms of the quantum evolution of the nuclear bath; the qubit enters the problem in a trivial way, involving only its z spin operator which commutes with all of the operators in the problem. If we had to include the qubit as a non-trivial quantum object in the quantum evolution, then the clusters could not be treated independently, each interacting with the qubit in a non-trivial (non-commuting) way. This will be discussed in more detail in Sec. 4.3.1 but it is important to note this limitation of our technique and remark that this may be an essential key that allows this problem to be feasibly solved.

Our technique allows us not only to solve the FID problem, but also consider qubit-controlling pulse sequences that may allow one to decouple the qubit from the bath using strategies introduced in Sec. 1.4 and expounded upon in Ch. 5. Because our cluster expansion technique requires that the qubit enter the problem in a trivial way (such that qubit operators commute with all other relevant quantum operators), we are restricted to treating ideal, instantaneous pulses; that is, we restrict ourselves to the regime in which the control pulse operates on a short time-scale relative to the dynamics of the system.

We first presented our cluster expansion technique in Ref. [39] where we studied the Hahn echo decay in the Si:P system. We published a more detailed formulation of this cluster expansion along with additional results applied to GaAs quantum dots in Ref. [41], and we used this technique to study nuclear spin memory [48]. Our lowest-order solution, the pair approximation, was reproduced by Yao *et al.* [40] using an entirely different approach, providing independent validation. This group later developed a formalism that goes beyond the pair approximation using a diagrammatic linked-cluster expansion approach [45] that is essentially based upon the same perturbative arguments as our approach but is computed differently in practice; their approach offers some insight into the physical processes undergone by the nuclear spin bath, but our technique is more straight-forward computationally (we need not theoretically study and examine each possible process individually) and provides an effective way to answer numerical decoherence questions in a simple way that is not prone to calculation mistakes.

It is important to study the performance of other DD pulse sequences, beyond the Hahn echo, for qubit coherence preservation in the nuclear spin bath system. A number of these different pulse sequences have been tested numerically [47] for small, artificial systems (with bath sizes on the order of 20 nuclear spins) to give some indication of their performance. We have studied [42] the Carr-Purcell-Meiboom-Gill (CPMG) [25] periodic pulse sequences in physically relevant mesoscopic baths using our cluster expansion technique demonstrating improved qubit coherence (over the total pulse sequence time) with each applied pulses (assuming ideal pulses). Concatenations of the Hahn echo sequence were analyzed in Refs. [43, 44] for mesoscopic quantum-dot baths, and they demonstrated that, with increased concatenation levels, coherence can be maintained while increasing the time between pulses (not just increasing coherence time for the entire sequence duration). Their analysis, however, is restricted to the pair approximation which we demonstrate, in this dissertation, to be insufficient to study decoherence in these schemes; the concatenate sequence will eliminate lowest perturbative orders successively and therefore require computation of higher orders in the cluster expansion to yield the correct solution [49]. This dissertation explores this series of concatenated pulse sequences in Ch. 5 and presents more accurate decoherence results by evaluating *all* appropriate orders of the cluster expansion and testing cluster expansion convergence by evaluating an additional expansion order.

Chapter 3

The Qubit, the Bath, and Control Pulses

In Ch. 2 we introduced the basic problem that is the topic of this dissertation: the decoherence of a spin qubit, either the spin of a localized electron or that of a donor nucleus, induced by a nuclear spin bath. In this chapter we will describe the various physical qubit-bath and intra-bath interactions of the system, and show how we formulate the basic decoherence problem for an arbitrary pulse sequence. Section 3.1 first presents the form of a general free evolution Hamiltonian that will be useful in the formulations of subsequent chapters. In Sec. 3.2, we discuss typical qubit-bath and intra-bath interactions pertaining to physical systems of interest. Finally, Sec. 3.3 will formulate the decoherence problem in the context of a general sequence of ideal π-pulses.

3.1 General Free Evolution Hamiltonian

We begin with a general model for our qubit and decoherence-inducing bath. This model will be used in Chs.4 and 5 in the formulation of perturbative expansions. Specific types of interactions are discussed in Sec. 3.2, but these specifics will not be needed in the formulations of these two subsequent chapters.

In general, a qubit can decohere via depolarization as well as dephasing. However, by splitting the two energy levels of the qubit, depolarization can be effectively suppressed in a low-temperature environment because of energy conservation; we are then left only with dephasing which affects only the transverse component of the Bloch vector (see Sec. 1.3). For typical solid state spin qubit candidates, this can be feasibly done by applying a magnetic field on the order of one Tesla (to split the energies) and refrigerating the device to sub-Kelvin temperatures. With this as justification, we will disregard interactions that do not preserve the polarization (longitudinal component of the Bloch vector) of our spin qubit. This will also prove to be a useful (perhaps necessary) simplification in the formulation of our cluster expansion in Ch. 4. To be rigorous, one should consider higher-order processes with virtual spin-flip transitions of the qubit (preserving the polarization by the end of the process); such a process is considered in Sec. 3.2.4 and is not negligible, in general, even with a moderately strong applied magnetic field. However, in such a case, one may use an effective Hamiltonian to account for these processes while maintaining qubit polarization as a symmetry of the Hamiltonian.

A general Hamiltonian that preserves the qubit polarization may be written in the form $\hat{\mathcal{H}} = \sum_{\pm} |\pm\rangle \hat{\mathcal{H}}_{\pm} \langle\pm|$ where $\hat{\mathcal{H}}_{\pm}$ acts only upon the bath's Hilbert space. We can split $\hat{\mathcal{H}}_{\pm}$ into qubit dependent and independent parts, so that, without loss of generality (considering that constant terms in the Hamiltonian are irrelevant),

$$\hat{\mathcal{H}}_{\pm} = \pm \hat{\mathcal{H}}_{qb} + \hat{\mathcal{H}}_{b}, \tag{3.1}$$

$$\hat{\mathcal{H}}_{b} = \hat{\mathcal{H}}_{b0} + \epsilon \hat{\mathcal{H}}_{bb}, \tag{3.2}$$

where $\hat{\mathcal{H}}_{qb}$ is the qubit-dependent part that plays the role of coupling the qubit to the bath. The remaining qubit-independent term, $\hat{\mathcal{H}}_{b}$, is further split into interaction-independent energies in $\hat{\mathcal{H}}_{b0}$ (e.g., Zeeman energy of a spin bath), and interactions between bath constituents (intra-bath interactions) in $\hat{\mathcal{H}}_{bb}$. As a bookkeeping parameter, ϵ will be useful for carrying out perturbations with respect to intra-bath interactions.

In the mathematical formulations in Ch. 4, it will be useful to make a further assumption that the intra-bath interaction in $\hat{\mathcal{H}}_{bb}$ can be formulated as a sum of bilinear terms, a product of two operators acting on different lattice sites in the bath (e.g., different nuclear spins). This not a very limiting assumption and is satisfied by all of the intra-bath interactions discussed in Sec. 3.2.

3.2 Types of Interactions (Energies)

This section discusses typical types of interactions that may occur between a solid-state spin qubit and the nuclear spin bath or amongst nuclei at different lattice sites in the bath. Throughout this section, we equate units of energy and inverse time with $\hbar = 1$. In Sec. 3.2.1, we discuss the Zeeman interaction, which plays the important role of suppressing qubit depolarization and is responsible for independent energies of the bath nuclear spins, $\hat{\mathcal{H}}_{b0}$. Section 3.2.2 specifies the form of the dipolar interactions which often dominate the coupling between nuclear spins in the bath, playing the role of $\hat{\mathcal{H}}_{bb}$; for a donor nucleus qubit, these will also serve as the qubit-bath interactions, $\hat{\mathcal{H}}_{qb}$, as well. The hyperfine interactions of Sec. 3.2.3 provide the qubit-bath interactions, $\hat{\mathcal{H}}_{qb}$, for the localized electron spin qubit. The hyperfine-mediated and indirect exchange interactions, of Secs. 3.2.4 and 3.2.5 respectively, are additional effective interactions that may couple nuclear spins via electrons in the solid. The hyperfine-mediated interaction is long-ranged and mediated by the spin of a localized electron qubit. Its effects, however, are largely cancelled out, with a sufficiently strong applied magnetic field, by the pulse sequences considered in this dissertation. Section 3.2.6 provides a summary of all of these interactions and contains a convenient table showing their estimated magnitudes (scale).

3.2.1 Zeeman

The energy of a spin due to an applied magnetic field is known as its Zeeman energy. We take the applied field's direction to be along the z-axis, and its strength as B. The Zeeman energy of a localized electron is given by

$$\hat{\mathcal{H}}_e^{\mathrm{Z}} = \gamma_S B \hat{S}_z = \Omega_e \hat{S}_z, \tag{3.3}$$

with γ_S as its gyromagnetic ratio and $\hat{S}_z$ is the z-component of the electron spin operator. The Zeeman energy for a nuclear spin, labelled n, is similarly defined as

$$\hat{\mathcal{H}}_n^{\mathrm{Z}} = -\gamma_n B \hat{I}_{nz} = \omega_n \hat{I}_{nz}, \tag{3.4}$$

where the conventional sign of γ_n is defined in an opposite sense of γ_S.

The Zeeman energy of the qubit serves to suppress depolarization, leaving only the dephasing decoherence problem (that is, $T_2 < T_1$). Typically, $\gamma_S \sim 10^7 (\mathrm{s\ G})^{-1}$ and $\gamma_n \sim 10^4 (\mathrm{s\ G})^{-1}$; the difference in these orders of magnitude helps to suppress direct hyperfine flip-flops (discussed in Sec. 3.2.3).

3.2.2 Dipolar (Secular and Non-secular)

The dipolar interaction among spins in quantum mechanics is a straightforward quantization of the classical magnetic interaction between two dipoles. For two spins, labelled n and m with corresponding spin operators of $\hat{\boldsymbol{I}}_n$ and $\hat{\boldsymbol{I}}_m$, this is given by [50]

$$\hat{\mathcal{H}}^{\mathrm{D}}_{nm} = \frac{\gamma_n \gamma_m \hbar}{2} \left[\frac{\hat{I}_n \cdot \hat{I}_m}{R^3_{nm}} - \frac{3(\hat{I}_n \cdot \boldsymbol{R}_{nm})(\hat{I}_m \cdot \boldsymbol{R}_{nm})}{R^5_{nm}} \right], \tag{3.5}$$

where $\boldsymbol{R}_{nm}$ is the vector joining nuclei n and m. This can be expanded into a form containing only operators of the type $\hat{I}_+$, $\hat{I}_-$, or I_z (raising, lowering, and z projection spin operators respectively) [50]. The dipolar interaction between nuclear spins in semiconductors has a typical strength of $\hat{\mathcal{H}}^{\mathrm{D}}_{nm} \sim 10^2\ s^{-1}$, much smaller than typical nuclear Zeeman energies of about $10^8\ s^{-1}$ in an applied field of one Tesla. Therefore, energy conservation arguments allows us to neglect any term that changes the total Zeeman energy of the nuclei. This will leave us with the following secular contribution:

$$\hat{\mathcal{H}}^{\mathrm{D}}_{nm} \approx b_{nm} \begin{cases} 2\hat{I}_{n+}\hat{I}_{m-} - 4\hat{I}_{nz}\hat{I}_{mz} & \text{, if } \gamma_n = \gamma_m \\ -4\hat{I}_{nz}\hat{I}_{mz} & \text{, otherwise} \end{cases}, \tag{3.6}$$

$$b_{nm} = -\frac{1}{4}\gamma_n \gamma_m \hbar \frac{1 - 3\cos^2\theta_{nm}}{R^3_{nm}}, \tag{3.7}$$

where θ_{nm} is the angle of $\boldsymbol{R}_{nm}$ relative to the magnetic field direction. Note that the flip-flop interaction between nuclei with different gyromagnetic ratios is suppressed by Zeeman energy conservation in the same way that the non-secular part of the dipolar interaction is suppressed. This occurs, for example, in GaAs because the two isotopes of Ga and the one isotope of As that are present have significantly different gyromagnetic ratios.

3.2.3 Hyperfine (Contact and Anisotropic)

The hyperfine (HF) interaction between the spins of a localized electron and a nucleus in the lattice consists of a contact part (proportional to the probability that the electron is at the particular site) and a dipolar part (an expectation value of the dipolar interaction determined by the electron's wave-function). These are dependent upon the spatial wave-function of the electron that we denote as $\Psi(\boldsymbol{x})$. In its general form, the hyperfine interaction is $\hat{\mathcal{H}}_n^{\mathrm{HF}} = \hat{\boldsymbol{I}}_n \cdot \boldsymbol{A}_n \cdot \hat{\boldsymbol{S}}$, where the tensor $\mathbf{A}$ is

$$\boldsymbol{A}_{ij} = \gamma_I \gamma_S \left(\frac{8\pi}{3} \left| \Psi(\mathbf{0}) \right|^2 \delta_{ij} + \left\langle \Psi \left| \frac{3 x_i x_j - \boldsymbol{r}^2 \delta_{ij}}{\boldsymbol{r}^5} \right| \Psi \right\rangle \right), \tag{3.8}$$

with the electron's wave-function, $\Psi(\boldsymbol{x})$, taken relative to the nucleus in question. The first term of Eq. (3.8) is the *isotropic* Fermi-contact HF interaction that is proportional to the probability of the electron being at the nuclear site. The second term can be anisotropic and is responsible for the anisotropic hyperfine interaction (AHF). Which part of the interaction is more important depends on the electron wave-function. For example, the GaAs conduction band minimum occurs at the Γ-point of the Brillouin zone and the electron Bloch function is atomic s-type, so that HF interaction in GaAs between an electron near the conduction band minimum and the surrounding nuclear spins is essentially isotropic. On the other hand, the conduction band minimum for Si occurs close to the X-point of the Brillouin zone so the electron Bloch function has significant contributions from p- and d-atomic-orbitals [51, 52] so that, as a result, the HF interaction in such systems has strong anisotropic characteristics. The effects of the AHF interaction in Si:P will be studied in Sec. 6.1.3.

Typical HF interaction strengths yield $A_n \sim 10^6\ s^{-1}$. With typical Zeeman energies of $\sim 10^{11}\ s^{-1}$ for an applied magnetic field of one Tesla, Zeeman energy conservation will suppress depolarization effects due to terms in the HF interaction that involve the $\hat{S}_x$ and $\hat{S}_y$ (or equivalently $\hat{S}_+$ and $\hat{S}_-$) operators. In low fields, these so-called direct HF interactions do play a significant role and have been studied recently [53, 54]. For strong applied fields considered in this work, we use the following approximate form for the HF interaction between the electron and some nucleus labelled by n:

$$\hat{\mathcal{H}}_n^{\mathrm{HF}} \approx A_n \hat{S}_z \hat{I}_{nz} + B_n \hat{S}_z \hat{I}_{nx'}. \tag{3.9}$$

We can often disregard the dipolar part of the HF interaction and therefore neglect the anisotropic contribution (i.e., $B_n \approx 0$); then A_n is determined solely by the Fermi-contact energy:

$$A_n = \frac{8\pi}{3} \gamma_S \gamma_n \hbar |\Psi(\boldsymbol{R}_n)|^2, \tag{3.10}$$

where $\boldsymbol{R}_n$ denotes the location of this nth nucleus. The $\hat{S}_z \hat{I}_z$ part of the dipolar interaction, when it isn't negligible, may also contribute to this isotropic part of the HF interaction. The remaining terms of the dipolar interaction that involve $\hat{S}_z$ will determine the AHF interaction strength, B_n, and quantization axis, x', of Eq. (3.9).

3.2.4 Hyperfine-mediated (RKKY)

Although an applied magnetic field will suppress direct HF interactions that flip the electron spin, it is important to consider the possibility of virtual electron spin flips. This can lead to a non-local interaction between any two nuclei in the bath (mediated by their common interaction to the electron spin). This interaction, well-known [50, 55] as the RKKY interaction, diminishes with an increased strength of an applied magnetic field; however, the vast number of possible non-local nuclear pairings can make the effect significant even in a moderately strong applied magnetic field.

The HF-mediated interaction emerges perturbatively from the off-diagonal Fermi-contact HF interaction, $\hat{V} = \sum_n A_n (\hat{S}_+ \hat{I}_{n-} + \hat{S}_- \hat{I}_{n+})/2$, in the limit of a large electron Zeeman energy. Applying the transformation

$$\hat{P} = \exp\left[\sum_n \frac{A_n}{2(\Omega_e - \omega_n)} \left(\hat{S}_+ \hat{I}_{n-} - \hat{S}_- \hat{I}_{n+}\right)\right], \tag{3.11}$$

to $\hat{\mathcal{H}}$ with $\hat{\mathcal{H}} = \hat{\mathcal{H}}_e^{\mathrm{Z}} + \sum_n \hat{\mathcal{H}}_n^{\mathrm{Z}} + \sum_n \hat{\mathcal{H}}_n^{\mathrm{HF}}$, $\hat{\mathcal{H}}' = \hat{P}\hat{\mathcal{H}}\hat{P}^{-1}$ produces, in its lowest order (with respect to A_n/Ω_e), the non-local HF-mediated interaction [40],

$$\hat{\mathcal{H}}_{nm}^{\mathrm{HFM}} = \sum_{n \neq m} A_{nm} \hat{I}_{n+} \hat{I}_{m-} \hat{S}_z. \tag{3.12}$$

In applying this transformation, we must rotate the basis states slightly; this results in a "visibility" loss of coherence estimated as $\sum_n \left(A_n/\Omega_e\right)^2$ [40] and is typically very small.

Neglecting AHF interactions, which is often small (as in GaAs) or can be treated separately (as in Si:P), the qubit-bath interaction results from Fermi-contact

HF interactions. With a large Zeeman energy to suppress electron spin flips, the qubit-bath interaction is a combination of the diagonal Fermi-contact HF interaction and the HF-mediated interaction of Eq. (3.12):

$$\hat{H}_{qb} = \frac{1}{2}\sum_{n} A_n \hat{I}_{nz} + \frac{1}{2}\sum_{n \neq m} A_{nm} \hat{I}_{n+} \hat{I}_{m-}. \tag{3.13}$$

This HF-mediated interaction has a significant impact upon the free induction decay (FID, free evolution decoherence neglecting inhomogeneous broadening), and it has been studied recently both analytically [54] as well as numerically [40, 43, 44] (using cluster-type treatments inspired by our own [39, 41]).

If we neglect any other intra-bath interactions so that $\hat{H}^{\pm} = \pm \hat{H}_{qb}$, it is easy to see that $\hat{U}_0^{+} \hat{U}_0^{-} = \hat{\mathbb{1}}$. Because of this simple fact, the HF-mediated interactions are suppressed by the Hahn echo sequence and the other dynamical decoupling sequences discussed in Ch. 5. This suppression was earlier [56] observed from exact numerical simulations of small systems and also discussed [40] in the context of larger systems using a pair approximation (equivalent to the lowest order of our cluster expansion [39]). Because we only consider dynamical decoupling sequences in the results of Ch. 6, we will neglect the HF-mediated interactions and only discuss the estimated visibility loss, $\sum_n (A_n/\Omega_e)^2$, imparted by the transformation of Eq. (3.11). This is fully justified in the pair approximation of the echo decay, but to be completely rigorous, one should consider the possibility that higher order processes involving a combination of HF-mediated along with other intra-bath interactions (such as dipolar) could play an important role for some pulse sequences (such as concatenated sequence which cancel out lower order processes, as we will see in Sec. 5.1, making higher order processes relevant). Our results (of Ch. 6) are, however, valid in the limit of a strong applied magnetic field.

3.2.5 Indirect Exchange

Interactions between nuclei may be further mediated via HF interactions with virtual electron-hole pairs [55, 58, 59, 60, 61]. When this is cause by the Fermi-contact HF interaction, it is known as the pseudo-exchange interaction and takes the form [40]

$$\hat{\mathcal{H}}_{nm}^{\mathrm{Ex}} = -b_{nm}^{\mathrm{Ex}} \hat{I}_n \cdot \hat{I}_m. \tag{3.14}$$

The leading contribution to this pseudo-exchange for nearest neighbors may be expressed as [58, 59]

$$b_{nm}^{\mathrm{Ex}} = \frac{\mu_0}{4\pi} \frac{\gamma_n^{\mathrm{Ex}} \gamma_m^{\mathrm{Ex}}}{\boldsymbol{R}_{nm}^3} \frac{a_0}{\boldsymbol{R}_{nm}}, \tag{3.15}$$

where γ_n^{Ex} is the effective gyromagnetic ratio determined by renormalization of the electron charge density [40]. This interaction has been experimentally studied many years ago [59, 60, 61].

In GaAs quantum dots, these interactions can be comparable to the direct dipolar interactions of Sec. 3.2.2. There may be other local interactions between nuclei in the bath, such as the indirect pseudo-dipolar interaction [55] or intra-nuclear quadrapole interaction, but the dipolar and indirect exchange interactions alone account for the line-shapes of NMR [40]. Any such local interactions may be easily included in our formalism. However, much of our results in Ch. 6 neglect this interaction which is important in GaAs. Including these interactions, as we do in

Fig. 6.13, gives a quantitative correction to coherence times that is within an order of magnitude and has no significant qualitative effect. To be more accurate, the indirect exchange interactions should be included in applications to GaAs.

3.2.6 Summary of Interactions

Table 3.1 lists the interactions that we have discussed and indicates their rough energy scales in units of inverse time (using $\hbar = 1$) and units of temperature (using $k_B = 1$) assuming an applied magnetic field strength on the order of one Tesla. This table provides a convenient way to compare the magnitude of different energies in order to justify various perturbations and approximations. For example, our formalism (particularly the cluster expansion of Ch. 4) requires that we neglect any interactions that flip the qubit (electron) spin. This is justified by noting that $\Omega_e \gg \omega_n, A_n$. The only caveat is the consideration of higher order processes with virtual electron spin flips; this is accounted for by the HF mediated interaction, A_{nm}. The temperature scales in this table are also convenient. Because $\Omega_e \sim 1$ K, sub-Kelvin temperatures are required to to suppress electron spin flips mediated by phonons. Also, if $T \gg \omega_n \sim 1$ mK, we are justified in using a high temperature approximation for the initial density matrix of an equilibrated nuclear spin bath; if $1 \text{ mK} \gtrsim T \gg b_{nm} \sim$ 1nK, we can use a similar high temperature approximation but should account for some polarization of the bath.

Putting all of these interactions together for the electron spin qubit and relat-

Table 3.1: Interactions and estimated energy scales for a 1 T applied field. (A similar table appears in Ref. [44].)

Interaction	Symbol	Scale ($\hbar = 1$)	Scale ($k_B = 1$)
Zeeman (electron)	Ω_e	10^{11} s^{-1}	1 K
Zeeman (nucleus)	ω_n	10^8 s^{-1}	1 mK
Contact HF	A_n	10^6 s^{-1}	10 μK
Dipolar	b_{nm}	10^2 s^{-1}	1 nK
Indirect exchange	b_{nm}^{Ex}	10^2 s^{-1}	1 nK
HF mediated	A_{nm}	10 s^{-1}	10^{-1} nK

ing these interactions to the formulation of Sec. 3.1, we have

$$\hat{\mathcal{H}}_{qb} = \frac{1}{2}\sum_n A_n \hat{I}_{nz} + \frac{1}{2}\sum_{n \neq m} A_{nm} \hat{I}_{n+} \hat{I}_{m-}, \tag{3.16}$$

$$\hat{\mathcal{H}}_{b0} = \sum_n \omega_n \hat{I}_{nz}, \tag{3.17}$$

$$\hat{\mathcal{H}}_{bb} = \frac{1}{2}\sum_{n \neq m} \left(\hat{\mathcal{H}}_{nm}^{\mathrm{D}} + \hat{\mathcal{H}}_{nm}^{\mathrm{Ex}}\right) \tag{3.18}$$

Because $\omega_n \gg b_{nm}$, it is usually appropriate to use the secular approximation of Eq. (3.6); this is not necessary in our formalism and we have performed test calculations without this approximation, but our results in Ch. 6 use the limit of a strong applied magnetic field where we apply this secular approximation. Furthermore, as discussed in Ch. 3.2.4, the HF-mediated interaction may be neglected in the limit of a strong applied magnetic field, particularly for the pulse sequences that we treat. These HF-mediated interactions (A_{nm}) don't really fit will into this general form anyways because these are simultaneously qubit-bath and intra-bath interactions (it is possible to incorporate this into our formalism in a more appropriate way but with some extra complications). Our calculations also neglect the indirect exchange interaction of Sec. 3.2.5 though this is not entirely justified in GaAs. The model that we predominantly use in this work, then, uses

$$\hat{\mathcal{H}}_{qb} = \frac{1}{2}\sum_n A_n \hat{I}_{nz} \tag{3.19}$$

$$\hat{\mathcal{H}}_{bb} = \sum_{n\neq m} b_{nm} \begin{cases} 2\hat{I}_{n+}\hat{I}_{m-} - 4\hat{I}_{nz}\hat{I}_{mz} & ,\text{if } \gamma_n = \gamma_m \\ -4\hat{I}_{nz}\hat{I}_{mz} & ,\text{otherwise} \end{cases}, \tag{3.20}$$

and $\hat{\mathcal{H}}_{b0}$ is treated as a constant and is therefore irrelevant in determining the dynamics of the system.

3.3 The Decoherence Problem Given a Pulse Sequence

To formulate our decoherence problem, we will consider a qubit in an initially pure state (having no initial entanglement with the bath), so that we may write the initial density matrix as a product of qubit and bath states, $\hat{\rho}_0 = \hat{\rho}_{q0} \otimes \hat{\rho}_b$. In order to perform the cluster decomposition of Ch. 4, we must assume that the initial density matrix of the bath, $\hat{\rho}_b$, has no correlations among different nuclear spins; that is,

$$\hat{\rho}_b \equiv \sum_j P_j |\mathcal{B}_j\rangle\langle\mathcal{B}_j| = \prod_{\otimes\, n}\left(\sum_j p_{nj}|b_{nj}\rangle\langle b_{nj}|\right) \tag{3.21}$$

where P_j represents a probability for the bath to be in state $|\mathcal{B}_j\rangle$; in its more specific non-correlated form, p_{nj} represents a probability for bath state n to be in the state $|b_{nj}\rangle$. It is often appropriate to assume that the initial spin bath is in thermal equilibrium with $p_{nj} \sim \exp\left(-\omega_n/T\right)$ (in $k_B = 1$ units) since the Zeeman energy, for an applied field on the order of one Telsa, dominates the nuclear energies. In our calculations, we assuming the limiting case of a completely random initial bath; that is, we assume the effective nuclear temperature to be infinite which is valid for $T \gg \omega_n \sim mK$. With the assumption of infinite nuclear temperature, we simply use a uniform distribution in the probabilities of nuclear states. When the temperature is too low for this approximation to be valid, it is *not* difficult to incorporate the effect of resulting nuclear polarization in the calculations.

To quantify the dephasing decoherence, as represented in Fig. 1.2, one can consider the decay of the qubit's Bloch vector (the spin's expectation value) over time with the qubit in an initial state that is perpendicular the z-axis (which defines both the applied magnetic field direction and the quantization axis of the spin); such an initial state will exhibit maximal decoherence due to dephasing. Such an initial qubit state has the general form $|\psi\rangle = \left(|-\rangle + e^{i\phi}|+\rangle\right)/\sqrt{2}$, being in a equal linear combination of up and down (represented by $|+\rangle$ and $|-\rangle$ states for future convenience). Dephasing of this initial state can be considered as the interference between evolved bath states corresponding to the up, $|+\rangle$, versus down, $|-\rangle$, components of the initial spin qubit state. If we define $\hat{U}^{+}$ and $\hat{U}^{-}$ as the evolution of the bath for any considered pulse sequence with the initial spin qubit being up or down respectively, the length of the resultant Bloch vector of the reduced density matrix, quantifying the decoherence or the magnitude of the pulse sequence echo, may be written

$$
\begin{aligned}
v_E &= \left\| \mathrm{Tr}_B \left(\hat{U}^{+} \hat{\rho}_B \left[\hat{U}^{-} \right]^{\dagger} \right) \right\| && (3.22) \\
&= \left\| \sum_j P_j \left\langle \mathcal{B}_j \right| \left[\hat{U}^{-} \right]^{\dagger} \hat{U}^{+} \left| \mathcal{B}_j \right\rangle \right\| && (3.23) \\
&= \left\| \left\langle \left[\hat{U}^{-} \right]^{\dagger} \hat{U}^{+} \right\rangle \right\| = \left\| \langle \hat{W} \rangle \right\|, && (3.24)
\end{aligned}
$$

where the $\langle ... \rangle$ operator in the last line is a shorthand for the appropriate weighted average of expectation values over the bath states, and $\hat{W} \equiv \left[\hat{U}^{-} \right]^{\dagger} \hat{U}^{+}$. We use v_E to denote a generic pulse sequence echo, or we will use different subscript text for representing the echo of specific pulse sequences (e.g., v_{Hahn}, v_{CPMG}, or v_{CDD}).

In this formulation we assume that the $\hat{U}_{\pm}$ evolution operators may be defined within the state space of the bath (e.g., no qubit operators). This restricts our treatment to solely ideal π-rotation pulses in our pulse sequence. A finite width pulse, for example, would require the inclusion of the qubit in our state space for evolution operators. As mentioned in Sec. 2.2.2, this restriction is important in the formulation of our cluster expansion in Ch. 4. It may be possible to extend our treatment beyond this restriction, but that is beyond the current scope of this work (it may be important future work).

We assume, therefore, that our pulse sequence consists of ideal π-rotation pulses; this is a good approximation when the pulses can be applied on a much shorter time-scale than the dynamics of the system. The $\hat{U}^{\pm}$ operators of an arbitrary pulse sequence may then be constructed in the following way. The free evolution operators (with no pulses) are defined as

$$\hat{U}_0^{\pm}(t) = \exp\left(-i\hat{\mathcal{H}}_{\pm}t\right), \tag{3.25}$$

with $\hat{\mathcal{H}}_{\pm}$ taken from the general free evolution Hamiltonian in Sec. 3.1. Each π-pulse effectively switches $+$ and $-$. The Hahn echo evolution operator is then written

$$\hat{U}_{\text{Hahn}}^{\pm} = \hat{U}_0^{\mp}(\tau)\hat{U}_0^{\pm}(\tau), \tag{3.26}$$

with τ as the time before an after the applied pulse. The evolution operators, $\hat{U}^{\pm}$ for any pulse sequence, with ideal π-pulses, can be constructed as sequence of alternating $\hat{U}_0^{\pm}(t_n)$ and $\hat{U}_0^{\mp}(t_n)$ operators with appropriate delay times, t_n.

Chapter 4

The Cluster Expansion

Our decoherence problem of a solid state spin qubit interacting with a dephasing nuclear spin bath has been reduced, via Eq. (3.24), to the problem of evaluating $\langle \hat{W} \rangle \equiv \left\langle \left[\hat{U}^{-} \right]^{\dagger} \hat{U}^{+} \right\rangle$ where $\hat{U}^{\pm}$ are the bath evolution operators for an initial up/down spin qubit for the desired pulse sequence and $\langle ... \rangle$ averages expectation values over bath states according to their probability. Because the Hilbert space grows exponentially with the number of spins in the bath, this problem can not be feasibly solved without some simplification or approximation. In this chapter, we describe a cluster expansion of $\langle \hat{W} \rangle$ that will yield successive approximations that are feasibly computable. The convergence of this expansion will depend upon relative energy scales of the interactions and specifics of the pulse sequence and its delay times. We demonstrate, however, the utility and versatility of this expansion by studying specific applications, relevant to quantum computing architectures, in Ch. 6. In Sec. 4.1, we provide a conceptual description of this cluster expansion; Section 4.2 provides some justification for why and when we might expect such an expansion to converge; Section 4.3 supplies the mathematical formalism and practical implementation of this expansion; finally, Sec. 4.4 gives some concluding remarks for this chapter.

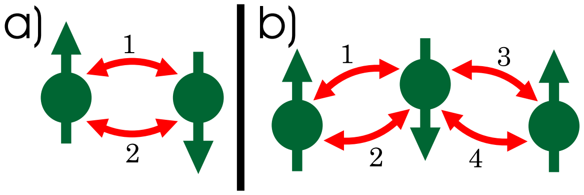

Figure 4.1: Some possible nuclear "processes" where the numbered two-sided arrows represent a sequence of flip-flops between pairs of nuclei. (a) depicts a two-nuclei process and (b) depicts a three-nuclei process.

4.1 Conceptual cluster expansion

Consider independent, simultaneous nuclear "processes" that may contribute to the decay of the Hahn echo. For example, a process may involve a pair of nuclei flip-flopping [Fig. 4.1(a)] which results in fluctuations of the effective magnetic field seen by the qubit spin, or it may involve three nuclei interdependently [Fig. 4.1(b)], etc. The dynamics of such a process results from the local coupling between nuclei (with coupling constants $\{b_{nm}\}$), and hyperfine coupling to the electron (with coupling constants $\{A_n\}$). Any number of these processes may occur "simultaneously" as long as they involve disjoint sets of nuclei and are thus independent of each other (processes that share a nucleus are not independent and would have to be combined into a larger process).

Using this (not yet well-defined) concept of nuclear processes, the cluster expansion may be described, ideally, as follows. The cluster expansion will include processes that involve a successively increasing number of nuclei. Except when we consider AHF interactions (Sec. 6.1.3), an isolated nucleus in our model does not contribute to spectral diffusion. Thus, at the lowest nontrivial order we include any simultaneous processes involving two nuclei (pairs); that is, we can involve any number of pair processes together as long as the pairs do not overlap (i.e., involve the same nucleus). At the next order, we will additionally include processes that involve three nuclei. Next, we include four nuclei processes which cannot be decomposed into two pair processes (these would already have been included). To summarize, let us say that the kth order of the expansion will include processes of up to k nuclei.

Because *all* processes involving a given number of nuclei are included at each order of this expansion, and because these processes are independent (proven formally in Sec. 4.3), rather than working with individual processes, we can work with contributions due to each given "cluster" of nuclei (for now, simply defined as a set of nuclei); such a "cluster contribution" includes contributions from all of the processes involving all nuclei in that cluster in an interdependent way (i.e., not separable into independent sub-processes). Thus we may say that the kth order of the expansion includes contributions from clusters up to size k. These "contributions" are not necessarily additive in the solution because we must account for simultaneous but independent processes (from disjoint clusters). The idea is simply to include the possibility of interdependent processes involving clusters of successively increasing size.

We deliberately use the word "cluster" to imply proximity between the members of the set of nuclei involved in interdependent processes. In fact, a near neighbor approximation, in which the constituent nuclei of a contributing cluster must be in the same neighborhood, is justified by the $1/\mathbf{R}_{nm}^3$ dependence of the intra-nuclear

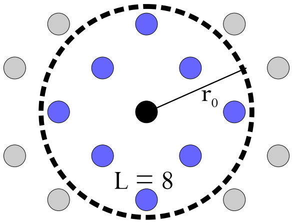

Figure 4.2: L is loosely defined as the average number of neighbors in a near neighbor approximation that converges to the exact answer. For example, we can include neighbors up to a distance r_0 away such that increasing this maximum neighbor distance in the near neighbor approximation (where non-neighbor interactions are neglected) does not significantly change the solution.

coupling constant [Eq. (3.7)]. Consider a near (not necessarily nearest) neighbor approximation with an adjustable parameter r such that we ignore interactions between nuclei that are a further apart than r. If a near neighbor approximation is applicable, the Hahn echo solution in this approximation (in principle, whether or not it is feasible to compute) will converge with an acceptable level of accuracy at some finite value of r much smaller than the system size. Let us define r_0 to be the value of r in which this acceptable convergence is achieved. Let L be the number of nuclei within a range of r_0 from any nucleus, on average, as shown in Fig. 4.2. Applying this near neighbor approximation to our cluster expansion, L determines the way in which the number of contributing clusters scales with cluster size. This has important implications for the convergence of the cluster expansion.

To be specific, the convergence of the cluster expansion depends upon two factors. The first is how the number of contributing clusters scales with cluster size (which relates to L as we have already said). The second is how the average contribution of clusters scales with cluster size. Clusters only contribute via interdependent processes; thus the set of nuclei in a contributing cluster must form a connected graph where edges in the graph connect neighbors [Fig. 4.3(a)]. When counting the number of clusters of a given size, we have N sites to choose from for the first nucleus, but there are only $\mathcal{O}(L)$ possibilities (roughly) for each additional nucleus because it must neighbor one of the previous choices. This simple analysis does not compensate for over-counting due to permuting labels and other such details, but it provides the correct scaling in terms of N and L; that is, there are $\mathcal{O}\left(NL^{k-1}\right)$ contributing clusters of size k. Our first scaling factor is then L since the number of clusters as a function of cluster size scales in powers of L. The other scaling factor will rely upon some perturbation theory to describe how cluster contributions themselves scale with an increase in cluster size. We will show, in Sec. 4.2, that, according to two complementary perturbation theories, cluster contributions scale, with size, in orders of some small perturbation parameter, λ. That is, a cluster contribution of size k, where one or both of these perturbation theories (that will be discussed shortly) are applicable, will scale as $\mathcal{O}\left(\lambda^k\right)$. Thus λ is assigned as the other scaling factor, and we may loosely argue that we expect the cluster expansion to converge when $\lambda L \ll 1$ because the total contribution from clusters then decreases as we increase in cluster size. This reasoning will become more rigorous when we go on to explain how we implement this cluster expansion.

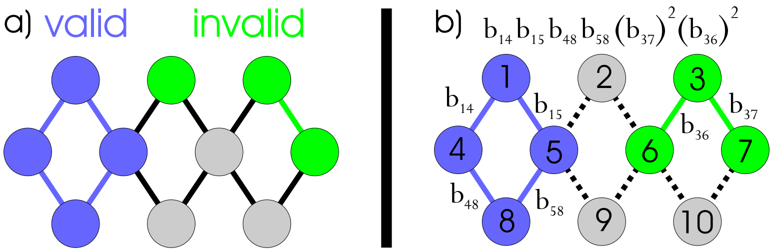

Figure 4.3: (a) The set of nuclei in a contributing cluster must form a connected graph. Edges represent neighbor connections. The set of blue nuclei on the left form a valid cluster. The set of green nuclei on the upper right are not fully connected so they do *not* form a valid cluster. (b) A set of b_{nm} factors in a term of an expansion of $\langle \hat{W} \rangle$ determines a set of disjoint clusters (the connected subgraphs formed from b_{nm} edges).

4.2 Initial Justification in Terms of Perturbation Theories

Before we delve into the details of our cluster expansion, we first discuss when and why we might expect cluster contributions to diminish with increasing cluster size. These will be based upon two different perturbation theories: the time perturbation and the intra-bath perturbation. In the time perturbation, we expand $\hat{W}$ in orders of the time between pulses; for example, Taylor expand $\hat{U}_0^{\pm} = \exp\left(-i\mathcal{H}_{\pm}\tau\right)$ and collect orders of τ. In the intra-bath perturbation, we treat intra-bath interactions as a perturbation in the Hamiltonian, expanding the Hamiltonian's eigen-states and eigen-energies in orders of ϵ. The former is expected to be convergent (at least, for small system sizes or with respect to a small cluster) when the time between pulses is small compared to the dynamics of the system, and the latter is expected to be convergent (for a small system or cluster) when the qubit-bath interaction is strong compared with the intra-bath interactions. For typical cases of an electron spin qubit, nuclei near the center of the electron's wave-function tend to have a much stronger coupling to the qubit than its coupling to other nuclei while the opposite is true for nuclei further from the electron center. In this case, the intra-bath perturbation is applicable to the near nuclei while the time perturbation is applicable to the far nuclei (since the dynamics of these interactions is relatively slow). In this sense, the two perturbation theories are complementary.

We assume that the qubit-bath interaction Hamiltonian, $\hat{\mathcal{H}}_{qb}$ is a sum of interactions with individual nuclei in the bath, and that the intra-bath interaction Hamiltonian, $\hat{\mathcal{H}}_{bb}$, is a sum of bilinear operators coupling only pairs of nuclei. We can then relate the size of a cluster contribution to its lowest perturbation order, in either perturbation theory, by noting that there is a limit to the possible number of $\hat{\mathcal{H}}_{bb}$ (bilinear operator) factors that can arise in terms of an expanded $\hat{W}$ for a given perturbation order. In the intra-bath perturbation theory, with $\lambda = \epsilon$, there can be at most k factors of $\hat{\mathcal{H}}_{bb}$ in the kth order of the perturbation because ϵ accompanies each factor of $\hat{\mathcal{H}}_{bb}$. The same argument can be used for the time perturbation, $\lambda = \tau$; each factor of $\hat{\mathcal{H}}_{bb}$ must be accompanied by a factor of τ by dimensional analysis arguments (time versus energy). Tighter restrictions can be made for specific pulse sequences, but the trend is that more $\hat{\mathcal{H}}_{bb}$ factors implies a higher perturbative order in either perturbation theory.

The bilinear operators of $\hat{\mathcal{H}}_{bb}$ can be thought of as the "glue" that binds the clusters together because without them, the lattice sites in the bath act independently of each other. Following this reasoning, a limit in the number of $\hat{\mathcal{H}}_{bb}$ factors will set a limit on the size of the cluster that can contribute such a term. Conversely, a cluster contribution must have a minimum number of $\hat{\mathcal{H}}_{bb}$ factors, determined monotonically by the size of the cluster, which corresponds to a minimum time or intra-bath perturbation order. Though the details of these bounds will depend upon the pulse sequence employed and interactions that are treated, the general trend is that cluster contributions scale, with their size, in orders of λ (used to represent either perturbation). For simplicity, then, we say that a cluster of size k gives a contribution of order λ^k.

4.3 Decoherence Via Cluster Contributions

In Sec. 4.1, we gave a rough, conceptual description of our cluster expansion to guide the reader's intuition and present some basic ideas. At this point, we will develop the rigorous mathematical formalism that relates the idea of simultaneous, independent nuclear processes contributing to the Hahn echo directly to the evaluation of $\langle \hat{W} \rangle$ needed to compute the qubit's decoherence, or pulse sequence echo. We will decompose $\langle \hat{W} \rangle$ into a sum of products of cluster contributions. Each cluster contribution will effectively contain the sum of contributions from all processes involving, inseparably (i.e., interdependently), all nuclei in the cluster. Such a decomposition requires that processes involving disjoint sets of nuclei are truly independent and interchangeable. This requirement is met by proving, as we shall, that a cluster contribution is independent of external clusters.

These cluster contributions need not be computed by analyzing the various "processes" involving each set of nuclei. The diagrammatic, linked cluster expansion approach of Ref. [45] does require consideration of these various processes (such as depicted in Fig. 4.1); while that approach can provide insight into the distinct physical processes involved, our approach lumps the net result of these processes together in a simple, automated way. The decomposition of $\langle \hat{W} \rangle$ into cluster contributions will be used recursively to define the cluster contributions themselves; this is shown in Sec. 4.3.1. With these cluster contributions concretely defined, we then discuss, in Sec. 4.3.2, how we mathematically define the ideal cluster expansion that we have conceptually described. This ideal expansion is useful for understanding some basic ideas, but in order to practically perform calculations on large systems, some further approximation techniques must be used. This practical implementation of the cluster expansion is explained in Sec. 4.3.3.

4.3.1 Decomposing into Cluster Contributions

Consider expanding $\hat{W}$ into a sum of products with respect to intra-bath coupling such that bilinear operators of $\hat{\mathcal{H}}_{bb}$ appear as factors of each term. For example, such an expansion could be made by Taylor expanding the exponentials of $U_0^{\pm}(\tau) = \exp\left(-i\mathcal{H}_{\pm}\tau\right)$ and then distributing through these sums. Each term in such an infinite expansion involves a set of nuclei through the bilinear operators. In the language of graph theory, each bilinear operator factor may be represented by edges (between nodes n and m); then the clusters are the sets of nuclei in each connected subgraph (each of these being involved in an interdependent process). Figure 4.3(b) illustrates an example of this. In this way we begin to relate our concept of clusters of interdependent processes to an expansion of $\langle \hat{W} \rangle$.

With these concepts in mind, we show how to decompose $\langle \hat{W} \rangle$ into independent contributions from different clusters of nuclei in the bath. We first define $\hat{W}_{\mathcal{S}}$ to be the same as $\hat{W}$ when only considering nuclei in the set $\mathcal{S}$. In order to show that cluster contributions are independent in a factorable way, we consider a particular cluster (or set) of nuclei contained in $\mathcal{S}$, $\mathcal{C} \subseteq \mathcal{S}$, and extract $\langle \hat{W}_{\mathcal{C}} \rangle$ from $\langle \hat{W}_{\mathcal{S}} \rangle$. We note that $\hat{W}_{\mathcal{S}} - \hat{W}_{\mathcal{C}} \otimes \hat{W}_{\mathcal{S}-\mathcal{C}}$, as expanded in bilinear operators, must involve cluster that bridge $\mathcal{C}$ and $\mathcal{S} - \mathcal{C}$; that is, all of its terms will contain bilinear operators such that one operator is in $\mathcal{C}$ and the other in $\mathcal{S} - \mathcal{C}$. Therefore, terms of $\hat{W}_{\mathcal{S}}$ that involve cluster $\mathcal{C}$ (independent from other clusters) must be contained in $\hat{W}_{\mathcal{C}} \otimes \hat{W}_{\mathcal{S}-\mathcal{C}}$. Because $\hat{W}_{\mathcal{C}}$ and $\hat{W}_{\mathcal{S}-\mathcal{C}}$ operate on disjoint subspaces of the Hilbert space, it follows that $\langle \hat{W}_{\mathcal{C}} \otimes \hat{W}_{\mathcal{S}-\mathcal{C}} \rangle = \langle \hat{W}_{\mathcal{C}} \rangle \times \langle \hat{W}_{\mathcal{S}-\mathcal{C}} \rangle$ in a bath that is initially uncorrelated as in Eq. (3.21). Now if we define $\hat{W}'_{\mathcal{C}}$ as the sum of only those terms in $\hat{W}_{\mathcal{C}}$ whose bilinear operators fully connect all of the nuclei in the set $\mathcal{C}$ (such that the terms each involve *all* nuclei in $\mathcal{C}$), then $\langle \hat{W}'_{\mathcal{C}} \rangle$ defines a cluster contribution. Using the above arguments, we may then decompose $\langle \hat{W}_{\mathcal{S}} \rangle$ as

$$\langle \hat{W}_{\mathcal{S}} \rangle = \sum_{\substack{\{\mathcal{C}_i\} \text{ disjoint}, \\ \mathcal{C}_i \neq \emptyset,\ \mathcal{C}_i \subseteq \mathcal{S}}} \prod_i \langle \hat{W}'_{\mathcal{C}_i} \rangle \tag{4.1}$$

$$= 1 + \sum_{\substack{\{\mathcal{C}_i\} \neq \emptyset \text{ disjoint}, \\ \mathcal{C}_i \neq \emptyset,\ \mathcal{C}_i \subseteq \mathcal{S}}} \prod_i \langle \hat{W}'_{\mathcal{C}_i} \rangle, \tag{4.2}$$

where the summation of Eq. (4.1) is over all possible sets, $\{\mathcal{C}_i\}$, of disjoint nonempty

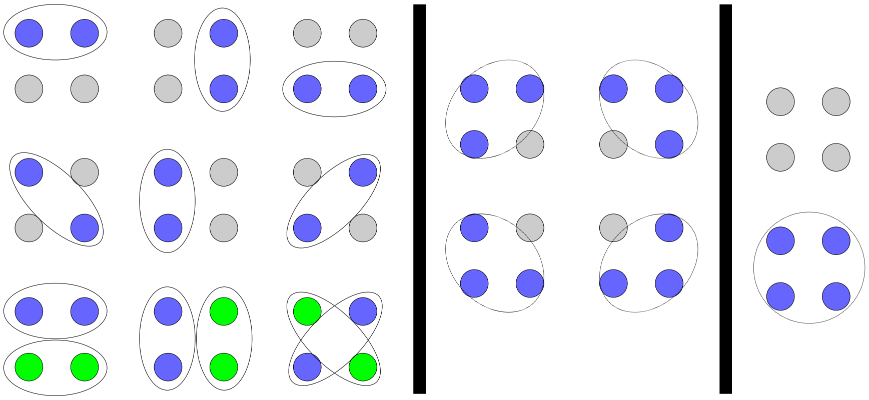

Figure 4.4: Set of all possible sets, $\{C_i\}$, of disjoint contributing clusters contained in a set, $\mathcal{S}$, of four nuclei as an example. Contributing clusters are of size 2 or greater (a single nucleus gives no contribution on its own). The cases on the left involve 2-nuclei, middle ones involve 3-nuclei, and the ones on the right are the trivial cases of $\{C_i\} = \emptyset$ or $\{C_i\} = \{\mathcal{S}\}$. Such possibilities are iterated over in the summation of Eq. (4.1).

clusters, $\mathcal{C}_i$, each of which is contained in or equal to $\mathcal{S}$. In other words, it iterates over all possible ways of dividing any part of $\mathcal{S}$ into disjoint clusters as depicted in Fig. 4.4. The product is over all clusters in each set. Despite the index, i, the order is irrelevant and permutations do not count as distinct cases. Extracting the trivial $\{\mathcal{C}_i\} = \emptyset$ term yields Eq. (4.2), shown explicitly to avoid confusion or ambiguity. The unique existence of such a decomposition follows from the fact that any $\langle \hat{W}'_{\mathcal{C}} \rangle$ must be well-defined independent of any nuclei outside of $\mathcal{C}$.

We can use Eq. (4.1) itself to obtain an unambiguous expression for any $\langle \hat{W}'_{\mathcal{C}} \rangle$. We do this by applying Eq. (4.1) to the case in which $\mathcal{S} = \mathcal{C}$ and pulling out the term, from the summation, in which $\{\mathcal{C}_i\} = \{\mathcal{C}\}$ leaving only sets in which all $\mathcal{C}_i \neq \mathcal{C}$:

$$\langle \hat{W}_{\mathcal{C}} \rangle = \langle \hat{W}'_{\mathcal{C}} \rangle + \sum_{\substack{\{\mathcal{C}_i\} \text{ disjoint,} \\ \mathcal{C}_i \neq \emptyset,\ \mathcal{C}_i \subset \mathcal{C}}} \prod_i \langle \hat{W}'_{\mathcal{C}_i} \rangle, \tag{4.3}$$

so that

$$\langle \hat{W}'_{\mathcal{C}} \rangle = \langle \hat{W}_{\mathcal{C}} \rangle - \sum_{\substack{\{\mathcal{C}_i\} \text{ disjoint,} \\ \mathcal{C}_i \neq \emptyset,\ \mathcal{C}_i \subset \mathcal{C}}} \prod_i \langle \hat{W}'_{\mathcal{C}_i} \rangle. \tag{4.4}$$

Equation (4.4) provides a recursive definition of a cluster contribution. Starting with the computation of $\langle \hat{W}_{\mathcal{C}} \rangle$, which may feasibly be calculated by direct diagonalization of $\hat{\mathcal{H}}^{\pm}_{\mathcal{C}}$ for small clusters, one must subtract terms that involve multiple independent processes and processes that do not involve all of the nuclei in $\mathcal{C}$. It is a direct consequence of the decomposition given by Eq. (4.1).

To ensure that Eq. (4.4) is well-understood, we show more explicit results for clusters of size one through four. Apart from AHF-induced effects, a single isolated nucleus does not contribute to spectral diffusion. In typical uses of the cluster expansion, therefore, $\langle \hat{W}'_{\mathcal{C}_1} \rangle = \langle \hat{W}_{\mathcal{C}_1} \rangle - 1 = 0$ for any $\mathcal{C}_1$ cluster of size one ($|\mathcal{C}_1| = 1$). It follows that for 2-clusters, $\langle \hat{W}'_{\mathcal{C}_2} \rangle = \langle \hat{W}_{\mathcal{C}_2} \rangle - 1$ (with $|\mathcal{C}_2| = 2$), having no contributing proper sub-clusters. For 3-clusters, we must subtract off contributions from contained pairs:

$$\langle \hat{W}'_{\mathcal{C}_3} \rangle = \langle \hat{W}_{\mathcal{C}_3} \rangle - 1 - \sum_{\substack{\mathcal{C}_2 \subset \mathcal{C}_3, \\ |\mathcal{C}_2| = 2}} \langle \hat{W}'_{\mathcal{C}_2} \rangle. \tag{4.5}$$

For 4-clusters, we must also subtract off contributions from contained 3-clusters and the products of contributions from contained disjoint pairs:

$$\begin{aligned}\langle \hat{W}'_{\mathcal{C}_4} \rangle &= \langle \hat{W}_{\mathcal{C}_4} \rangle - 1 - \sum_{\substack{\mathcal{C}_2 \subset \mathcal{C}_4, \\ |\mathcal{C}_2|=2}} \langle \hat{W}'_{\mathcal{C}_2} \rangle - \sum_{\substack{\mathcal{C}_3 \subset \mathcal{C}_4, \\ |\mathcal{C}_3|=3}} \langle \hat{W}'_{\mathcal{C}_3} \rangle \\ & \quad - \frac{1}{2} \sum_{\substack{\mathcal{A} \bigcup \mathcal{B} = \mathcal{C}_4, \\ |\mathcal{A}|=|\mathcal{B}|=2}} \langle \hat{W}'_{\mathcal{A}} \rangle \langle \hat{W}'_{\mathcal{B}} \rangle \end{aligned} \tag{4.6}$$

The factor of one-half in the last term is needed to compensate for the fact that $\mathcal{A}$ and $\mathcal{B}$ may be swapped in the summation; it is only a consequence of the notation used here (where $\mathcal{A}$ and $\mathcal{B}$ are interchangeable labels).

4.3.2 Ideal cluster expansion

We are now able to compute cluster contributions to be used in the evaluation of our cluster expansion. Revising Eq. (4.1) slightly, we may write the following expression for the ideal cluster expansion up to k^{th} order:

$$\langle \hat{W} \rangle^{(k)} = \sum_{\substack{\{\mathcal{C}_i\} \text{ disjoint}, \\ \mathcal{C}_i \neq \emptyset, \ |\mathcal{C}_i| \leq k}} \prod_i \langle \hat{W}'_{\mathcal{C}_i} \rangle. \tag{4.7}$$

In order to estimate the error of the kth order of the expansion, we can compare it with the $(k+1)^{\text{th}}$ order which must include contributions from $k+1$ sized clusters. One way to convert $\langle \hat{W} \rangle^{(k)}$ into $\langle \hat{W} \rangle^{(k+1)}$ is to add additional terms to the sum in which we replace any k-cluster contribution of an existing term with any $(k+1)$-cluster contribution generated by adding one neighboring nucleus to the original k-cluster. In doing so, a replacement must be made because the original k-cluster becomes disqualified when we introduce the new $(k+1)$-cluster which contains it (due to the requirement that the clusters be disjoint). This approach will account for all new sets of $\{\mathcal{C}_i\}$ containing a $(k+1)$-cluster (since any $(k+1)$-cluster can be made by adding a nucleus to a k-cluster); however, cases will be over-counted because many k-clusters can be used to build the same $(k+1)$-cluster. This is unimportant because our goal now is to estimate the error of $\langle \hat{W} \rangle^{(k)}$ relative to $\langle \hat{W} \rangle^{(k+1)}$ and overestimating this error is just as good. Proceeding along these lines, we first separate out the k-cluster contributions:

$$\langle \hat{W} \rangle^{(k)} = \sum_{\substack{\{\mathcal{C}_i, \mathcal{D}_j\} \text{ disjoint}, \\ 0<|\mathcal{C}_i|<k,\ |\mathcal{D}_j|=k}} \prod_i \langle \hat{W}'_{\mathcal{C}_i} \rangle \prod_j \langle \hat{W}'_{\mathcal{D}_j} \rangle. \tag{4.8}$$

This performs the same summation over sets of disjoint clusters as in Eq. (4.7) except that we label k-clusters as $\mathcal{D}_j$ and the smaller clusters as $\mathcal{C}_i$. With these k-clusters now set apart, we can estimate the error of $\langle \hat{W} \rangle^{(k)}$ relative to $\langle \hat{W} \rangle^{(k+1)}$ by noting that the sum of all $(k+1)$-cluster contribution replacements of $\langle \hat{W}'_{\mathcal{D}_j} \rangle$ are roughly $\mathcal{O}(\lambda L) \times \langle \hat{W}'_{\mathcal{D}_j} \rangle$. Recall that λ was introduced as a perturbation parameter such that a cluster contribution of size k scales as $\mathcal{O}(\lambda^k)$, and L is the average number of neighbors so that there are, roughly speaking, $\mathcal{O}(L)$ $(k+1)$-clusters that may be built out of one k-cluster. Thus

$$\begin{aligned} \langle \hat{W} \rangle^{(k+1)} \quad = & \sum_{\substack{\{\mathcal{C}_i, \mathcal{D}_j\} \text{ disjoint}, \\ 0<|\mathcal{C}_i|<k,\ |\mathcal{D}_j|=k}} \prod_i \langle \hat{W}'_{\mathcal{C}_i} \rangle \times \\ & \prod_j \langle \hat{W}'_{\mathcal{D}_j} \rangle \left[1 + \mathcal{O}(\lambda L) \right]. \end{aligned} \tag{4.9}$$

If we explicitly include these $(k+1)$-clusters, they would have relative corrections of $\mathcal{O}(\lambda L)$ to account for $(k+2)$-clusters and so forth. This provides a more rigorous argument for our previous assertion that the cluster expansion converges when $\lambda L \ll 1$.

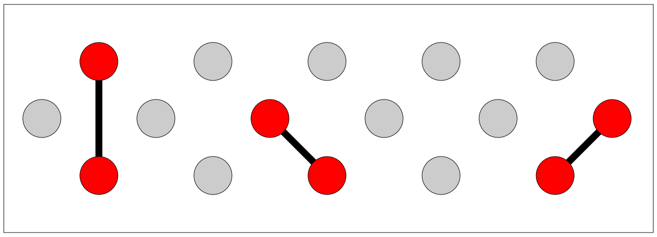

Figure 4.5: One possible combination of simultaneously included pair contributions. The red/dark circles are the nuclei whose processes are being considered.

4.3.3 Practical implementation of the cluster expansion

Equation (4.7) directly implements the conceptual cluster expansion as described in Sec. 4.1 (the inclusion of contributions from all clusters up to size k); however, it is impractical for calculating results in large systems. At the lowest nontrivial order, we would need to sum over all possible products of disjoint pair contributions; for example, Fig. 4.5 depicts one such combination of disjoint pairs. It is simply not feasible for a computer to iterate through all such possibilities when dealing with the large baths ($N \gtrsim 10^6$) that we treat. However, we can effectively obtain all possible combinations by making products of the form $\prod_{\mathcal{C}} \left[1 + \langle \hat{W}'_{\mathcal{C}} \rangle\right]$. Distributing through a given factor yields the possibility of excluding, via the 1 term, or including, via the $\langle \hat{W}'_{\mathcal{C}} \rangle$ term, that cluster. Therefore, such a product gives the sum of all possible combinations of simultaneous cluster processes (for the clusters included in the product). Unfortunately, this will yield combinations that involve overlapping clusters (that are therefore not independent). These overlapping clusters will introduce an error that, in principle, may be corrected in successive orders of an approximation.

With this approach, the lowest nontrivial order of the expansion may be implemented with

$$\langle\hat{W}\rangle^{(2)} \approx \prod_{|\mathcal{C}_2|=2}\left[1+\langle\hat{W}'_{\mathcal{C}_2}\rangle\right], \tag{4.10}$$

producing all combinations of pair contributions along with some extraneous terms, such as overlapping pairs as depicted in Fig. 4.6(b). For a moment, let us disregard these erroneous terms and consider the consequence of this approximation. If we take the logarithm of both sides, we can convert the product on the right-hand side of Eq. (4.10) into a convenient sum:

$$\begin{aligned}\ln\left(\langle\hat{W}\rangle^{(2)}\right) &\approx \sum_{|\mathcal{C}_2|=2}\ln\left(1+\langle\hat{W}'_{\mathcal{C}_2}\rangle\right) &(4.11)\\ &\approx \sum_{|\mathcal{C}_2|=2}\langle\hat{W}'_{\mathcal{C}_2}\rangle\left[1+\mathcal{O}\left(\langle\hat{W}'_{\mathcal{C}_2}\rangle\right)\right], &(4.12)\end{aligned}$$

where Eq. (4.12) follows from the Taylor expansion of $\ln\left(1+\langle\hat{W}'_{\mathcal{C}_2}\rangle\right)$ for $\langle\hat{W}'_{\mathcal{C}_2}\rangle \ll 1$, which we will shortly justify in a self-consistent way. If we assume that $\langle\hat{W}'_{\mathcal{C}_2}\rangle$ is small for all (or most) of the $\mathcal{C}_2$ pairs, then

$$\begin{aligned}\langle\hat{W}\rangle^{(2)} &\approx \exp\left[\Sigma_2(\tau)\right], &(4.13)\\ \Sigma_2(\tau) &= \sum_{|\mathcal{C}_2|=2}\langle\hat{W}'_{\mathcal{C}_2}\rangle. &(4.14)\end{aligned}$$

For this discussion, we will assume that the bath is unpolarized so that, by symmetry of the system with respect to up and down, $\langle\hat{W}\rangle$ is always real-valued. It follows that $-1 \leq \langle\hat{W}_{\mathcal{C}_2}\rangle \leq 1$; therefore, $-2 \leq \left[\langle\hat{W}'_{\mathcal{C}_2}\rangle = \langle\hat{W}_{\mathcal{C}_2}\rangle - 1\right] \leq 0$. Because $\langle\hat{W}'_{\mathcal{C}_2}\rangle\Big|_{\tau=0} = \langle\hat{W}_{\mathcal{C}_2}\rangle\Big|_{\tau=0} - 1 = 0$, $\Sigma_2(\tau=0)=0$ and becomes increasingly negative (initially at the very least) as τ is increased. For a large system, we expect $\Sigma_2(\tau)$ to decrease monotonically to a negative value that is $-\mathcal{O}\left(LN\right)$ [i.e., $\langle\hat{W}'_{\mathcal{C}_2}\rangle$ have become random and there are $\mathcal{O}(LN)$ pairs] so that Eq. (4.13) exhibits a decay form. The first part of the decay, when $\Sigma_2(\tau) \gtrsim -1$ so that $\langle \hat{W} \rangle^{(2)} \gtrsim e^{-1}$, is what interests us the most. When $\langle \hat{W} \rangle^{(2)} \gtrsim e^{-1}$ the average pair contribution will be, at most, $\mathcal{O}(1/LN)$, self-consistently justifying the approximation of Eq. (4.13) relative to Eq. (4.12) when N is large (as it is for systems of interest). Increasing τ much beyond this point will bring us to the tail of the decay in which $\langle \hat{W} \rangle \approx \langle \hat{W} \rangle^{(2)} \ll 1$. To state this in a physically intuitive way, the decoherence of spectral diffusion is caused by many nuclei collectively such that each potentially flip-flopping nuclear pair contributes only a small amount to the overall dephasing before coherence is completely lost.

For practical purposes (i.e., for time-scales prior to reaching the tail of the echo decay), we thus regard each pair contribution to be $\mathcal{O}(1/LN)$. Now let us discuss the extraneous overlapping pairs of Eq. (4.10) that we have thus far disregarded. We can now think of these cases, and their corrections, in orders of $1/N$ with each increase in the number of overlapping clusters. The lowest order correction will therefore remove cases of two pairs that overlap with each other. For any given pair, there are $\mathcal{O}(L)$ pairs that can overlap with it, each of which has a contribution of $\mathcal{O}(1/LN)$ as discussed above. Therefore in estimating the error of Eq. (4.10) we may write

$$\langle \hat{W} \rangle^{(2)} = \prod_{|\mathcal{C}_2|=2} \left(1 + \langle \hat{W}'_{\mathcal{C}_2} \rangle \left[1 + \mathcal{O}\left(\frac{1}{N} \right) \right] \right). \tag{4.15}$$

Applying this error estimate to Eq. (4.13), we have

$$\langle \hat{W} \rangle^{(2)} = \exp\left(\Sigma_2(\tau) \left[1 + \mathcal{O}\left(\frac{1}{N} \right) \right] \right). \tag{4.16}$$

An intuitive way to think about the smallness of this error is to imaging picking a *few* pairs in the bath at random (since these pair contributions are assumed small, considering *many* pair contributions multiplied together is unnecessary). For a large bath, it is very unlikely, with a probability $\sim \mathcal{O}(1/N)$, to pick overlapping pairs (or the same pair multiple times).

Because a cluster contribution scales in orders of λ as we increase the cluster size, this approach may be used for higher order cluster contributions provided that $\lambda \ll N$ (typically, $\lambda \ll 1$ where the cluster expansion is applicable). Taking either $\lambda \ll 1$ or $\lambda \sim 1$, we may write, as an extension of the above approach to higher orders,

$$\begin{aligned} \ln\left(\langle \hat{W} \rangle^{(k)}\right) &= \sum_{j=2}^{k} \Sigma_j(\tau) \left[1 + \mathcal{O}\left(\frac{1}{N}\right)\right], &(4.17)\\ \Sigma_j(\tau) &= \sum_{|\mathcal{C}|=j} \langle \hat{W}'_{\mathcal{C}} \rangle. &(4.18) \end{aligned}$$

Note that $\Sigma_k(\tau) \sim \Sigma_{k-1}(\tau) \times \mathcal{O}(\lambda L)$, since there are roughly $\mathcal{O}(L)$ times as many k-clusters as $(k-1)$-clusters and on average each k-cluster contribution, by the definition of λ, is $\mathcal{O}(\lambda)$ times that of the average $(k-1)$-cluster. With this in mind, we see that, under the cluster expansion, $\ln\left(\langle \hat{W} \rangle\right)$ is effectively expanded, additively, in powers of (λL).

In addition to the expansion in cluster size, we may also successively correct for the $\mathcal{O}(1/N)$ errors of overlapping clusters. This is done by starting with the smallest number of overlapping clusters of the smallest sizes; that is, start with the case of two overlapping pairs (Fig. 4.6). Each additional cluster included in the set of overlapping clusters being considered will multiply $\mathcal{O}(1/N)$ to the correction, and each additional nucleus added to any cluster will multiply $\mathcal{O}(\lambda L)$ to the correction.

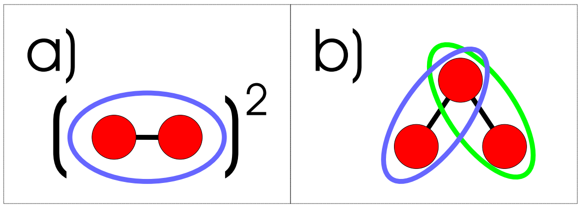

Figure 4.6: The practical implementation of the cluster expansion approximates the ideal cluster expansion up to errors resulting from overlapping clusters. At the lowest order, such errors involve overlapping pairs. (a) A single pair multiplied by itself (i.e., a pair overlapping itself) and (b) two pairs overlapping by sharing a nucleus.

For our purposes, we will only consider the correction for two overlapping pairs as a check to verify that the approximation made in Eq. (4.17) is valid.

There are two cases to consider for this lowest order correction of overlapping clusters: the same pair multiplied by itself [Fig. 4.6(a)] which was introduced by the approximation of Eq. (4.12), and two different pairs that overlap [Fig. 4.6(b)] which originates from Eq. (4.10). These cases are, respectively, eliminated, to lowest order (two pairs and only two pairs that overlap), by adding the following to Eq. (4.17):

$$\Sigma_2^*(\tau) = -\frac{1}{2}\sum_{|\mathcal{C}_2|=2}\left[\langle \hat{W}'_{\mathcal{C}_2}\rangle\right]^2, \tag{4.19}$$

$$\Sigma_3^*(\tau) = -\frac{1}{2}\sum_{\substack{|\mathcal{A}\bigcup\mathcal{B}|=3,\\ |\mathcal{A}|=|\mathcal{B}|=2}} \langle \hat{W}'_{\mathcal{A}}\rangle\langle \hat{W}'_{\mathcal{B}}\rangle, \tag{4.20}$$

so that

$$\begin{aligned}\ln\left(\langle \hat{W}\rangle^{(k)}\right) &= \Sigma_2(\tau)+\Sigma_2^*(\tau)+\Sigma_3^*(\tau) \\ &\quad + \sum_{j=3}^{k}\Sigma_j(\tau)\left[1+\mathcal{O}\left(\frac{1}{N}\right)\right].\end{aligned} \tag{4.21}$$

Exponentiating Eq. (4.21) then expanding and distributing this exponential into a sum of products form will yield the sum of all products of disjoint cluster contributions, as in Eq. (4.7), plus extraneous terms of overlapping clusters. However, all cases of only two pairs overlapping with each other (including a pair multiplied by itself) will be removed as a result adding in $\Sigma_2^*(\tau)$ and $\Sigma_3^*(\tau)$. There will remain higher-order errors with more than two overlapping clusters or overlapping clusters larger than pairs; in fact, additional higher-order errors are introduced by the $\Sigma_2^*(\tau)$ and $\Sigma_3^*(\tau)$ corrections itself. For this reason, it is difficult to derive higher-order corrections (you must correct errors introduced by lower order corrections). We can, however, regard this lowest order correction as an estimate of the error caused by these extraneous overlapping clusters:

$$\begin{aligned} \ln\left(\langle\hat{W}\rangle^{(k)}\right) &= \sum_{j=2}^{k}\Sigma_j(\tau) + \mathcal{O}\left(\Sigma^*(\tau)\right), & (4.22) \\ \Sigma^*(\tau) &= \Sigma_2^*(\tau) + \Sigma_3^*(\tau). & (4.23) \end{aligned}$$

Note that $\Sigma_2^*(\tau)$ and $\Sigma_3^*(\tau)$ are both ≤ 0 and therefore add constructively (otherwise we would want to take absolute values in order to estimate the error conservatively). Fortunately, calculations of $\Sigma^*(\tau)$ indicate that it is a minor correction for practical purposes. Such calculations verify the argument that these are $\mathcal{O}(1/N)$ errors [at least for practical values of τ for which $\langle\hat{W}\rangle \gtrsim e^{-1}$].

4.4 Cluster Expansion in Summary

The cluster expansion method that we have developed in this section is very powerful and quite general. The disjoint cluster decomposition [Eq. (4.1)] could be used to take the trace of any evolution operators described by Hamiltonians with pairwise (or even higher order) interactions. In the context of decoherence problems, it is important that the qubit enters the problem in a trivial way (only via the $\hat{S}_z$ operator) to avoid needing to include it as a kind of "super-node" in all clusters; this would make it difficult to break up the problem into separate and independent problems that involve small clusters. Furthermore, we must assume that the bath is initially uncorrelated in order to treat clusters independently. Beyond these assumptions, the decomposition is completely general. This decomposition may then be used to form an expansion [Eq. (4.7)] that converges when the sum of cluster contributions decreases with cluster size (i.e., $\lambda L \ll 1$). In order to practically compute this expansion for a large system, we need to use approximations such as Eq. (4.15) or Eq. (4.17) which have the additional requirement that each cluster contribution be small [e.g., $\mathcal{O}(1/N)$] so that extraneous overlapping clusters arising from these approximations are small. This is, in principle, a formally exact, systematic expansion, and its convergence may be tested by comparing $\Sigma_j(\tau)$ for at least $j = 2, 3,$ and 4 as well as $\Sigma^*(\tau)$. It is important to compute $\Sigma_4(\tau)$ as well as $\Sigma_3(\tau)$ because, in an unpolarized bath, all odd orders of λ for both the time and intra-bath perturbation theories are eliminated by symmetry [41]; therefore, 3 cluster contributions are actually $\mathcal{O}(\lambda^4)$.

We conclude this section by remarking that, besides being elegant and useful for understanding the expansion, the natural logarithm form of the Hahn echo given by Eq. (4.22) has the advantage that it is convenient to compute $\Sigma_j(\tau)$ and $\Sigma^*(\tau)$ using statistical sampling (Monte-Carlo) techniques. Rather than computing the full sum, randomly selected terms may be sampled and averaged in order to obtain an estimate for each sum. This can save a lot of computation time and makes this method powerful for large, complicated systems.

Chapter 5

Pulse Sequences for Dynamical Decoupling

The formalism of Ch. 4 is generally applicable to any sequence of ideal π-rotation pulses as described in Sec. 3.3. Typically, these pulses use electromagnetic spin resonance to address the qubit spin without affecting the bath directly. Any technique that will rotate the qubit, as long as this rotation is fast relative to the dynamics of the bath, is considered a pulse. A pulse sequence refers to a series of rotations and delays (free evolution), at the end of which the hope is to restore the qubit to its original state (up to a known rotation) with little decoherence induced by the bath.

Applying specific sequences of rotating pulses can be an effective strategy to decouple the qubit from the bath. In this chapter we will discuss the strategy of using both periodic and concatenated sequences of pulses for the purposes of dynamical decoupling (DD). We start with the simple Hahn echo [22] sequence that was illustrated in Fig. 1.3. It is designed to remove the effects of inhomogeneous broadening, dephasing that results from inhomogeneity of the magnetic field when measuring the signal from an ensemble of "qubit" spins at different locations. The decay of the echoes as a function of τ is typically used to measure the "intrinsic" T_2 dephasing time of these spins in order to distinguish it from the T_2^* time-scale of the inhomogeneous broadening; a more appropriate T_2, however, would be the time-scale of free induction decay (FID) [40], the decay of a *single* spin's expectation value (with a known bath polarization) as a result of free evolution.

The Hahn echo decay is not a strictly proper measurement of T_2 because this sequence offers dynamical decoupling beyond refocusing spins that are inhomogeneously broadened. This decoupling occurs because there are no interactions between the qubit and the bath in the time-averaged Hamiltonian (proportional to $\hat{\mathcal{H}}^{+} + \hat{\mathcal{H}}^{-}$); as a consequence, the evolution operators preserve qubit coherence in the lowest order of a Magnus [23] expansion. It is known [14] that repeating such a sequence, known as periodic dynamical decoupling (PDD), at a rate that is fast compared to the dynamics of the system will prolong the overall coherence time of the qubit(s). Concatenating such a sequence, known as concatenated dynamical decoupling (CDD), can often do a better job of decoupling the qubit from a bath by preventing the buildup of errors that plague periodic sequences [18].

The effective concatenation of the Hahn echo series was considered in Ref. [43]; there it is asserted that this concatenation successively decouples the qubit from the bath in orders of a time expansion for the decoherence decay. This CDD series will be analyzed in Sec. 5.1 where we will show how it eliminates successive orders in both the time and intra-bath perturbations [49] that relate to the cluster expansion of Ch. 4. Sections 5.1.2 and 5.1.3 analyze the lowest order echo result in the time and intra-bath perturbations respectively, and Sec. 5.1.4 discusses the Magnus expansion in order to relate our work to more standard treatments of DD. Section 5.2 will discuss the consequences of repeating the evolution of any level of this concatenated series; such PDD can be used for flexibility if one does not wish to be constrained by the concatenation series' need for the number of time segments (e.g., between pulses) to be a power of two. We also relate the discussion to the known CPMG (Carr-Purcell-Meiboom-Gill) periodic series that we analyzed in Ref. [42].

The time (τ) and intra-bath (ϵ) perturbations are only consequential, for a large bath, because of their relationship to the cluster expansion of Ch. 4; the cluster expansion extends the applicability of these perturbations to large systems when the system size overwhelms the smallness of the perturbation. In that chapter, a correspondence was made between an expansion in the size of clusters of lattice sites to orders in either the time or intra-bath perturbation. Note that as levels of the concatenated dynamical decoupling (CDD) sequences discussed in Sec. 5.1 eliminate successive orders of either perturbation, there is a corresponding need to incorporate larger cluster sizes to yield the true lowest-order result. This invalidates the use of the pair approximation in Refs. [43, 44] to analyze the effectiveness of the CDD series; clusters larger than pairs (2-clusters) must be included for any CDD level beyond the first level (i.e., the Hahn sequence) [49].

5.1 Concatenated Dynamical Decoupling

A concatenated pulse sequence is one that is defined by recursion. At level zero, we have free evolution for a time τ. At the first level, we insert pulses between τ-length free evolutions in order to compose a dynamical decoupling sequence, one in which the qubit and the bath are decoupled in the time-averaged Hamiltonian. The next level replaces the τ-length free evolution embedded in the first level with the sequence of the first level itself.

In concatenating the Hahn sequence, we apply an extra π-pulse (either at the beginning or the end) in order to return the qubit to its original state (apart from decoherence). Using X to denote the π rotations around the x axis (arbitrarily chosen as a direction perpendicular to the applied field) this sequence may be recursively defined as [19]

$$\mathrm{p}_l := \begin{cases} \tau & \text{, if } l = 0 \\ \mathrm{X}\mathrm{p}_{l-1}\mathrm{X}\mathrm{p}_{l-1} & \text{, otherwise} \end{cases} \tag{5.1}$$

With each concatenation, we do to the previous sequence what the Hahn echo does to free evolution and in this way we obtain improved dynamical decoupling. More general concatenated sequences [18] apply pulses in multiple directions (not just X). Such sequences can decouple the qubit from a depolarizing bath as well as a dephasing bath. Since our treatment only deals with dephasing (as a necessary approximation for our cluster expansion formalism), we only consider the simple concatenated sequence of Eq. (5.1) with pulses applied only in one direction, X.

We can simplify the concatenated sequence of Eq. (5.1) by noting that two π rotations does nothing. Therefore, assuming $l > 0$, and ignoring any pulse at the start or end of the sequence (having no consequence in terms of coherence),

$$\mathrm{p}_l := \begin{cases} \mathrm{p}_{l-1}\mathrm{X}\mathrm{p}_{l-1} & \text{, odd } l \\ \mathrm{p}_{l-1}\mathrm{p}_{l-1} & \text{, even } l \end{cases} . \tag{5.2}$$

For the sake of our analysis, we only need to consider how this sequence will impact the $\hat{U}^{+}$ and $\hat{U}^{-}$ evolution operators, the evolution of the bath with an initial up or down qubit respectively. These will have the following recursive form [43]:

$$\hat{U}_l^{\pm} = \hat{U}_{l-1}^{\mp} \hat{U}_{l-1}^{\pm}. \tag{5.3}$$

where $\hat{U}_0^{\pm}$ freely evolves the bath (with electron spin up or down) for a time τ as defined above.

5.1.1 Eliminating Successive Perturbative Orders

To simplify the arguments of this section, we assume that the spin bath is unpolarized such that, by symmetry, $\left\langle \hat{W}_l \right\rangle = \left\langle \left[\hat{U}_l^-\right]^\dagger \hat{U}_l^+ \right\rangle = \left\langle \left[\hat{U}_l^+\right]^\dagger \hat{U}_l^- \right\rangle = \mathrm{Re}\left\{\left\langle \hat{W}_l \right\rangle\right\}$. In general, the CDD echo is $v_{\mathrm{CDD}} = \left\| \langle \hat{W}_l \rangle \right\| \geq \mathrm{Re}\left\{ \langle \hat{W}_l \rangle \right\}$, and we may therefore take this real part as a lower bound of coherence in the formulated problem. The measure of this "minimum" coherence is then given by

$$\begin{aligned} \mathrm{Re}\left\{\left\langle \hat{W}_l \right\rangle\right\} &= \frac{1}{2}\left\langle \left[\hat{U}_l^-\right]^\dagger \hat{U}_l^+ + \left[\hat{U}_l^+\right]^\dagger \hat{U}_l^- \right\rangle & (5.4) \\ &= 1 - \left\langle \Delta_l^\dagger \Delta_l \right\rangle, & (5.5) \end{aligned}$$

where we define $\Delta_l \equiv \hat{U}_l^+ - \hat{U}_l^-$ and note that $\hat{U}_l^{\pm}$ are unitary operators such that $\left[\hat{U}_l^{\pm}\right]^\dagger \hat{U}_l^{\pm} = \hat{\mathbb{1}}$. Thus, $\left\langle \Delta_l^\dagger \Delta_l \right\rangle$ gives a measure of the "maximum" decoherence. Applying the recursive definitions for the $\hat{U}_l^{\pm}$ evolution operators [Eq. (5.3)],

$$\hat{\Delta}_l \equiv \hat{U}_l^+ - \hat{U}_l^- = \left[\hat{U}_{l-1}^-, \hat{U}_{l-1}^+\right] = \left[\hat{U}_{l-1}^-, \hat{\Delta}_{l-1}\right], \tag{5.6}$$

noting that $\hat{U}_{l-1}^-$ commutes with itself.

Let us consider a perturbation with a smallness parameter λ in which $\hat{U}_l^{\pm} = \hat{\mathbb{1}} + \mathcal{O}(\lambda)$ for all $l \geq l_0$ for some l_0. Two such perturbations have $\lambda = \tau$, with

$l_0 = 0$, or $\lambda = \epsilon$, with $l_0 = 1$ (as long as $\hat{\mathcal{H}}_{b0}$ may be disregarded); we discuss these two perturbations in the context of CDD more specifically in Secs. 5.1.2 and 5.1.3 respectively. Because the identity commutes with anything, it is easy to see from Eq. (5.6) that $\hat{\Delta}_l = \mathcal{O}(\lambda) \times \hat{\Delta}_{l-1}$ for all $l > l_0$; this proves that we get successive cancellations of the low-order perturbation (τ or ϵ) with each concatenation of the sequence. The lowest order result is given by

$$\hat{\Delta}_l \approx \lambda \left[\frac{d}{d\lambda} \hat{U}^-_{l-1} \bigg|_{\lambda=0}, \hat{\Delta}_{l-1} \right], \ \forall\, l > l_0. \tag{5.7}$$

Conveniently, for all $l > l_0$,

$$\begin{aligned} \frac{d}{d\lambda} \hat{U}^{\pm}_l \bigg|_{\lambda=0} &= \frac{d}{d\lambda} \hat{U}^+_{l-1} \bigg|_{\lambda=0} + \frac{d}{d\lambda} \hat{U}^-_{l-1} \bigg|_{\lambda=0} \\ &= 2^{l-l_0} \frac{d}{d\lambda} \left(\hat{U}^+_{l_0} + \hat{U}^-_{l_0} \right) /2 \bigg|_{\lambda=0}, \end{aligned} \tag{5.8}$$

so that Eq. (5.7) becomes

$$\hat{\Delta}_l \approx \lambda \begin{cases} 2^{l-l_0-1} \left[\frac{d}{d\lambda} \left(\hat{U}^+_{l_0} + \hat{U}^-_{l_0} \right) /2 \Big|_{\lambda=0}, \hat{\Delta}_{l-1} \right] & , \ l > l_0 \\ \frac{d}{d\lambda} \left(\hat{U}^+_{l_0} - \hat{U}^-_{l_0} \right) \Big|_{\lambda=0} & , \ l = l_0 \end{cases} . \tag{5.9}$$

Note that in the $l = l_0 + 1$ case, Eq. (5.6) yields

$$\hat{\Delta}_{l_0+1} \approx \lambda^2 \left[\frac{d}{d\lambda} \hat{U}^-_{l_0}, \frac{d}{d\lambda} \hat{U}^+_{l_0} \right] \bigg|_{\lambda=0}, \tag{5.10}$$

which is equivalent to the corresponding case in Eq. (5.9) recalling that any operator commutes with itself.

5.1.2 Time Perturbation

In the case of the time perturbation, $\lambda = \tau$, we refer to the general $\hat{\mathcal{H}}_{\pm}$ Hamiltonians of Eq. (3.1) to see that $\hat{U}_0^{\pm}\Big|_{\tau=0} = \hat{\mathbb{1}}$ and

$$\frac{d}{d\tau}\left(\hat{U}_0^{+} + \hat{U}_0^{-}\right)/2\Big|_{\tau=0} = -i\hat{\mathcal{H}}_b. \tag{5.11}$$

Thus, Eq. (5.9), with $l_0 = 0$, yields

$$\hat{\Delta}_1 \approx \left[\frac{d}{d\tau}\hat{U}_0^{-}, \frac{d}{d\tau}\hat{U}_0^{+}\right]\Bigg|_{\tau=0} \tau^2 = 2\left[\hat{\mathcal{H}}_{qb}, \hat{\mathcal{H}}_b\right]\tau^2. \tag{5.12}$$

Applying the recursion of Eq. (5.9) then gives

$$\begin{aligned} \hat{\Delta}_l &= -2^{(l^2-l+2)/2}\left[...\left[\left[\hat{H}_{qb}, \hat{H}_b\right], \hat{H}_b\right], ...\right](i\tau)^{l+1} \\ &\quad + \mathcal{O}\left(\tau^{l+2}\right), \quad \forall\, l > 0, \end{aligned} \tag{5.13}$$

with l nested commutations abbreviated by ...'s. By computing the lowest-order time perturbation results [Eq. (5.13)] when calculating cluster contributions of the cluster expansion and comparing them with results from exact cluster contributions, we can test the applicability of this perturbation. In the results that we present in Ch. 6, we do make such comparisons and find that the τ perturbation is typically applicable for quantum dots with assumed Gaussian-shaped wave-functions but not for donor-bound electrons with exponential-shaped wave-functions. This will be discussed in more depth in Sec. 6.2.

A reasonable assumption for many solid-state spin baths is that the bath Hamiltonian, $\hat{\mathcal{H}}_b$, which excludes qubit-bath interactions, is homogeneous. That is, sites that are equivalent in terms of the Bravais lattice are equivalent with regard to bath interactions. A notable exception to this is where isotopes in the lattice are interchangeable; for example, three different isotopes of Si may occupy any lattice site in Si, and two different isotopes of Ga may occupy any Ga site in GaAs. However, if we simply want to know the decoherence that results from averaging different types of isotopic configurations, then we may regard the bath (apart from the qubit interactions) as homogeneous and use isotopic probabilities in expressions for $\hat{\mathcal{H}}_b$. Then the only inhomogeneity is in the interactions with the qubit, $\hat{\mathcal{H}}_{qb}$. We can then factor out this inhomogeneous part and compute the rest in a way that is independent of the qubit interactions. This will be convenient, for example, when analyzing a quantum dot in which the wave-function of the electron (whose spin represents the qubit) can take on many shapes and sizes.

If we take $\hat{\mathcal{H}}_{qb}$ to be the isotropic hyperfine interactions discussed in Sec. 3.2.3, $\hat{\mathcal{H}}_{qb} = \sum_n A_n \hat{I}_{nz}/2$, then we can make the following factorization of the homogeneous and non-homogeneous parts of $\left\langle \hat{\Delta}_l^\dagger \hat{\Delta}_l \right\rangle$:

$$\begin{aligned} \left\langle \hat{\Delta}_l^\dagger \hat{\Delta}_l \right\rangle &= (-)^{(l+1)} 2^{(l^2-l+2)} \sum_{n,m} A_n^* A_m f_{n,m}^{(l)} \tau^{2l+2} + \mathcal{O}\left(\tau^{2l+4}\right), \quad \forall\, l > 0, & (5.14) \\ f_{n,m}^{(l)} &\equiv \left\langle \left[..., \left[\hat{\mathcal{H}}_b^\dagger, \left[\hat{\mathcal{H}}_b^\dagger, \hat{I}_{nz} \right] \right] ... \right] \left[... \left[\left[\hat{I}_{mz}, \hat{H}_b \right], \hat{H}_b \right], ... \right] \right\rangle, & (5.15) \end{aligned}$$

where the ...'s again denote l nested commutations. The homogeneous part is represented by $f_{n,m}^{(l)}$, and exploiting this homogeneity, we note that this function is equivalent when we shift by any Bravais lattice vector, $\vec{R}$:

$$f^{(l)}(\vec{r}_n, \vec{r}_m) \equiv f_{n,m}^{(l)} = f^{(l)}(\vec{r}_n - \vec{R}, \vec{r}_m - \vec{R}). \tag{5.16}$$

The simplification of Eq. 5.14 can be particularly helpful to study the effect of quantum dot shape upon its decoherence as the electron wave-function dependency (the A_n's) is factored out. Of course, this is only helpful to the extent that a time perturbation provides an appropriate approximation.

5.1.3 Intra-bath Perturbation

We treat the intra-bath perturbation, with $\lambda = \epsilon$, by using the interaction representation for bath states. In the standard Schrödinger picture, the states of a quantum mechanical system evolve in time according to the time evolution operators (i.e., $\hat{U}^{\pm}$) while operators for observables remain constant. In the equivalent Heisenberg picture, the states remain constant, while the operators for observables evolve instead. In the interaction representation, the Hamiltonian is split up into an unperturbed part, $\hat{H}_0$, and an interaction (perturbation), $\hat{V}$; the observable operators then evolve according to $\hat{H}_0$ and the states evolve as necessary to incorporate the effects of $\hat{V}$. In our case, we consider bath states which evolve, in the Schrödinger representation, as $|\mathcal{B}^{\pm}(t)\rangle \equiv \hat{U}^{\pm}|\mathcal{B}_0\rangle$. For the intraction representation, we use $\hat{\mathcal{H}}_0^{\pm}(t) = \pm s(t)\hat{\mathcal{H}}_{qb} + \hat{\mathcal{H}}_{b0}$ where $s(0) = 1$ but $s(t)$ changes sign whenever a π-pulse is encountered in the evolution [Eq. (5.2)], and we use $\hat{V} = \epsilon\hat{\mathcal{H}}_{bb}$ in order to perform the perturbation expansion with respect to ϵ.

We can relate the interaction representation bath states to the corresponding Schrödinger states in the following way:

$$\text{Texp}\left(-i\int_0^t \hat{\mathcal{H}}_0^{\pm}(t')dt'\right)|\mathcal{B}_I^{\pm}(t)\rangle = |\mathcal{B}^{\pm}(t)\rangle, \tag{5.17}$$

where Texp is the time-ordering exponential operator, which, after taking the exponential of its argument via the expansion, $\exp(\hat{O}) = \sum_{n=0}^{\infty}\hat{O}^n/n!$, orders operators in increasing time order from right to left. In general for any time-dependent operator, $\hat{O}(t)$,

$$i\frac{\partial}{\partial t}\,\mathrm{Texp}\left(-i\int_0^t \hat{O}(t)dt'\right) = \hat{O}(t)\,\mathrm{Texp}\left(-i\int_0^t \hat{O}(t)dt'\right). \tag{5.18}$$

Then taking i times the partial derivative of both sides of Eq. (5.17) and invoking the Schrödinger equation, $i\frac{\partial}{\partial t}|\mathcal{B}^{\pm}(t)\rangle = \hat{H}^{\pm}(t)|\mathcal{B}^{\pm}(t)\rangle$,

$$\hat{\mathcal{H}}_0^{\pm}(t)|\mathcal{B}^{\pm}(t)\rangle + \mathrm{Texp}\left(-i\int_0^t \hat{\mathcal{H}}_0^{\pm}(t')dt'\right)\left[i\frac{\partial}{\partial t}|\mathcal{B}_I^{\pm}(t)\rangle\right] = (\hat{\mathcal{H}}_0^{\pm}(t) + \epsilon\hat{\mathcal{H}}_{bb})|\mathcal{B}^{\pm}(t)\rangle, \tag{5.19}$$

Therefore,

$$i\tfrac{\partial}{\partial t}|\mathcal{B}_I^{\pm}(t)\rangle = \hat{V}_I^{\pm}(t)|\mathcal{B}_I^{\pm}(t)\rangle, \tag{5.20}$$

$$\hat{V}_I^{\pm}(t) = \epsilon\left[\mathrm{Texp}\left(-i\textstyle\int_0^t \hat{\mathcal{H}}_0^{\pm}(t')dt'\right)\right]^{-1}\hat{\mathcal{H}}_{bb}\,\mathrm{Texp}\left(-i\textstyle\int_0^t \hat{\mathcal{H}}_0^{\pm}(t')dt'\right). \tag{5.21}$$

From this we derive the evolution operator in the interaction representation:

$$|\mathcal{B}_I^{\pm}(t)\rangle = \hat{U}_I^{\pm}(t)|\mathcal{B}_I^{\pm}(0)\rangle = \hat{U}_I^{\pm}(t)|\mathcal{B}_0\rangle, \tag{5.22}$$

$$\hat{U}_I^{\pm}(t) = \mathrm{Texp}\left[-i\int_0^t \hat{V}_I(t')dt'\right]. \tag{5.23}$$

This naturally yields perturbative orders by expanding the time-ordered exponential:

$$\hat{U}_I^{\pm}(t) = \sum_{n=0}^{\infty}\frac{1}{n!}\,\mathrm{T}\left[\left(-i\int_0^t \hat{V}_I(t')dt'\right)^n\right]. \tag{5.24}$$

After transforming back to the Schrödinger representation for a particular concatenated sequence,

$$\hat{U}_l^{\pm} = \mathrm{Texp}\left[-i\int_0^{2^l\tau}\hat{\mathcal{H}}_0^{\pm}(t')dt'\right]\hat{S}_l^{\pm}, \tag{5.25}$$

where we use $\hat{S}_l^{\pm}$ to denote the interaction picture evolution operator, $\hat{U}_I^{\pm}$, corresponding to the concatenated sequence [Eq. (5.2)] at level l. This notation is chosen because the interaction picture evolution operator is traditionally called the S-matrix; usually this implies evolution from $-\infty$ to ∞ in time with the perturbation turned on adiabatically, but we are clear here in what we mean (evolution for the duration of the pulse sequence). Using the fact that $s(t)$ is balanced in any of these pulse sequences, the $\hat{\mathcal{H}}_{qb}$ term cancels in the integral of Eq. (5.25) leaving

$$\hat{U}_l^{\pm} = \begin{cases} \exp\left[-i\left(\pm\hat{\mathcal{H}}_{qb} + \hat{\mathcal{H}}_{b0}\right)\tau\right]\hat{S}_0^{\pm}, & l = 0 \\ \exp\left[-2^l i\hat{\mathcal{H}}_{b0}\tau\right]\hat{S}_l^{\pm}, & l > 0 \end{cases} \tag{5.26}$$

By its construction, $\hat{S}^{\pm}(t) = \hat{\mathbb{1}} + \mathcal{O}(\epsilon)$; however, $\hat{U}_l^{\pm}$ is not generally of the form $\hat{\mathbb{1}} + \mathcal{O}(\epsilon)$ that we require to prove successive dynamical decoupling [Eq. (5.7)] unless $\hat{\mathcal{H}}_{b0} = 0$. Successive dynamical decoupling also results if $\hat{\mathcal{H}}_{b0}$ commutes with the Hamiltonian as a whole (in which case it is not relevant in the dynamics of the electron spin and can therefore be removed from the problem). For example, we may use the effective Hamiltonian of Eqs. (3.19) and (3.20), using the limit of a strong applied magnetic field.

Assuming that $\hat{\mathcal{H}}_{b0} = 0$ (or an irrelevant constant), we can equate the evolution operators in the Schrödinger and interaction representations, $\hat{U}_l^{\pm} = \hat{S}_l^{\pm}$, for CDD sequences with $l \geq 1$ according to Eq.(5.26). Using the general result of Eq. (5.9) for the lowest order of $\hat{\Delta} = \hat{U}_l^{+} - \hat{U}_l^{-}$ with $l_0 = 1$ [since $\hat{U}_l^{\pm} = \hat{\mathbb{1}} + \mathcal{O}(\epsilon)$ for $l \geq 1$], all we need to know is $\hat{U}_1^{\pm} = \hat{S}_1^{\pm}$ to the lowest order in ϵ. The interaction perturbation potential, V_I, for the Hahn echo sequence (with $\hat{\mathcal{H}}_{b0} = 0$) is given by

$$\hat{V}_I^{\pm}(t) = \epsilon \exp\left(-i\hat{\mathcal{H}}_{qb}(\tau - |\tau - t|)\right)\hat{\mathcal{H}}_{bb} \exp\left(i\hat{\mathcal{H}}_{qb}(\tau - |\tau - t|)\right), \tag{5.27}$$

so that

$$\begin{aligned} \hat{U}_1^{\pm} = \hat{S}_1^{\pm} &= \mathrm{Texp}\left[-i\epsilon \int_0^{2\tau} e^{\pm i\hat{\mathcal{H}}_{qb}(\tau - |\tau - t'|)} \hat{\mathcal{H}}_{bb} e^{\mp i\hat{\mathcal{H}}_{qb}(\tau - |\tau - t|)} dt'\right] & (5.28) \\ &= \hat{\mathbb{1}} - 2i\epsilon \int_0^{\tau} e^{\pm i\hat{\mathcal{H}}_{qb}t'} \hat{\mathcal{H}}_{bb} e^{\mp i\hat{\mathcal{H}}_{qb}t'} dt' + \mathcal{O}\left(\epsilon^2\right). & (5.29) \end{aligned}$$

We can use the above results in Eq. (5.9) with $\lambda = \epsilon$ and $l_0 = 1$ in order to obtain the lowest-order results of the intra-bath perturbation. By using the lowest-order intra-bath perturbation results in calculating cluster contributions of the cluster expansion and comparing them with results from exact cluster contributions, we can test the applicability of this perturbation. In the results that we present in Ch. 6, we do make such comparisons and generally find that the intra-bath perturbation is applicable roughly to the extent that the cluster expansion converges well.

5.1.4 Magnus Expansion

Dynamical decoupling is typically discussed in terms of its effect upon low orders of the Magnus expansion [13, 14, 18, 19, 15]. In the Magnus expansion, an evolution operator that is composed of a product of evolution operators (i.e., evolution of different parts of the pulse sequences) is expanded via repeated applications of the Baker-Campbell-Hausdorff relation [13]:

$$e^{\hat{B}} e^{\hat{A}} = \exp\left\{\hat{A} + \hat{B} + \frac{1}{2}\left[\hat{B}, \hat{A}\right] + ...\right\} \tag{5.30}$$

In this way, the evolution resulting from a time dependent Hamiltonian may be expanded as [19]

$$\hat{U}(t) = \exp \sum_{i=1}^{\infty} \hat{A}_i(t), \tag{5.31}$$

where

$$\begin{aligned} \hat{A}_1 &= -i \int_0^t dt_1 \hat{\mathcal{H}}(t_1), & (5.32) \\ \hat{A}_2 &= -\frac{1}{2} \int_0^t dt_1 \int_0^{t_1} dt_2 \left[\hat{\mathcal{H}}(t_1), \hat{\mathcal{H}}(t_2) \right], & (5.33) \end{aligned}$$

and each subsequent term in the exponential of Eq. (5.31) will involve another commutation and time integration. When dealing with π-pulse sequences, our time dependent Hamiltonians for $\hat{U}^{\pm}$ will be piecewise constant in time, alternating between $\hat{\mathcal{H}}_+$ and $\hat{\mathcal{H}}_-$ for time intervals of τ. Each integration will thus introduce a factor of τ in the corresponding term. In this way, the Magnus expansion can be viewed as a τ expansion for the logarithm of $\hat{U}^{\pm}$. Recalling the logarithmic form of our cluster expansion, Eq. (4.17), the Magnus expansion leads to an essentially equivalent perturbation as that of the time perturbation (Sec. 5.1.2) properly placed within the context of the cluster expansion (that is, the logarithm of the echo approximated as the sum of cluster contributions expanded up to the desired power of τ). For this reason, we do not discuss the Magnus expansion beyond pointing out this equivalence. We note, however, that while our time perturbation (in the cluster expansion context) emerges from the Magnus expansion alone, our intra-bath perturbation (Sec. 5.1.3) does not. Our computations results (Ch. 6) indicate that the intra-bath perturbation is generally applicable whenever we have found the cluster expansion to be convergent but our τ perturbation is not always applicable;

we therefore conclude that our cluster expansion does go beyond the Magnus expansion. Along these lines, our proof that each concatenation successively cancels low-order terms of the intra-bath perturbation goes beyond the previous [18, 43, 44] analyses of concatenation that relate to the Magnus expansion.

5.2 Periodic Dynamical Decoupling (e.g. CPMG)

In this section we consider the application of periodic pulse sequences. These sequences derive their strategy from the argument that repeating a series of decoupling pulses at a greater frequency than the pertinent dynamical frequencies of the system should prolong qubit coherence for extended times. The qubit and the bath are completely decoupled in the limit of infinitely many pulses in a finite amount time [15]. In the Carr-Purcell-Meiboom-Gill [25] sequence, illustrated in Fig. 1.4, a periodic train of π-pulses is applied in some direction perpendicular to the applied magnetic field; for an even number of pulses, it corresponds to repetitions of the second level of concatenation discussed above. We studied this sequence in Ref. [42] using our cluster expansion technique; we showed that, to the extent that the intra-bath perturbation is applicable, the log of the echo as a function of the intra-pulse time, τ, scales with the square of the number of pulses applied. While coherence, with more applied pulses, is enhanced as a function of the total elapsed time, it diminishes as a function of τ. Concatenation, on the other hand, can actually improve the performance as a function of τ as we will be demonstrated in Sec. 6.3.

Concatenation yields better performance because it yields successive cancellation of the lowest perturbative orders in the time and intra-bath perturbations. Repetition does not provide this cancellation; however, it is easy to show that the repetition of a given concatenation order will maintain the same lowest perturbative order. We can simply express the evolution operators for the periodic sequence, for n repetitions, as the corresponding concatenated sequence raised to the nth power. As in Sec. 5.1.1, we will consider an unpolarized bath as a limiting case (giving minimum coherence): $v_E = \left\|\hat{W}\right\| \geq \mathrm{Re}\left\{\langle\hat{W}\rangle\right\}$. Then we have

$$\begin{aligned}
\mathrm{Re}\left\{\langle\hat{W}\rangle\right\} &= \frac{1}{2}\left\langle\left[\left(\hat{U}_l^-\right)^\dagger\right]^n\left[\hat{U}_l^+\right]^n + \left[\left(\hat{U}_l^+\right)^\dagger\right]^n\left[\hat{U}_l^-\right]^n\right\rangle & (5.34)\\
&= 1 - \frac{1}{2}\left\langle\left[\Delta_l^{(n)}\right]^\dagger\Delta_l^{(n)}\right\rangle, & (5.35)
\end{aligned}$$

where

$$\begin{aligned}
\hat{\Delta}_l^{(n)} &\equiv \left(\hat{U}_l^+\right)^n - \left(\hat{U}_l^-\right)^n & (5.36)\\
&= \left(\hat{\Delta}_l + \hat{U}_l^-\right)^n - \left(\hat{U}_l^-\right)^n & (5.37)\\
&= \mathcal{O}\left(\hat{\Delta}_l\right). & (5.38)
\end{aligned}$$

The terms of $\Delta_l^{(n)}$ must contain at least one factor of Δ_l; therefore, when repeating a concatenated sequence of level l, it will maintain the low order perturbation properties of a single application. Repeating concatenated sequences can offer flexibility when it is not convenient to be constrained to having 2^l time segments in ones pulse sequence.

Chapter 6

Applications in Specific Systems

Applying our cluster expansion technique to study dynamical decoupling pulse sequences in specific systems is a matter of specifying appropriate $\hat{\mathcal{H}}_{qb}$, $\hat{\mathcal{H}}_{bb}$, and $\hat{\mathcal{H}}_{b0}$ Hamiltonians by supplying appropriate interactions and approximations as discussed in Sec. 3.2. Our first two applications, in Secs. 6.1 and 6.2, will consider a localized electron spin qubit in a Si or GaAs lattice, respectively. In the former case, the electron is bound to a P donor, and in the latter case, the electron is confined to a quantum dot via confining potentials of some sort. In these first two sections, we consider the Hahn echo decay, while in Sec. 6.3, we consider both PDD and CDD pulse sequences. In Sec. 6.4, we study the decoherence of a donor nucleus and disregard HF coupling to any electrons in the system. These applications have relevance for various quantum computing architectures, and it is therefore important to study the decoherence of their respective qubits and study the effects of dynamical decoupling.

Each of these applications are different in the way that the qubit interacts with the bath, $\hat{\mathcal{H}}_{qb}$. For the electron spin qubit, except when we consider the AHF interaction in Sec. 6.1.3, this qubit-bath Hamiltonian will be determined by the diagonal part of Fermi-contact HF [Eq. (3.19)]. We will neglect the HF-mediated interactions that couple non-local nuclear spins in the bath [Sec. 3.2.4] which is justified in the limit of a strong applied magnetic field, particularly for the pulse sequences we consider which reverse this effect; we will estimate the corresponding visibility loss [40, 56, 57] for each application. Unless otherwise stated, we use the secular part of the dipolar interaction [Eq. (3.20)] for the intra-bath interaction, $\hat{\mathcal{H}}_{bb}$, assuming the limit of a strong applied magnetic field in which $\hat{\mathcal{H}}_{b0}$ is irrelevant (beyond justifying the approximation). Except in Fig. 6.13 we do not include the indirect exchange interaction [Sec. 3.2.5] that can actually be comparable to the dipolar interaction for nearest neighbors in GaAs; any such local intra-bath interaction is easily included in framework but the indirect exchange interaction does not appear to make a qualitative difference.

For the initial state of the bath, we assume thermal equilibrium in the limit of high nuclear temperatures and thus use a uniform distribution of bath states. This is well justified when $T \gg$ mK (see Sec. 3.2.6); in the mK temperature range, one should account for polarization in the nuclear bath which could diminish the SD decoherence (or enhance the coherence).

6.1 Phosphorus Donor in Silicon

Our first application is to consider the decoherence of an electron spin of a phosphorus donor in natural silicon [35, 34, 37]. Here we take $\Psi(\boldsymbol{R}_n)$ to be the Kohn-Luttinger wave-function of a phosphorus donor impurity in silicon based upon an effective mass approximation. This will determine the HF coupling constants, A_n [Eq. (3.10)], responsible for the qubit-bath interaction, $\hat{\mathcal{H}}_{qb} = \sum_n A_n \hat{I}_{nz}/2$. We have [35]

$$
\begin{aligned}
A_n &= \frac{16\pi}{9}\gamma_S\gamma_I^{Si}\hbar\eta\left[F_1(\boldsymbol{R}_n)\cos(k_0X_n)\right. && (6.1)\\
&\left.+F_3(\boldsymbol{R}_n)\cos(k_0Y_n)+F_5(\boldsymbol{R}_n)\cos(k_0Z_n)\right]^2\\
&-\gamma_S\gamma_I^{Si}\hbar\frac{1-3\cos^2\theta_n}{|\boldsymbol{R}_n|}\Theta(|\boldsymbol{R}_n|-na),\\
F_{1,2}(\boldsymbol{r}) &= \frac{\exp\left[-\sqrt{\frac{x^2}{(nb)^2}+\frac{y^2+z^2}{(na)^2}}\right]}{\sqrt{\pi(na)^2(nb)}}, && (6.2)
\end{aligned}
$$

with $\gamma_S = 1.76\times10^7(\text{s G})^{-1}$, $\gamma_I^{Si} = 5.31\times10^3(\text{s G})^{-1}$, $n = 0.81$, $a = 25.09$ Å, $b = 14.43$ Å, $\eta = 186$, $k_0 = (0.85)2\pi/a_{Si}$, and $a_{Si} = 5.43$ Å. The $F_{3,4}(\boldsymbol{r})$ and $F_{5,6}(\boldsymbol{r})$ functions are defined via respective permutations of x, y, and z in Eq. (6.2). The Si nuclei are located on a diamond lattice [62]. The central ^{31}P nuclear spin does not contribute to SD because its HF energy is significantly larger than any of its neighbors, suppressing the spin flips by energy conservation.

In a natural sample of silicon, only a small fraction $f = 4.67\%$ of lattice sites have nonzero nuclear spin. These are the spin-1/2 ^{29}Si isotopes, therefore $I_n = 1/2$ for all contributing nuclei. We will use $\langle\Sigma_k(\tau)\rangle$ and $\langle\Sigma_k^*(\tau)\rangle$ to denote $\Sigma_k(\tau)$ and $\Sigma_k^*(\tau)$ averaged, respectively, over isotopic configurations with a fraction, f, of ^{29}Si. We will also use the convention that $\Sigma_k(\tau)$ and $\Sigma_k^*(\tau)$ without these angle brackets gives the $f = 100\%$ result. Thus

$$
\begin{aligned}
\langle\Sigma_k(\tau)\rangle &= f^k\Sigma_k(\tau), && (6.3)\\
\langle\Sigma_k^*(\tau)\rangle &= f^k\Sigma_k^*(\tau), && (6.4)
\end{aligned}
$$

where $\Sigma_k(\tau)$, $\Sigma_2^*(\tau)$, and $\Sigma_3^*(\tau)$ are given by Eqs. (4.18), (4.19), and (4.20), respectively, taking all nuclei to be ^{29}Si. The fact that only a fraction, f, of these nuclei contribute to the diffusion is accounted for by the f^k factors in Eqs. (6.3) and (6.4) because f^k is the probability that all nuclei in a cluster of size k have nonzero spin.

We will justifiably neglect the HF-mediated interactions (Sec. 3.2.4) because their effects are reversed in the Hahn echo (or other DD sequences), at least in the pair approximation; also, the visibility decay associated with the HF-mediated interactions is estimated as $\sum_n f(A_n/\Omega_n)^2 \sim 10^{-5} \times f$ for an applied field strength of $B = 0.35$ T (to correspond with the experimental data to which we compare our results).

6.1.1 Hahn echo spectral diffusion

For the spin-1/2 nuclei that contribute to the Hahn echo, we can write the following analytical solution for pairs (2-clusters):

$$\begin{aligned} v_{nm}(\tau) &= 1 + v'_{nm}(\tau) \\ &= 1 - \frac{c_{nm}^2}{(1+c_{nm}^2)^2}\left[\cos\left(\omega_{nm}\tau\right) - 1\right]^2, \qquad (6.5) \\ \omega_{nm} &= 2b_{nm}\sqrt{1+c_{nm}^2}, \qquad (6.6) \\ c_{nm} &= \frac{A_n - A_m}{4b_{nm}}, \qquad (6.7) \end{aligned}$$

This can be obtained by evaluating $v_{\text{Hahn}} = \left\langle \left[\hat{U}_0^+\hat{U}_0^-\right]^\dagger \hat{U}_0^-\hat{U}_0^+ \right\rangle$ with τ as the implicit inter-pulse time ($\hat{U}_0^+ \equiv \hat{U}_0^+(\tau)$) and using a uniform initial bath distribution.

Our numerical calculations of Hahn echo decay in the lowest order of the cluster expansion, $v_E^{(2)}(\tau) = \exp\left(\langle\Sigma_2(\tau)\rangle\right)$ using Eqs. (6.3), (4.18), and (6.5), are shown for several magnetic field orientation angles in Fig. 6.1(a) with a direct quantitative comparison to the experiment [36]. The dipolar coupling [Eq. (3.7)] contains an

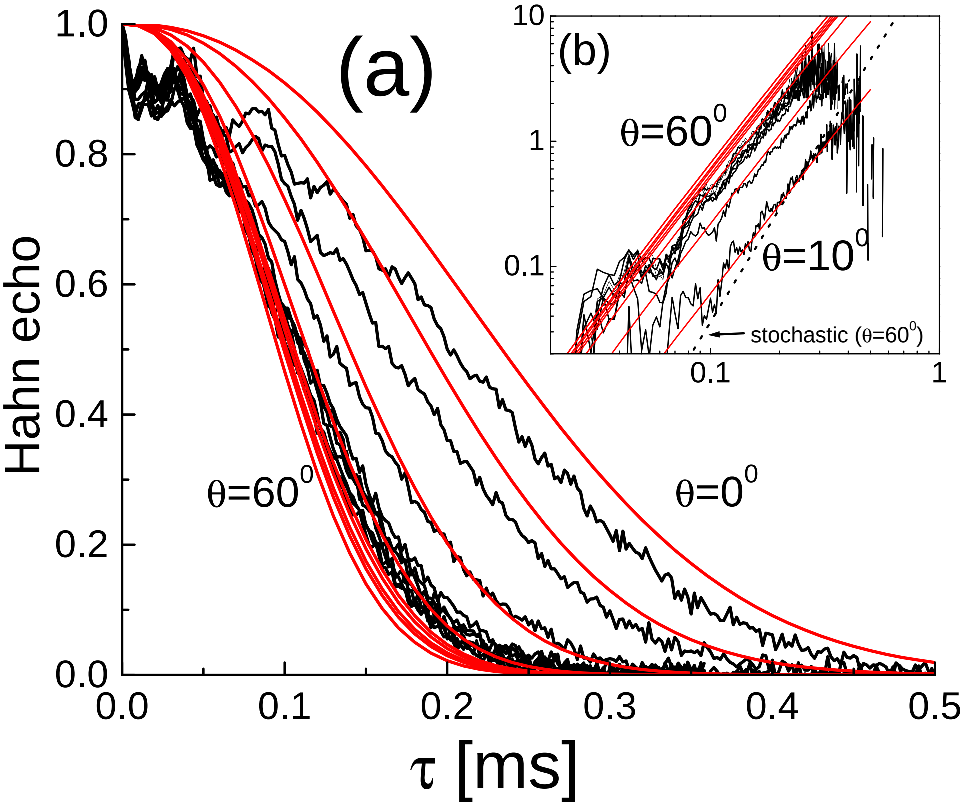

Figure 6.1: Hahn echo decay $v_E(\tau, \theta)$ of a phosphorus donor electron spin in silicon due to the dipolar nuclear spin bath dynamics. (a) Theory (solid lines) and experiment (Ref. [36]) is shown for several orientation angles of the magnetic field with respect to the crystal lattice, ranging from the [100] to the [110] direction ($\theta = 0, 10, 20, \ldots, 90$). (b) Here we plot $-\ln v_E(\tau, \theta) + \ln v_E(\tau, \theta = 0)$, allowing for the removal of any decoherence mechanism which is independent of θ. The qualitative and quantitative agreement between theory and experiment is remarkable, in contrast to the stochastic approach (dashed) of Ref. [35].

important anisotropy with respect to the θ_{nm} angle formed between the applied magnetic field and the bond vector linking the two spins ($\boldsymbol{R}_{nm}$). This property leads to a strong dependence of spin echo decay when the sample is rotated with respect to the applied B field direction. The experimental data is taken for bulk natural silicon with phosphorus doping concentration equal to 2×10^{15} cm^3 [36]. The high concentration of phosphorus donors leads to an additional decoherence channel arising from the direct spin-spin coupling between the electron spins that contribute to the echo. This contribution can be shown to contribute a multiplicative factor $\exp(-\tau/1\,\mathrm{ms})$ to the Hahn echo [63]. Because this contribution is independent of the orientation angle, we can factor it out by subtracting the $\theta = 0$ contribution from the logarithm of the experimental data taken at angle θ. The result is shown in Fig. 6.1(b) (log-log scale). Our theory seems to explain the time dependence of the experimentally observed echo quite well. This result is to be compared with the recent stochastic theory of Ref. [35] [Dashed line in Fig. 6.1(b) shows the stochastic calculation for $\theta = 60°$]. Although the stochastic theory, which assumes a particular probability distribution of nuclear flip-flop rates, yields roughly correct coherence times in order of magnitude, it fails qualitatively in explaining the time dependence [that is, the shape of the decay as can be seen from the incorrect slope of the stochastic calculation in the log-log plot of Fig. 6.1(b)]. The present method is able to incorporate all these features within a fully microscopic framework, obtaining both qualitative and quantitative agreement with experiment. Most importantly, it does this without *any* fitting parameters; we solely use well-established values of magnetic moments for the interacting spins and an effective mass theory-derived electron wave-function [determining Eq. (6.1)].

An important issue in the context of quantum information processing is the behavior of spin coherence at the shortest time scales. The experimental data [36] in Fig. 6.1 reveals several oscillatory features which are not explained by our current method. These are echo modulations arising from the AHF coupling and will be discussed in Sec. 6.1.3 where we show how to substantially reduce this effect by adjusting the strength and direction of the applied magnetic field and properly time the pulse sequence.

Isotopic purification can reduce the value of f (fraction of ^{29}Si nuclei). Figure 6.2 contains information that is useful for understanding how the Hahn echo curves change as f is changed (i.e., lowered via isotopic purification). In a log-log plot, $\ln(v_E(\tau)) \approx \langle \Sigma_2(\tau) \rangle \propto f^2$ simply shifts vertically when f is changed. Figure 6.2 shows both the f-independent $\Sigma_2(\tau)$ (i.e., $f = 100\%$), and $\langle \Sigma_2(\tau) \rangle$ for natural Si ($f \sim 5\%$). Results are shown for magnetic field angles that yield the extremal slowest and fastest decoherence. For natural Si, in a wide range of τ about $\tau_{1/e}$, where $v_E(\tau_{1/e}) = 1/e$, $\langle \Sigma_2(\tau) \rangle$ matches $\tau^{2.3}$ curves very well. In this range of τ, therefore, we may write

$$\begin{aligned} v_E(\tau) &\approx \exp\left(-f^2 (\tau/\tau_0)^{2.3}\right) && (6.8) \\ &= \exp\left(-(\tau/\tau_{1/e})^{2.3}\right), && (6.9) \end{aligned}$$

where

$$\tau_{1/e} = \tau_0 / f^{2/2.3} \propto f^{-0.87}, \tag{6.10}$$

providing a formula that allows us to adjust our Hahn echo curves to other val-

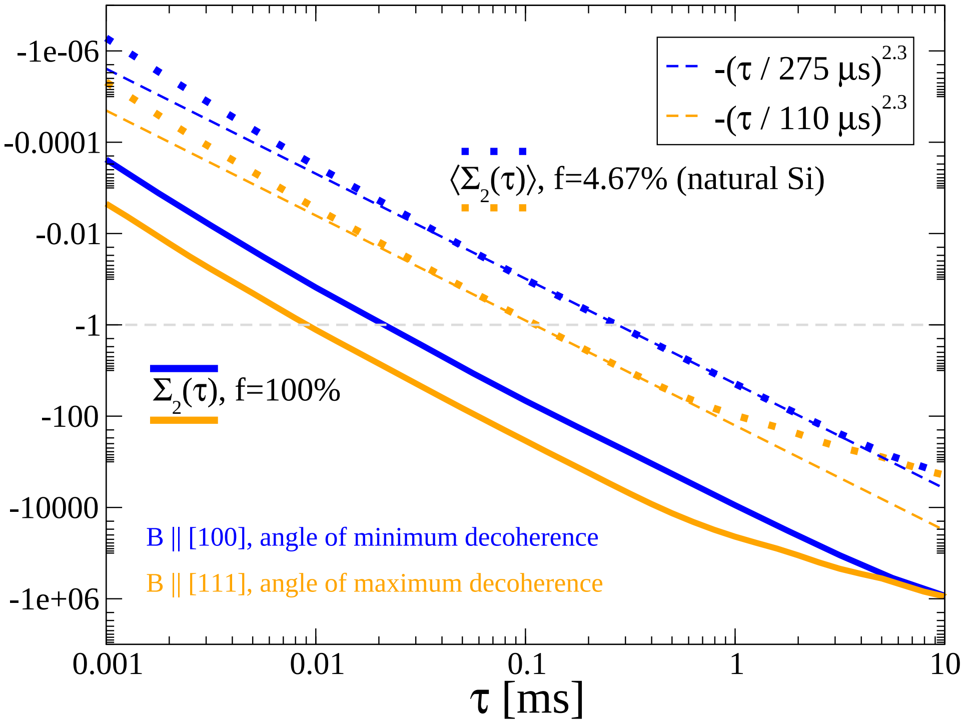

Figure 6.2: Lowest order theoretical results for the natural log of the Hahn echo, $\ln\left(v_E(\tau)\right) \approx \langle \Sigma_2(\tau) \rangle \propto f^2$, for Si:P in a log-log plot. The solid lines give $\Sigma_2(\tau)$ with $f = 1$. Dotted lines give $\langle \Sigma_2(\tau) \rangle$ for natural Si ($f = 4.67\%$). In this log-log plot, multiplying by f^2 simply shifts the curves vertically. Isotopic purification would shift these curves up further. The two magnetic field angles shown give extremal results. Corresponding to θ angles in Fig. 6.1, $B \parallel [100]$ is $\theta = 0°$ and $B \parallel [111]$ is $\theta \approx 54.7°$. Dashed lines fit the natural Si curves near their -1 values (where $v_E \sim 1/e$) with $\tau^{2.3}$ power law curves (linear in the log-log plot).

ues of f for a range of τ in which Eq. (6.8) is applicable. This scaling behavior was predicted in our original submission of Ref. [41] and was confirmed shortly thereafter in the literature [64] from experimental data produced by Abe *et al.* showing echo time scaling ranging between $f^{-0.86}$ and $f^{-0.89}$, in remarkable agreement with our prediction [Eq. (6.10)]. Tyryshkin *et al.* [36] report Si:P Hahn echo decay forms of $\exp\left(\tau^{2.4\pm0.1}\right)$, in agreement with Eq. (6.8), with exception to magnetic field orientations near the [100] direction. In the [100] direction, they report a form of $\exp\left(\tau^{3.0\pm0.2}\right)$. By incorporating the effect of AHF interactions which produces the modulations of the echo, the agreement is somewhat improved as shown in Sec. 6.1.3.1.

6.1.2 Cluster expansion convergence

We now check the convergence of our cluster expansion for this Si:P system. Using Eq. (4.22) and averaging over the isotopic configurations yields

$$\ln\left(v_E^{(k)}(\tau)\right) = \sum_{j=2}^{k} \langle \Sigma_j(\tau) \rangle + \mathcal{O}\left(\langle \Sigma^*(\tau) \rangle\right). \tag{6.11}$$

This approximates the ideal cluster expansion [see Secs. 4.3.2 and 4.3.3] with an error that we may estimate as $\langle \Sigma^*(\tau) \rangle = \langle \Sigma_2^*(\tau) \rangle + \langle \Sigma_3^*(\tau) \rangle$. This error is estimated by the correction needed to compensate for overlapping pairs [either the same pair overlapping itself, $\Sigma_2^*(\tau)$, or two different pairs overlapping, $\Sigma_3^*(\tau)$] in the approximation. Figure 6.3 shows these relative corrections, $\Sigma_2^*(\tau)/\Sigma_2(\tau)$ and $\Sigma_3^*(\tau)/\Sigma_2(\tau)$, to $\ln\left(v_E(\tau)\right)$ for both $f = 100\%$ and natural Si ($f \sim 5\%$). The graphs also show the respective Hahn echoes (in a log time scale which alters their appearance) to

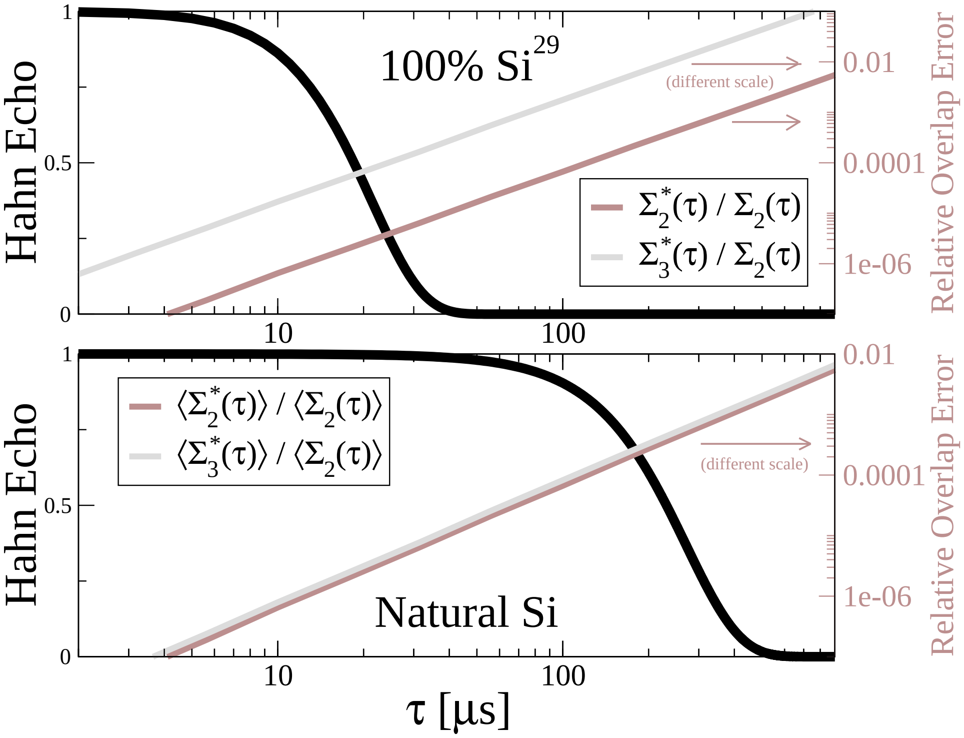

Figure 6.3: Relative errors (with scales on the right) to the log of the Hahn echo due to overlapping pairs for both 100% ^{29}Si (top graph) and natural Si (bottom graph). In these examples, $B \parallel [100]$. The Hahn echoes themselves are shown, as well, with the 0 to 1 scales on the left. All curves share the same logarithmic time (τ) scale. It is apparent that these relative corrections are very small up to the tail of their respective echo decays.

show that these relative corrections are very small up to the tail of their respective echo decays. The argument, given in Sec. 4.3.3, that $\Sigma^*(\tau)$ would be small was only applicable for $v_E(\tau) \gtrsim e^{-1}$ so it is expected that this approximation approaches failure out in the tail of the decay. This is irrelevant for practical purposes.

The expansion of Eq. (6.11) is convergent where $\langle \Sigma_{k+1}(\tau) \rangle \ll \langle \Sigma_k(\tau) \rangle$ (implying that $\lambda L \ll 1$ effectively). The $\Sigma_k(\tau)$ functions have been calculated (up to $k = 5$) using statistical sampling (Monte-Carlo) techniques with cluster contributions, $\langle \hat{W}'_{\mathcal{C}} \rangle$, for clusters that are larger than pairs, calculated by numerically diagonalizing $\hat{\mathcal{H}}_{\pm}$ [Eq. (3.1)]. For each $\Sigma_k(\tau)$ independently, the maximum distance between neighbors and the maximum distance of nuclei to the donor is increased for various Monte-Carlo runs until convergence within a desired precision is reached. To speed up each Monte-Carlo run, clusters are chosen with a heuristic bias for those that have strong coupling between the constituent nuclei as well as a bias for clusters closer to the donor. Appropriate weighting factors are used to counteract these biases.

Figure 6.4 compares f-independent (i.e., $f = 100\%$) $\Sigma_k(\tau)$ functions in a dual (showing positive and negative values) log-log plot for Si:P with $B \,||\, [100]$. In other words, it compares successive orders of the expansion for the natural log of the Hahn echo, $\ln(v_E(\tau))$, with the f dependence removed. As one might anticipate by the fact that $\Sigma_3(\tau)$ and $\Sigma_4(\tau)$ are both $\mathcal{O}(\lambda^4)$ (Ref. [41] proves that there are no odd orders of λ for either perturbation theory), they are similar orders of magnitude, at least for the 0.03 ms $< \tau < 1$ ms range. Near $\tau \sim 1$ ms, however, the perturbation theory fails [having the condition that $\max(b_{nm})\tau \ll 1$] as we see that $|\Sigma_4(\tau)|$

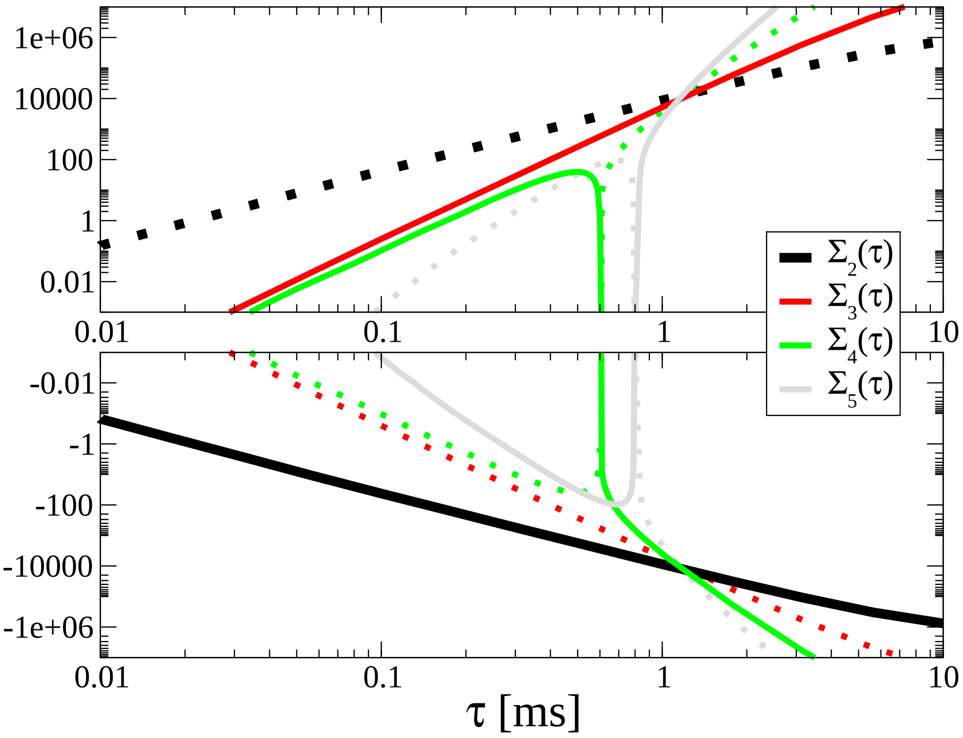

Figure 6.4: Successive contributions to the cluster expansion for the natural log of the Hahn echo [Eq. (6.11)], computed for Si:P and $B \parallel [100]$, for the 100% ^{29}Si theoretical scenario. The thick black line gives the lowest order result, $\Sigma_2(\tau)$, and other solid lines give higher order $\Sigma_k(\tau)$ results. The dotted lines give the negative of their corresponding functions provided to assist in the absolute value comparison of these higher order corrections. A failure of convergence occurs near $\tau \sim 1$ ms where all of the curves are the same order of magnitude. This occurs well into the tail of the decay, however, and therefore has no practical consequence.

surpasses $|\Sigma_3(\tau)|$. Interestingly, all orders approach the same order of magnitude near $\tau \sim 1$ ms. We can thus identify the breakdown of the cluster expansion. Note, however, that this is well into the tail of the decay [where $v_E(\tau) < e^{-1000}$] and therefore this breakdown is irrelevant for practical purposes. It is prudent, in any case, to understand the limitations of this expansion.

The $\langle \Sigma_k(\tau) \rangle$ curves for some fraction, f, of ^{29}Si will be the same as the $\Sigma_k(\tau)$ curves in the log-log plots of Fig. 6.4 except with appropriate vertical shifts [multiplying by f^k effectively appears as addition by $k \log(f)$ in the log plot] due to the f dependence. Higher orders will be shifted closer to zero than the lower order curves and therefore these curves will be more separated (actually improving the cluster expansion convergence). The top graph of Fig. 6.5 is analogous to the bottom (negative range) graph of Fig. 6.4 for natural Si (dashed lines indicate negated curves, i.e., where values are actually positive). We show only the low-order corrections to the log of the Hahn echo, including $\langle \Sigma^*(\tau) \rangle$ as well as $\langle \Sigma_3(\tau) \rangle$ and $\langle \Sigma_4(\tau) \rangle$ and not bothering with $\langle \Sigma_5(\tau) \rangle$. $\langle \Sigma_3(\tau) \rangle$, with its inclusion of 3-cluster, gives the largest correction. Although $\Sigma^*(\tau)$ is of a comparable order of magnitude, its correction partially cancels the $\Sigma_3(\tau)$ correction because they are opposite in sign. We may therefore use $\Sigma_3(\tau)$ for a conservative estimate of the error of the lowest order cluster expansion result. The bottom graph of Fig. 6.5 shows the absolute (as opposed to relative) error of the lowest order Hahn echo result estimated by the inclusion of $\Sigma_3(\tau)$. The Hahn echo is displayed for reference. At its maximum, this absolute error is approximately 0.001. Although our cluster expansion fails near $\tau \sim 5$ ms [where $|\langle \Sigma_2(\tau) \rangle| \sim |\langle \Sigma^*(\tau) \rangle| \sim |\langle \Sigma_3(\tau) \rangle| \sim |\langle \Sigma_4(\tau) \rangle|$], the absolute error will stay

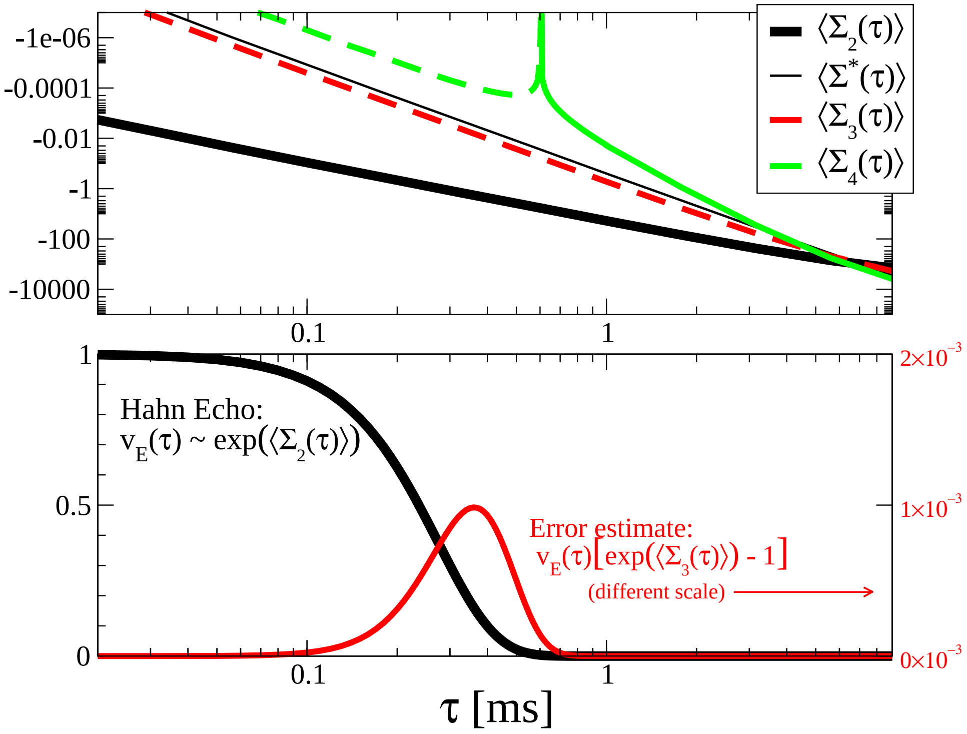

Figure 6.5: Successive contributions to the cluster expansion of the Hahn echo, $v_E(\tau)$, computed for Si:P in natural Si ($f = 0.0467\%$) with $B \parallel [100]$. (top) Log-log plot of low-order contributions to the natural log of the Hahn echo, $\ln(v_E(\tau))$. Ordinate axis is negative as in the bottom graph of Fig. 6.4; however, dashed lines indicate negated curves (and thus represent positive values). (bottom) Conservative estimate of the absolute error of the lowest order Hahn echo result (scale on the right) due to 3-cluster contributions, $\langle\Sigma_3(\tau)\rangle$. The lowest order Hahn echo result is shown as a reference (scale on the left). The logarithmic time scale is the same for all plots (top and bottom).

small if we assume that our Hahn echo decay is forever monotonically decreasing. For all practical purposes, the lowest order result is therefore valid up to 0.1% of the initial $v_E(0) = 1$, and higher order terms only provide corrections beyond 99.9% accuracy level.

To better understand the reasons for cluster expansion convergence, we have also compared cluster expansion results where we compute cluster contributions exactly versus computing them in the lowest order of the intra-bath perturbation (see Sec. 5.1.3). The agreement in these comparisons clearly shows that the credit for cluster expansion convergence goes to this intra-bath perturbation (larger clusters can only contribute higher orders in this perturbation as noted in Sec. 4.2). The clusters for which the intra-bath perturbation is most applicable are those with the largest differences in the HF interactions among the nuclei such that $c_{nm} \sim (A_n - A_m)/b_{nm} \gg 1$. Since the intra-bath coupling is essentially homogeneous, the clusters with the largest differences in their HF interactions will have the highest frequency dynamics and thus will operate at the shortest time-scales and dominate the echo decay. This is essentially the reason that the cluster expansion converges over the relevant decoherence time-scale. In Si:P, the τ perturbation only serves to keep the clusters with slower dynamics “under control” so that we are safe to disregard the larger ones (that is, pairs with slow dynamics have little effect upon the echo decay and 3-clusters with slow dynamics have even less of an effect). In Sec. 6.2, however, we find that the τ perturbation plays a more significant role in GaAs quantum dots.

6.1.3 Anisotropic hyperfine modulations and comparison with experiment

As was discussed in Sec. 3.2.3, the HF interaction between the spin of an electron and nucleus can contain anisotropic parts due to a dipolar interaction between the electron and nucleus as it is averaged over the electron wave-function. Because the conduction band minimum for Si occurs close to the X-point of the Brillouin zone so that the electron Bloch function has significant contributions from p- and d-atomic-orbitals [51, 52], the HF interaction between an electron near the conduction band minimum, such as an electron confined to a donor or a quantum dot, and the surrounding nuclear spins has strong anisotropic characteristics. Indeed, AHF interaction has been studied extensively in the Si:P system in the 1960s and 1970s. The strength of AHF has been accurately measured and calculated for the phosphorus donor electron [51]. In the context of solid state spin quantum computation, however, much of the existing literature only takes into account the contact HF [first term in Eq. (3.8)] in considering electron spin decoherence.

In Ref. [70] and in this section, we analyze how the AHF interactions leads to spin decoherence by considering a single P donor and donor-bound electron in Si interacting with the P and ^{29}Si nuclear spins. We assume the limit of a strong magnetic field ($>$ 100 mT is sufficient) applied in the z direction such that electron spin flips are suppressed due to its large Zeeman energy. Since $\gamma_S \gg \gamma_I$, it is appropriate to take the limit where S_z is conserved but not I_z (of any nucleus). In this limit we write the Hamiltonian (in $\hbar = 1$ units) as $\hat{\mathcal{H}} = \hat{\mathcal{H}}_0 + \sum_n \hat{\mathcal{H}}_n$ with

$$\hat{\mathcal{H}}_0 = \omega_S \hat{S}_z + A_P \hat{S}_z \hat{I}_z^P - \omega_P \hat{I}_z^P, \tag{6.12}$$

$$\hat{\mathcal{H}}_n = A_n \hat{S}_z \hat{I}_{nz} + B_n \hat{S}_z \hat{I}_{nx'} - \omega_I \hat{I}_{nz}. \tag{6.13}$$

We separate the Hamiltonian into $\hat{\mathcal{H}}_0$, involving the electron Zeeman energy and the donor nucleus, and $\hat{\mathcal{H}}_n$, involving the nth ^{29}Si nucleus in the surrounding lattice (other Si isotopes have zero spin). In our notation, $\hat{\boldsymbol{S}}$, $\hat{\boldsymbol{I}}^P$, and $\hat{\boldsymbol{I}}_n$ denote spin operators of the electron, P nucleus, and ^{29}Si nucleus n respectively, and $\hat{I}_{nx'}$ gives the nuclear spin operator with x'-axis oriented so that there is no $\hat{S}_z \hat{I}_{ny'}$ contribution (having a different orientation for each n). Given an applied magnetic field strength of B, we define $\omega_\Box = \gamma_\Box B$ as the Zeeman frequency for the electron, P nucleus, or a ^{29}Si nucleus with $\Box = S, P,$ or I respectively. A_P denotes the HF coupling between the electron and the P nucleus. Both contact HF as well as the $\hat{S}_z \hat{I}_z$ part of the AHF interaction are contained in A_n. The remaining AHF interaction in our strong field limit is contained in B_n and gives the relevant anisotropy mixing different directional components of $\hat{\boldsymbol{S}}$ and $\hat{\boldsymbol{I}}$.

Qualitatively, the anisotropic term, $B_n \hat{S}_z \hat{I}_{nx'}$, in $\hat{\mathcal{H}}_n$ dictates that the quantization axis for the precession of the ^{29}Si nuclear spin is dependent upon the state of the electron spin; conversely, the electron spin is affected by the precession of the nuclear spin. The resulting electron spin free induction decay (FID) in Si:P has been explored in Ref. [71], which shows that the donor electron spin could lose more than 1% of its coherence *only* after about 10 μs if a ^{29}Si atom is in one of the nearest neighbor (E-shell) sites. This will be disastrous for quantum computation, where the error rate must stay below 10^{-4}.

A key question, addressed in Sec. 6.1.3.2, is whether this AHF-induced decoherence effect can be removed/suppressed. It is well-known that spin echo techniques such as Hahn echo can be used to remove dephasing caused by the spatial variation of local magnetic fields (the inhomogeneous broadening). However, the AHF-induced FID is a dynamical effect and, as such, cannot be removed by Hahn echo. Instead AHF causes the echo envelope to oscillate, which is known within the electron spin resonance community as Electron Spin Echo Envelope Modulation (ESEEM) [65, 66, 67]. Our focus in this section is to study ESEEM in the Si:P system [36, 37, 68] and explore possible ways to significantly reduce the decoherence effect of AHF interaction with ^{29}Si in the context of spin quantum computation.

This AHF-induced ESEEM effect is observed in Hahn echoes of the Si:P system along with the effect of SD studied in Sec. 6.1.1 and was the cause of the modulations in Fig. 6.1; in Sec. 6.1.3.1 we will show how well the experimental results can be explained when we combine the theories of ESEEM and SD. In terms of our cluster expansion, ESEEM can be thought of as a 1-cluster contribution, caused by interactions with individual nuclei that are near the donor nucleus. These near nuclei give a negligible contribution to SD (they are few in number, and the strong HF coupling close to the center of the electron wave-function freezes out flip-flop interactions). We can therefore factor out this 1-cluster AHF effect from the 2-cluster SD effect and compose the Hahn echo as the product of the two. Treating the AHF problem independently from SD, then, we can neglect the intra-nuclear interactions;

the free evolution of the system is therefore factorable into

$$\hat{U}_0 = \exp\left(-i\sum_n \hat{H}_n\tau\right) = \prod_n \exp\left(-i\hat{H}_n\tau\right) = \hat{U}_0^{+}|\uparrow\rangle\langle\uparrow| + \hat{U}_0^{-}|\downarrow\rangle\langle\downarrow| \tag{6.14}$$

because the $\hat{H}_n$ Hamiltonians commute with each other. The $\hat{U}_0^{\pm}$ operators are the evolutions of the bath given an electron spin that is up or down. Because $\hat{U}_0$ factorizes independently for each nucleus in the bath, the ESEEM due to each nucleus factors independently into the echo of Eq. 3.24 (with $\hat{U}^{\pm}_{\text{Hahn}} = \hat{U}_0^{\mp}\hat{U}_0^{\pm}$ for the Hahn echo sequence we consider here). Given that only some fraction, f, of the Si nuclei have non-zero spin (^{29}Si), we have the following ESEEM, derived from Eq. 3.24 averaged with respect to isotope configurations [65, 69]:

$$\begin{aligned} V(\tau) &= \prod_n \left[(1-f) + fV_n(\tau)\right], && (6.15)\\ V_n(\tau) &= 1 - \frac{k_n}{2}\left(1-\cos\left(\omega_{n+}\tau\right)\right)\left(1-\cos\left(\omega_{n-}\tau\right)\right), && (6.16)\\ \omega_{n\pm} &= \sqrt{\left(\pm\frac{A_n}{2} - \omega_I\right)^2 + \left(\frac{B_n}{2}\right)^2}, && (6.17) \end{aligned}$$

and $k_n = \left(\omega_I B_n\right)^2 / \left(\omega_{n+}\omega_{n-}\right)^2$ is called the modulation depth parameter in the literature [69]. The maximum modulation (deviation from one) of $V_n(\tau)$ is $2k_n$ so that k_n is a measure of modulation amplitude. To obtain the results shown in the following sub-sections, we used experimentally determined contact and AHF coupling constants for 22 nuclear shells (which include about 150 symmetry-related nuclear sites) taken from Ref. [51].

6.1.3.1 Remarkable agreement with experiment

By incorporating AHF-induced ESEEM with our theoretical results for SD [Sec. 6.1.1], we are able to obtain excellent agreement between theory and experiment. Figure 6.6(c) shows excellent agreement of our ESEEM calculations with experiment, though it does use five separate fitting parameters: normalization, strain distribution width, relaxation time, SD time, and a SD exponent. The first three of these parameters (described momentarily) may be fixed for all different directions of the applied magnetic field; thus, in Fig. 6.7, which shows comparison with experiment for ten different magnetic field directions, we use only two fitting parameters per curve. These two fitting parameters characterize the SD decay and are compared with the results of Sec. 6.1.1 in Fig. 6.8. Considering that we use an approximation for the electron wave-function in Sec. 6.1.1, the agreement is quite good. There does appear to be, however, some discrepancy between the fit and the theory for the SD exponent when the applied field nears the [001] lattice direction; theory expects $n = 2.3$ and the fit yields $n = 2.5$. It is probably not coincidental that the nearest neighbor dipolar coupling vanishes when the applied field points along the [001] direction. Perhaps we have overlooked some interaction that becomes important when the dipolar interaction is weak.

We now describe the fitting parameters in more detail. The AHF-induced ESEEM for a single electron spin is shown in Fig. 6.6(a). Strain effects result in narrow distributions for the values of HF coupling constants and/or Zeeman frequencies and effectively dampen this signal for an ensemble of spins. This is shown

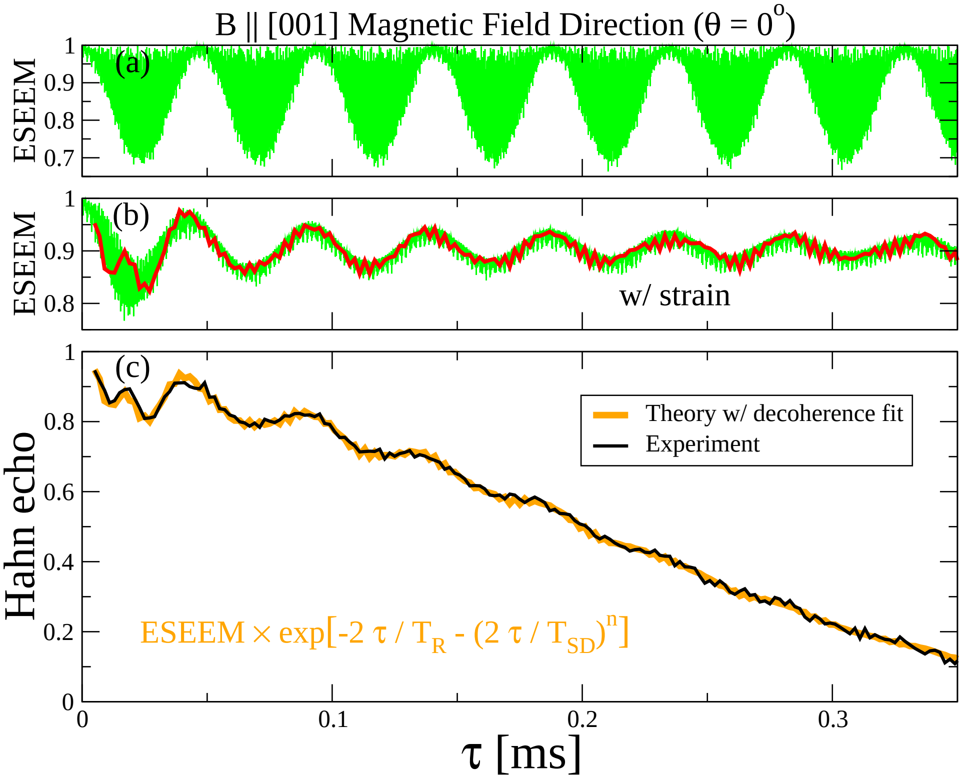

Figure 6.6: AHF-induced ESEEM in Si:P with an applied magnetic field in the [001] direction. (a) Pure AHF-induced ESEEM for a single electron spin. The green “blob” is one curve with high frequency components. (b) Before matching the ESEEM to experiment, we must account for strain effects in the ensemble of donor electrons (green); we must additionally sample at the same values of τ as the experiment (red) yielding a stroboscopic effect. (c) Comparison with experiment (black). In the theory, we combine the decoherence effects of ESEEM, SD, and longitudinal relaxation by simply multiplying them together. The orange curve gives ESEEM of our theory [red curve in (b)] multiplied by $\exp\left[-2\tau/T_R\right]\exp\left[-\left(2\tau/T_{SD}\right)^n\right]$ where T_R, T_{SD}, and n are fitting parameters for the relaxation time, SD time, and SD exponent respectively.

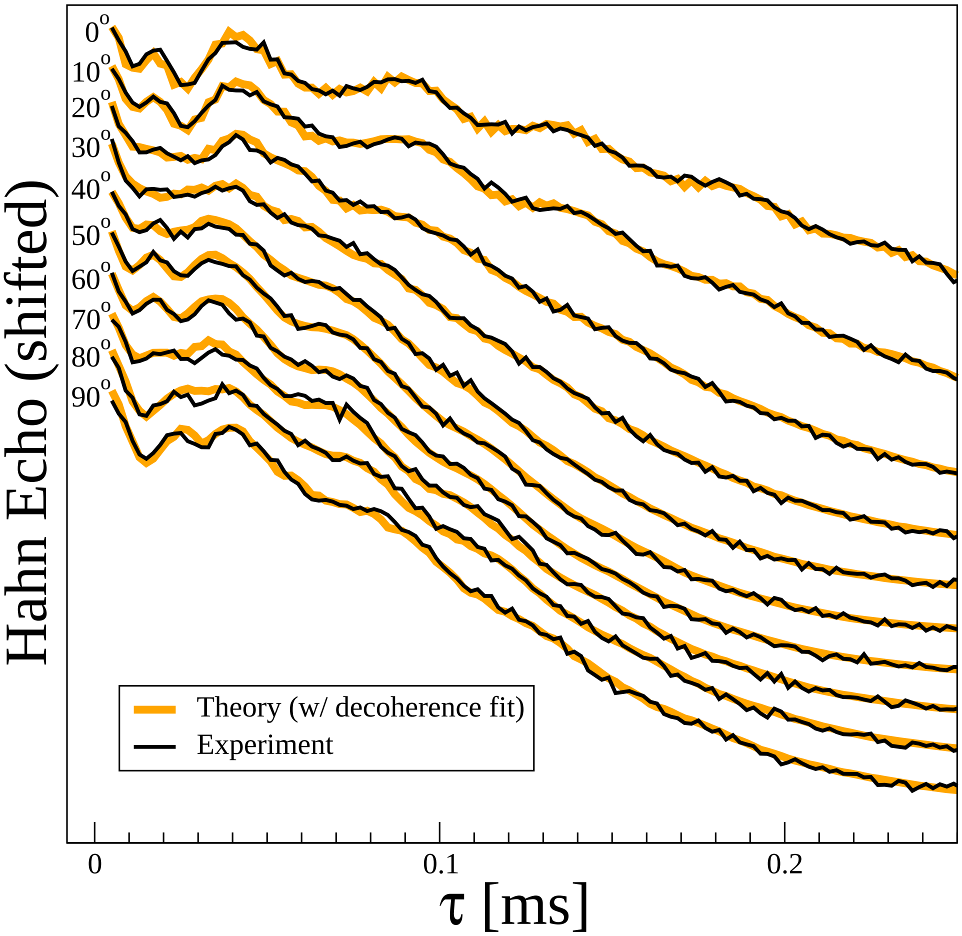

Figure 6.7: AHF-induced ESEEM in Si:P for ten different curves corresponding to ten different magnetic field angles ranging from the [001] to the [110] directions. The plots are shifted in order to distinguish each angle. All fits use the same normalization, strain distribution width (0.4%), and relaxation time ($T_R = 2.17 \pm 0.02$ ms) parameters. There are two fitting parameters per curve: the SD time, T_{SD}, and the SD exponent, n. These fitting parameters are compared with our SD theory [Sec. 6.1.1] in Fig. 6.8.

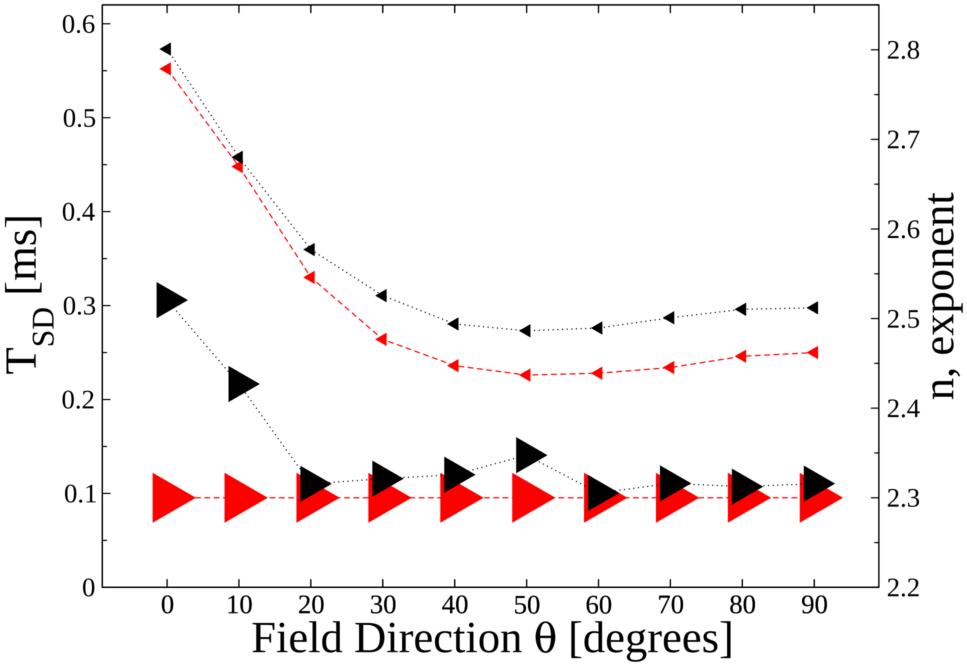

Figure 6.8: Comparison between the SD fitting parameters (black triangles connected with dotted lines) of Fig. 6.7 and the theoretical predictions (red triangles connected with dashed lines) of Sec. 6.1.1. Right [left] triangles correspond to n [T_{SD}]; sizes approximate fitting uncertainty. The experimental n fit deviates from theory (2.30 ± 0.05) only at small angles where nearest neighbor dipolar flip-flop interactions approach zero.

in Fig. 6.6(b) where, in order to fit the experimental results, we assume a Gaussian distribution for HF frequencies with a 0.4% width (similar results are obtained if the Zeeman frequencies are randomly distributed as well as or instead of the HF frequencies so this is just one fitting parameter for the strain distribution width). Also shown in Fig. 6.6(b) is the stroboscopic effect that emerges when we sample the same values of τ as those reported in the experiment. The theoretical (orange) curve in Fig. 6.6(c) shows the ESEEM result of Fig. 6.6(b) multiplied by $\exp\left[-2\tau/T_R\right]\exp\left[-\left(2\tau/T_{SD}\right)^n\right]$ to account for independent effects of longitudinal relaxation (due to interactions between electrons at different donors) and SD. This agrees well with the experimental results [black curve in Fig. 6.6(c)] after we normalize the signal strength as an additional fit (the experiment only gives the Hahn echo decay on a relative scale based upon the strength of the observed signal). Again, we use a total of five fitting parameters in Fig. 6.6; however, we use only two fitting parameters per curve in Fig. 6.7 and these two SD parameters are compared with our theoretical results in Fig. 6.8.

6.1.3.2 Suppressing anisotropic hyperfine modulations

In the "worst-case" scenario such that modulations from all nuclei combine constructively, the maximum possible modulation depth, averaged over isotopic configurations is given by

$$\max\left(1 - V(\tau)\right) = 1 - \prod_n \left[1 - 2 f k_n\right]. \tag{6.18}$$

We show this maximum modulation as a function of field strength due to various nuclear shells (symmetry-related sets of lattice sites [51]) in Fig. 6.9 (a).

One interesting feature of the maximum modulations shown in Fig. 6.9 (a) is that a peak occurs when $\omega_I \sim A_n/2$ (with A_n positive) for each shell of atoms. At each such cancellation condition, as it is dubbed, the Zeeman and HF energies of nucleus n cancel when the electron spin is up but not down, freeing the nuclear spin from conservation of energy constraints conditional upon the state of the electron spin. Mathematically, ω_{n+} is minimized [Eq. (6.17)] so that k_n is at (or very near) its maximum resulting in modulation depth peaks. Experimental results for two different magnetic field strengths near the A-shell cancellation condition peak are shown in Fig. 6.9 (c); these field strengths are labelled α and β in Fig. 6.9 (b). As expected, stronger modulations are observed for the field strength closer to the peak center. As it turns out, the experimental results shown in Secs. 6.1.1 and 6.1.3.1 used an applied field strength of 351.5 mT, labelled as χ in Fig. 6.9(b), near the center of the A-shell peak.

It is clear from Fig. 6.9 and the above discussion that to minimize decoherence by the AHF interaction, cancellation conditions for all the shells with finite AHF coupling constant should be carefully avoided by properly selecting the applied magnetic field strength (or, in electron spin resonance, the corresponding microwave cavity frequency). Furthermore, away from the cancellation condition peaks, the E-shell nuclei (nearest neighbors to the P nucleus) have the strongest AHF coupling by far, so that they dominate the echo modulations by more than an order of magnitude as seen in Fig. 6.9 (a). Remarkably, the echo modulation due

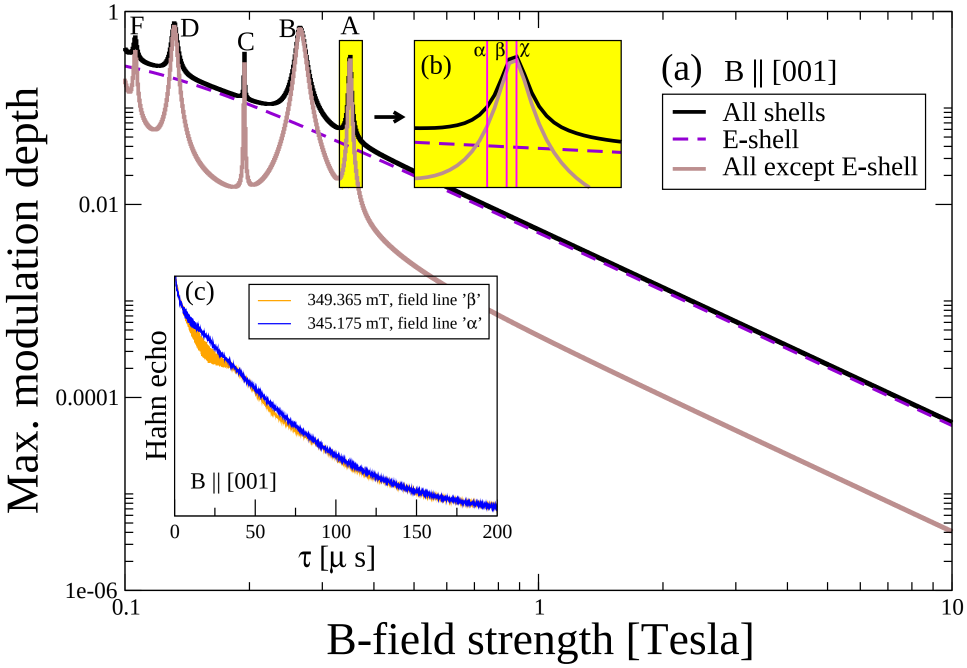

Figure 6.9: (a) Maximum modulation depth [Eq. (6.18)] in natural Si averaged over isotopic configurations with an applied magnetic field, B, parallel to the [001] lattice direction considering all shells (provided in Ref. [51]), just E-shell sites (nearest neighbors of the P donor), and all shells except the E-shell. Near the cancellation condition, $\omega_I \sim A_n/2$, for each shell of nuclei is a peak labelled by the shell letter. (b) Enlargement of the A-shell peak marking three field strengths, α, β, and χ, used in experiments for the data we present in Sec. 6.1; χ marks the field strength for the experimental data shown in Secs. 6.1.1 and 6.1.3.1. (c) Experimental [36] Hahn echo decay at field strengths α and β in the same Si:P sample. Relatively high doping, 10^{16} P/cm^3, results in fast exponential donor-donor induced relaxation but ESEEM is still observed.

to these dominating E-shell nuclei can be effectively removed at special magnetic field orientations [Fig. 6.10]. This is done be exploiting the periodic restoration of electron spin coherence in the presence of nuclei that are seen by the electron as magnetically equivalent. This restoration arises because $V_n(\tau) = 1$ [Eq. (6.16)] when τ is a multiple of $2\pi/\omega_{n\pm}$ (either + or −). Note that such periodic restoration does *not* generally occur in the free evolution case (see Eq.(7) of Ref. [71]). For special magnetic field orientations shown in Fig. 6.10, the contributing E-shell sites are magnetically equivalent with the same $\{\omega_{n-}, \omega_{n+}\}$; thus, the electron spin is periodically restored at the same values of τ regardless of isotopic (^{29}Si) configuration. In this way E-shell contributions can effectively be eliminated as exemplified in Fig. 6.11. By orienting the magnetic field in one of the special directions, the effects of all E-shell nuclei are simultaneously eliminated at periodic values of τ.

To understand the periodic restoration of ESEEM in the presence of magnetically equivalent nuclei, consider the Hahn evolution operators for an initially up/down electron spin, $\hat{U}^{\pm}_{\text{Hahn}} = \hat{U}^{\mp}_0(\tau)\hat{U}^{\pm}_0(\tau)$. The $\hat{U}^{\pm}_0(\tau)$ evolution operators simply precess the spins of the magnetically equivalent nuclei at angular frequencies of $\omega_{\pm}$ [Eq. (6.17)], and, thus, $U_{\pm}(2\pi m/\omega_{\pm}) = \hat{\mathbb{1}}$ for any integer m. Taking $\tau = 2\pi m/\omega_-$, for example, then $\hat{U}^{\pm}_{\text{Hahn}} = \hat{U}^{+}_0(\tau)$. Thus the evolution of the magnetically equivalent nuclei is independent of the electron spin so that the electron qubit is fully decoupled from these nuclei. If we concatenate (as in CDD) or repeat (as in PDD) the Hahn sequence, as discussed in Ch. 5, with $\tau = 2\pi m/\omega_-$, we generally find that $\hat{U}^{\pm} = \hat{U}^{+}(t/2)$ where t is the total pulse sequence time. These sequences thus preserve the property of decoupling the electron from magnetically equivalent nuclei

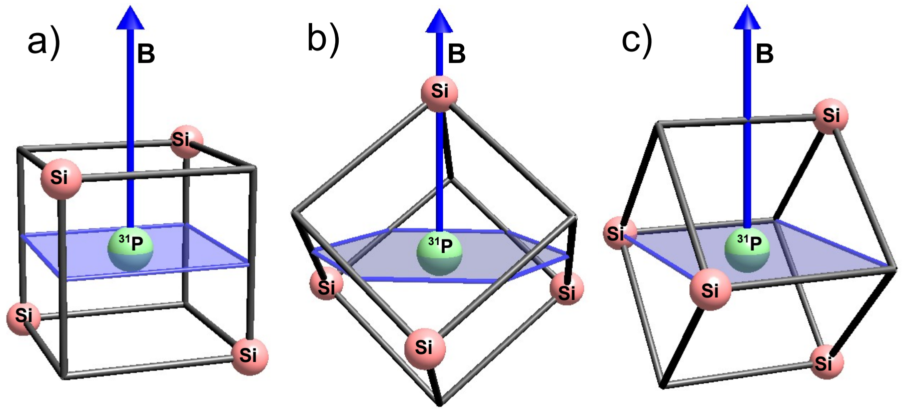

Figure 6.10: Special applied magnetic field directions that allow effective removal of echo modulation contributions due to E-shell nuclei (the four nearest neighbors to the P donor). The arrows and translucent sheets respectively indicate directions from the P atom parallel and perpendicular to the applied magnetic field. Sites in these direction give no anisotropic contribution ($B_n = 0$); in each of the three cases, the E-shell sites that *do* contribute are magnetically equivalent.

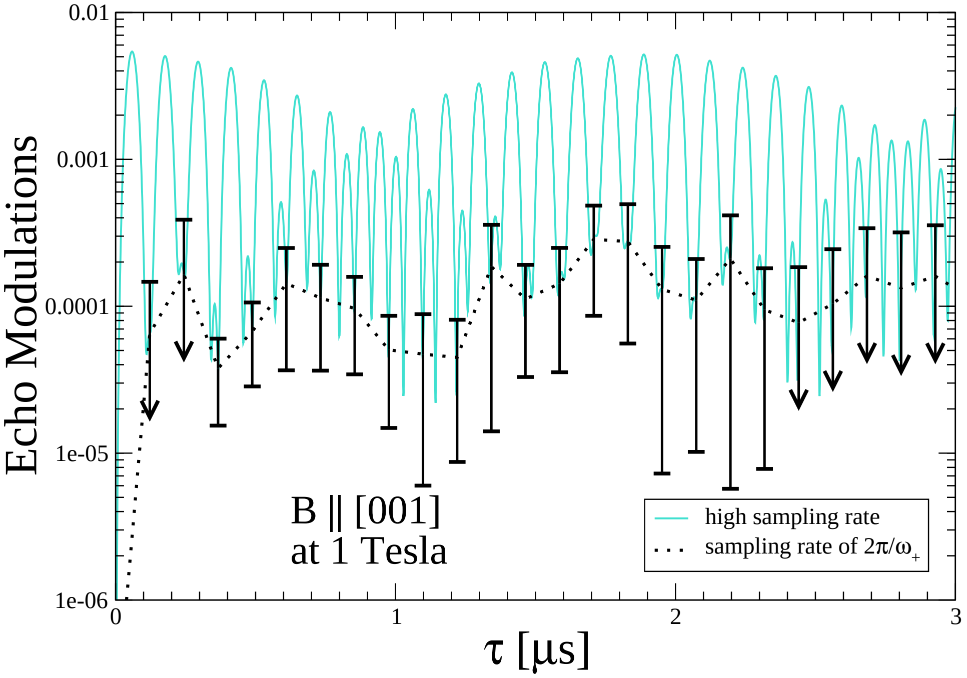

Figure 6.11: Echo modulations, $1 - V(\tau)$, in natural Si with an applied field of 1 T in the [001] direction corresponding to Fig. 6.10 (a). When sampling τ at multiples of $2\pi/\omega_+$ (or $2\pi/\omega_-$), the E-shell nuclei give no contribution to the echo modulations. Error bars, vertically asymmetric because of the log scale, correspond to the standard deviation resulting from random isotopic configurations; those with down arrows extend below the visible range.

when using the proper timing. In fact, this property is common to any balanced sequence in which an initially up or down electron (or the separate components of a superposition state) spends an equal amount of time being up and down.

We have studied Si:P donor electron spin decoherence due to AHF interaction which is an important dephasing mechanism in Si. We clarify the electron spin echo envelope modulation in the Si:P system and the resonance-like contributions from nuclear spins in various shells away from the P atoms, and our theory is in excellent quantitative agreement with experiment. Most importantly, we suggest an approach to minimize the decoherence effect of AHF interaction by avoiding the cancellation conditions and orienting an applied magnetic field along directions that can periodically eliminate the contributions from the dominant E-shell nuclei.

6.2 Gallium Arsenide Quantum Dots

Our next application is to study the decoherence of a localized quantum dot electron spin in GaAs. Such quantum dot qubits are exploited by the well-known quantum computing proposal of Loss and DiVencenzo [72] and many more recent variants [73, 74]. The decoherence of quantum dot spins has been much studied recently [41, 40, 47, 75, 76, 77].

For our analysis, we parameterize the quantum dot wave-function, $\Psi(\boldsymbol{R})$, by the quantum well thickness, z_0, and Fock-Darwin radius, $\ell(B)$ (a function of the magnetic field strength), as described in Ref. [35]. This will determine the HF coupling constants, A_n [Eq. (3.10)], responsible for the qubit-bath interaction, $\hat{\mathcal{H}}_{qb} = \sum_n A_n \hat{I}_{nz}/2$, due to the Fermi-contact HF interaction (Sec. 3.2.3). We have [35]

$$\begin{aligned} A_n &= \frac{16}{3}\frac{\gamma_S\gamma_I\hbar(a_{\mathrm{GaAs}}^3/4)}{\ell^2(B)z_0}d(I)\cos^2\left(\frac{\pi}{z_0}Z_n\right) \\ &\quad\times\exp\left(-\frac{X_n^2+Y_n^2}{\ell^2(B)}\right)\Theta(z_0/2-|Z_n|) \\ &\quad-\gamma_S\gamma_I\hbar\frac{1-3\cos^2\theta_n}{|\boldsymbol{R}_n|^3}\Theta[X_n^2+Y_n^2-\ell^2(B)], \end{aligned} \tag{6.19}$$

with $a_{\mathrm{GaAs}} = 5.65$ Å and $\gamma_S = 1.76 \times 10^7 (\mathrm{s\ G})^{-1}$ (the free electron gyromagnetic ratio). The GaAs lattice has a zinc-blende structure with two isotopes of

Ga atoms placed on one fcc lattice and ^{75}As atoms placed on the other fcc lattice [62]. The Ga isotopes are 60.4% ^{69}Ga and 30.2% ^{71}Ga [78]. We used $\gamma_I = 4.58, 8.16, 6.42 \times 10^3 (\text{s G})^{-1}$ and $d(I) = 9.8, 5.8, 5.8 \times 10^{25}$ cm^{-3} for ^{75}As, ^{71}Ga, and ^{69}Ga, respectively [79]. All of these nuclei have a valence spin magnitude of $I = 3/2$ which means that Eq. (6.5) is not quite applicable; this exact pair solution can be made valid for $I = 3/2$ by simply multiplying by a factor of 25 to account for all combinations of flip-flopping spin states.

As discussed in Sec. 3.2.4, HF-mediated interactions, effective coupling between nuclei that results from virtual electron spin transitions, are generally significant in GaAs even at modest magnetic fields because of their long-range nature. However, as was also noted in that section, the effect of this interaction largely cancels out (exactly cancels out in the pair approximation) when applying balanced pulse sequences (in which the electron spin spends an equal time being up or down) such as the Hahn echo or the dynamical decoupling sequences discussed in Ch. 5. There can be an additional visibility loss related to the HF-mediated interaction that is not cancelled out in these pulse sequence; however, for the quantum dots represented in Fig. 6.12, this visibility loss is estimated as $\sum_n (A_n/\Omega_n)^2 \lesssim 10^{-5}$ for an applied field strength of 1 T (the smaller dots exhibit greater visibility loss by this estimate due to their concentration of electron probabilities and correspondingly large values of A_n). It is important to note that FID, which should technically define the T_2 dephasing time, is dominated by this HF-mediated interaction [40].

Most of our results only include dipolar interactions (Sec. 3.5) for the intrabath Hamiltonian, $\hat{H}_{bb}$ and furthermore use the secular approximation for the strong applied magnetic field limit. However, indirect exchange interactions [55, 58, 59, 60, 61], discussed in Sec. 3.2.5, between nearest neighbors of GaAs may be of the same order of magnitude as the dipolar interactions and thus affect SD in this material [40]. At the end of Sec. 6.2.1, we include these interactions and compare our results to the pair approximation results of Ref. [40]. The results are not qualitatively changed by disregarding indirect exchange interactions, and the decay times are in quantitative agreement well within an order of magnitude.

Ignoring HF-mediated and indirect exchange, except as noted, the dominant part of the intra-bath Hamiltonian in the limit of a large magnetic field is the secular part of the dipolar interaction [Eqs. (3.5) and (3.7)]. One must take care not to include flip-flop terms between nuclei of different species [as prescribed in Eq. (3.6)] since the gyromagnetic ratios of ^{75}As, ^{71}Ga, and ^{69}Ga are significantly different. Furthermore, in order to account for the random allocation of the two Ga isotopes in the Ga sub-lattice, these isotopes are chosen randomly, with appropriate probabilities, while performing the statistical, Monte-Carlo, sampling of cluster contributions in calculating $\langle \Sigma_k(\tau) \rangle$.

6.2.1 Hahn echo spectral diffusion

The lowest order results, $v_E(\tau) \approx \exp\left[\langle \Sigma_2(\tau) \rangle\right]$, for most of our GaAs calculations show a Hahn echo decay of the form $\exp\left[-(2\tau/t_0)^4\right]$. This differs qualitatively from the decay for Si:P which, by our calculations, has the form $\exp\left[-(2\tau/t_0)^\alpha\right]$ where $\alpha \sim 2.3$ for a range of τ appropriate for natural Si and some range of isotopic purification. This $\exp\left[-(2\tau/t_0)^4\right]$ form of the GaAs echo decay corresponds to the lowest order of the τ-perturbation (Sec. 5.1.2); the reason that it has this form relates to our assumed shape for the electron wave-function and will be discussed in more detail in Sec. 6.2.2.

Figure 6.12 shows the t_0 of the initial $\exp\left[-(2\tau/t_0)^4\right]$ Hahn echo decay for various parameter settings of z_0 and ℓ with two different magnetic field orientations. Also shown is $t_{1/e}$, defined such that $v_E(\tau = t_{1/e}/2) = e^{-1}$. One can think of this $t_{1/e}$ as an effective T_2-time (with respect to the Hahn echo) for the problem although the echo decay is not a simple exponential. Except for small dots, $t_0 = t_{1/e}$, indicating that the decay has the form $\exp\left[-(\tau/\tau_0)^4\right]$. Small dots deviate from this form, beginning to have longer $t_{1/e}$ decay times than their initial characteristic times, t_0. It was noted in Ref. [35] that decoherence times become infinite as the size of the quantum dot approaches zero or infinity with a minimum decoherence time at some finite size. The former is simply because the electron has no interaction with nuclei as the quantum dot size approaches zero, and the latter is because the nuclei all have the same coupling to the electron as the size becomes infinite. For $z_0 = 5$ nm we begin to approach this maximum decoherence (minimum $t_{1/e}$) near $\ell = 10$ nm, but only in the regime where $t_{1/e}$ deviates from t_0.

As discussed previously, the flip-flop interactions between the different nuclear species is suppressed by their Zeeman energies. Because of this, the separate fcc lattices (one containing Ga and the other containing As) are decoupled in the pair approximation (2-clusters) that dominates the Hahn echo. In silicon, the asymmetry of the diamond lattice results in maximum decoherence in the [111] direction. In this

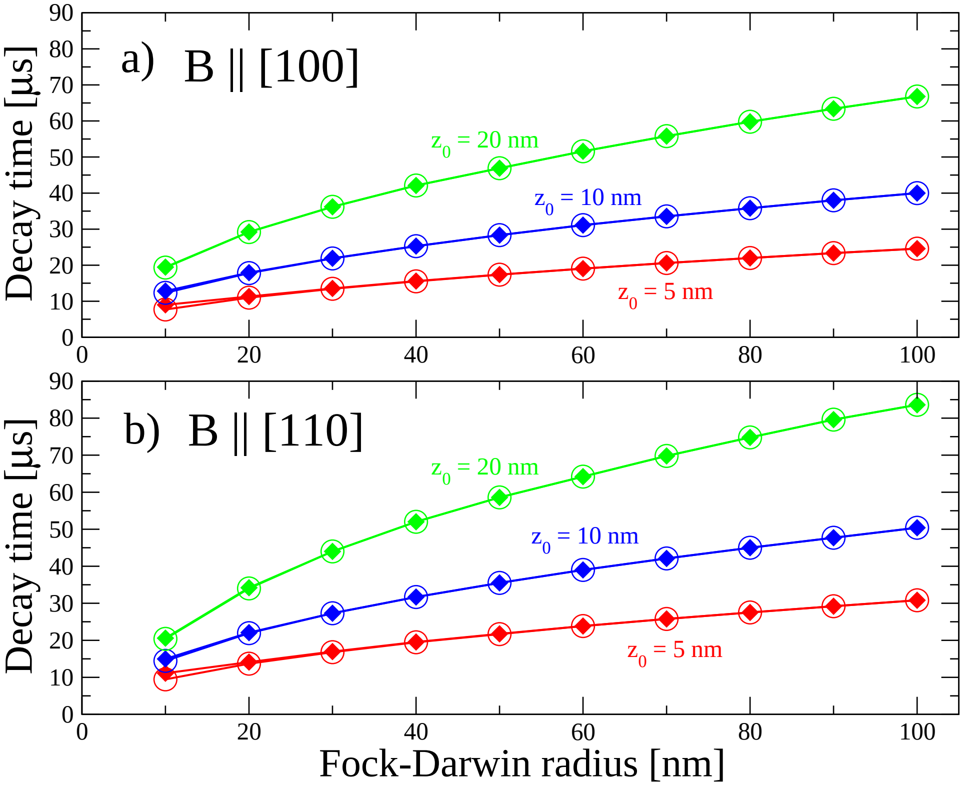

Figure 6.12: For GaAs quantum dots, t_0 (circles), the characteristic initial decay time, and $t_{1/e}$ (diamonds), the e^{-1} decay time, versus the Fock-Darwin radius ℓ for various quantum well thicknesses, $z_0 = 5, 10,$ and 20 nm. The orientation of the magnetic field is (a) along the z_0 confinement of the quantum dot and [100] lattice direction, or (b) perpendicular to the z_0 confinement direction and along [110] of the lattice.

case, because the fcc lattice is more symmetric, the angular dependence is primarily a result of the shape of the quantum dot (not the lattice). Figure 6.12 shows slight quantitative differences when the magnetic field is along the z_0 confinement direction or perpendicular to it.

We now return to a discussion of the indirect exchange interaction between nuclear spins (mediated by virtual inter-band electronic transitions) that were neglected in the above calculations. Including the exchange interaction, we should use

$$b_{nm} = b_{nm}^{\mathrm{D}} + b_{nm}^{\mathrm{Ex}}, \tag{6.20}$$

where b_{nm}^{D} is the dipolar coupling [Eq. (3.7)], and b_{nm}^{Ex} is the indirect exchange coupling [Eq. (3.15)]. We note that $b_{nm}^{\mathrm{Ex}} = 0$ in the Si:P system to a high degree of accuracy. Yao *et al.* [40] performed SD decoherence calculations (using an equation that is equivalent to our lowest order result) for GaAs quantum dots including the indirect exchange interaction. As a verification of the correctness of our calculations, Fig. 6.13 reproduces their Hahn echo results using our method but including the indirect exchange interactions. Figure 6.13 also shows the results for the same parameters when the indirect exchange is excluded; it is apparent that this coupling is quantitatively significant in GaAs quantum dots but not qualitatively significant (the decay exhibits the short τ behavior either way). The kink in the $t_{1/e}$ curve for the case of excluded indirect exchange is believed to be a discrete lattice effect only noticeable for small quantum dots. For such small quantum dots, it is likely that Eq. (6.19), derived from an approximate electron wave-function, is somewhat

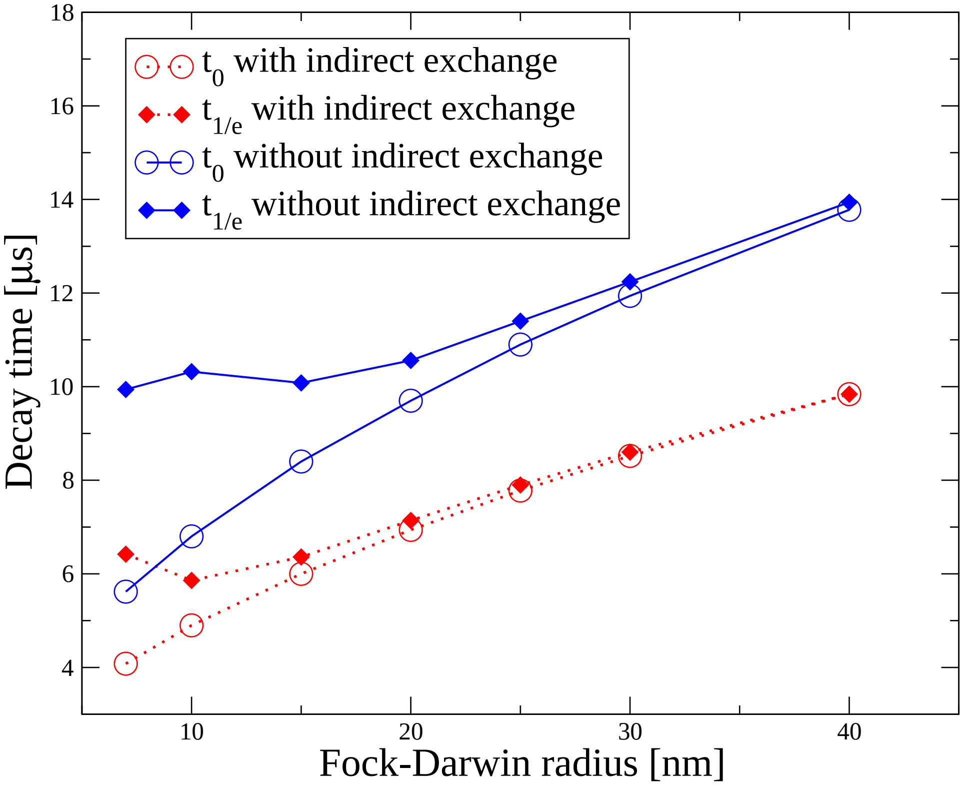

Figure 6.13: For GaAs quantum dots, t_0, the characteristic initial decay time, and $t_{1/e}$, the e^{-1} decay time, versus the Fock-Darwin radius ℓ for a quantum well thicknesses of $z_0 = 2.8$ nm. The orientation of the magnetic field is parallel to [110] of the lattice; this is perpendicular to the z_0 confinement of the quantum dot. This shows results both when including or excluding the indirect exchange coupling.

inaccurate.

6.2.2 Cluster expansion convergence

With our cluster expansion approach, we can estimate the error of our calculated decay curves by performing higher order calculations. We observe that the larger quantum dots have larger corrections. For quantum dots with $z_0 = 20$ nm and $\ell = 100$ nm our calculations indicate maximum correction to the Hahn echo decay curves on the order of 10^{-3}, 0.1% of the initial $v_E(0) = 1$, just as it was for natural Si (Fig. 6.5). For dots with $z_0 = 5$ nm and $\ell = 10$ nm, absolute corrections are on the order of 10^{-4}, 0.01% of the initial $v_E(0) = 1$. Fig. 6.14, analogous to Fig. 6.5, gives these low-order corrections explicitly for an intermediate size ($z_0 = 10 \text{ nm}, \ell = 50$ nm) GaAs quantum dot.

Because most of our GaAs results are in the form corresponding to the limit of small τ, it is tempting to think that GaAs is dominated by the $c_{nm} \sim (A_n - A_m)/b_{nm} \ll 1$ regime appropriate for the τ-expansion (Sec. 5.1.2). However, as with Si:P (Sec. 6.1.1), we find that the cluster expansion converges because it is dominated by clusters with $c_{nm} \gg 1$ for which the intra-bath perturbation is applicable. This is confirmed by comparing calculations that use exact pair contributions versus approximate pair contributions using the lowest order of the intra-bath perturbation (see Sec. 5.1.3). These different calculations agree very well for small quantum dots, but deviate slightly for larger quantum dots. Intermediate sized dots are well-approximated by either perturbation theory. The reason the results

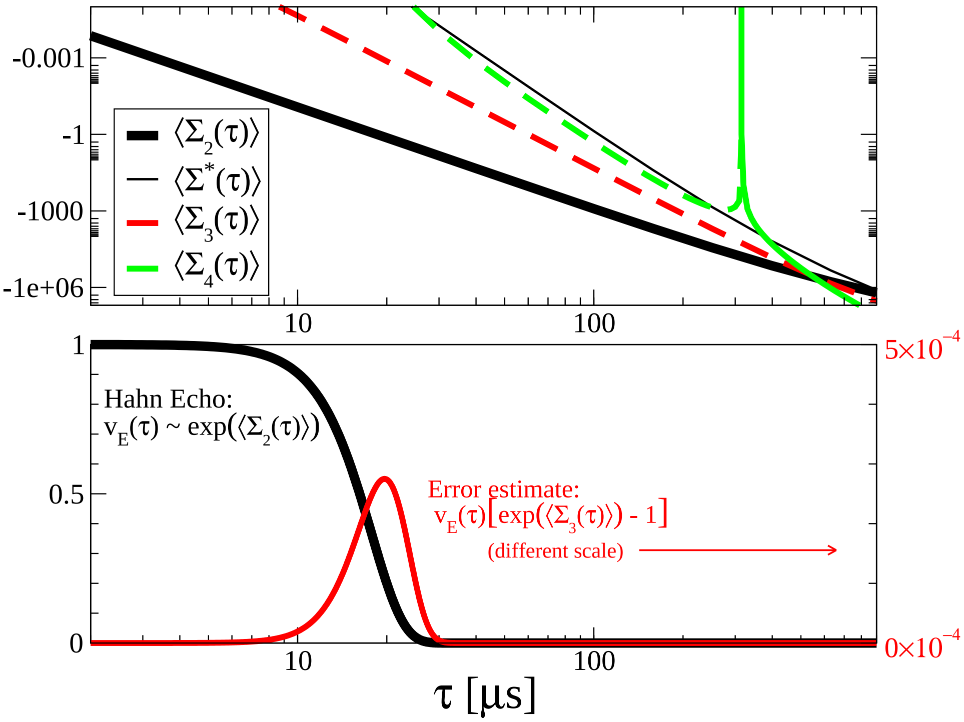

Figure 6.14: Successive contributions to the cluster expansion of the the Hahn echo, $v_E(\tau)$, computed for a GaAs quantum dot with $B \parallel [110]$, $z_0 = 10$ nm, and $\ell = 50$ nm. (top) Log-log plot of low-order contributions to the natural log of the Hahn echo, $\ln(v_E(\tau))$. Ordinate axis is negative; however, dashed lines indicate negated curves (and thus represent positive values). (bottom) Conservative estimate of the absolute error of the lowest order Hahn echo result (scale on the right) due to 3-cluster contributions, $\langle\Sigma_3(\tau)\rangle$. The lowest order Hahn echo result is shown as a reference (scale on the left). The logarithmic time scale is the same for all plots (top and bottom).

are well-approximated by the small τ limit is therefore not because $c_{nm} \ll 1$ for dominating clusters, but rather because the dominating clusters, with $c_{nm} \gg 1$, have similar maximal values of c_{nm} (largest c_{nm} implies fastest dynamics and most significance to the initial echo decay) and thus contribute similar frequencies. These dominating clusters are located where the electron's wave-function has the largest gradient (where $\|A_n - A_m\|$ between nearest neighbors is greatest). There are many such clusters with maximal c_{nm} in quantum dots with Gaussian-shaped electron wave-functions. In contrast, there are just a few such maximal c_{nm} clusters in Si:P which has an exponential-type donor electron wave-function; these must be near the P donor and give negligible contribution to SD. This is the reason that our GaAs results exhibit short τ behavior but our Si:P results do not.

6.2.3 Experiments in GaAs

Remarkable experiments have recently [38] investigated the coherence properties of a *single* qubit in GaAs quantum dots. In the context of these experiments, the qubit was not the spin of a single electron, but rather a sub-space of two electron spins, each in separate quantum dots with a controllable exchange interaction between the two dots. The qubit states are represented by the two-electron spin states with zero total spin, $|\uparrow\rangle_1 \otimes |\downarrow\rangle_2$ and $|\downarrow\rangle_1 \otimes |\uparrow\rangle_2$ where the 1 and 2 subscripts label the dots (and contained electrons). An applied magnetic field protects each electron spin from depolarization; at the same time, the degeneracy of the zero-spin subspace is protected from uniform magnetic-field fluctuations [74]. Electrostatic potentials are used to manipulate the electrons. State preparation and final readout are performed by biasing the two electrons, with an applied voltage, into the same dot so that the singlet state, $\left(|\uparrow\rangle_1 \otimes |\downarrow\rangle_2 + |\downarrow\rangle_1 \otimes |\uparrow\rangle_2\right)/\sqrt{2}$, has the lowest energy because of the Pauli-exchange interaction [74, 80]. Voltage control is also used to turn on an exchange interaction by allowing the wave-function of the two electrons on different dots to overlap; such control can be used to rotate the qubit [74, 80]. Using this control, one can apply π-pulses in order to perform a Hahn echo sequence or any other DD sequence (such as those discussed in Sec. 6.3) to prolong the coherence of the qubit.

We can simply map this two-electron qubit into our single-spin qubit formalism. For convenience, we will define $|0\rangle = |\uparrow\rangle_1 \otimes |\downarrow\rangle_2$ and $|1\rangle = |\downarrow\rangle_1 \otimes |\uparrow\rangle_2$ as our two qubit basis states. Turning on the exchange interaction will split the energies of the $(|0\rangle + |1|)/\sqrt{2}$ and $(|0\rangle - |1|)/\sqrt{2}$ superposition states and thereby rotate the qubit in a "transverse" direction as required for a DD sequence that combats dephasing. In order to obtain the free evolution Hamiltonian needed by our formalism, we simply need to derive the qubit-bath Hamiltonian, $\mathcal{H}_{qb}$, from the HF interactions in each of the two dots, $\hat{\mathcal{H}}_1^{\mathrm{HF}} + \hat{\mathcal{H}}_2^{\mathrm{HF}}$, by taking its matrix elements in terms of our qubit basis states. With a strong applied magnetic field, and assuming we can neglect HF-mediated interactions as we did in the single dot case,

$$\hat{\mathcal{H}}_1^{\mathrm{HF}} + \hat{\mathcal{H}}_2^{\mathrm{HF}} = \sum_n A_n^{(1)} \hat{S}_{1z} \hat{I}_{nz} + \sum_n A_n^{(2)} \hat{S}_{2z} \hat{I}_{nz}, \tag{6.21}$$

so that $\langle 0|\hat{\mathcal{H}}_1^{\mathrm{HF}} + \hat{\mathcal{H}}_2^{\mathrm{HF}}|1\rangle = \langle 1|\hat{\mathcal{H}}_1^{\mathrm{HF}} + \hat{\mathcal{H}}_2^{\mathrm{HF}}|0\rangle = 0$; we thus have only the following dephasing qubit-bath interaction:

$$\mathcal{H}_{qb} = \langle 0|\hat{\mathcal{H}}_1^{\mathrm{HF}} + \hat{\mathcal{H}}_2^{\mathrm{HF}}|0\rangle = -\langle 1|\hat{\mathcal{H}}_1^{\mathrm{HF}} + \hat{\mathcal{H}}_2^{\mathrm{HF}}|1\rangle = \frac{1}{2}\sum_n (A_n^{(1)} - A_n^{(2)}). \tag{6.22}$$

During the free evolution part of the pulse sequence, the two electrons must have essentially no overlap in their wave-functions; therefore, $A_n^{(1,2)}$ will only be non-zero when n represents a nucleus in dot $1, 2$ respectively. Thus,

$$\mathcal{H}_{qb} = \frac{1}{2}\sum_{n \in \text{dot } 1} A_n^{(1)} - \frac{1}{2}\sum_{n \in \text{dot } 2} A_n^{(2)}. \tag{6.23}$$

Assuming that the intra-nuclear interactions occur only within the same bath (and that the bath is initially uncorrelated), then the problem fully decouples into spectral diffusion problems for dot 1 and dot 2 separately [81]. In terms of our cluster expansion (Sec. 4), we simply need to sum the cluster contributions in the two dots separately. In a random, unpolarized bath with two equivalent dots, the cluster contributions in each dot will be identical; then, because the logarithm of the echo is approximated as the sum of cluster contributions [Eq. 4.17], the resulting echo, v_E, is simply the squared value of the echo for the problem of a single-electron in just one of the dots. There should, thus, be no qualitative difference between the spectral diffusion of a single-spin qubit and this double-spin qubit; a prediction of $v_E \sim \exp[-(\tau/\tau_0)^4]$ for a single-spin qubit will carry over to the double-spin qubit.

Although the reported Hahn echo decay time, T_2, of Ref. [38] is compatible with our theory (which disregards other decoherence mechanism) as a limiting case, it is clear that the experimental echo decay does not match the $\exp[-(\tau/\tau_0)^4]$ form. Therefore, at least one of the assumptions of our theoretical model is not applicable to this experiment; for example, it may not be appropriate to treat the applied π-rotation pulses as ideal [77]. Also, the experimentalists are apparently *not* operating in the strong applied magnetic field limit (which we assume) because they find that the T_2 time increases with an increase magnetic field [38]. Preliminary calculations in which we treat the full dipolar coupling (not using the secular approximation of the strong applied field limit) in our cluster expansion formalism do not show any change in qualitative behavior that would account for this discrepancy. More work needs to be done in order to bring the theory and experiment of quantum dot dephasing decoherence into agreement.

6.3 Periodic and concatenated dynamical decoupling

In the literature, the performance of various dynamical decoupling schemes for quantum computation is either estimated with abstract formalism [14, 15, 18] or small toy models [18, 47]. In Ref. [42], however, we studied periodic CPMG pulse sequences in realistic mesoscopic solid state systems using our cluster expansion technique. Using the pair approximation, equivalent to the lowest order of our cluster expansion, concatenated sequences were studied as well in mesoscopic solid state systems in Refs. [43, 44]. As we have noted, however, the lowest order cancellations made in concatenation require the inclusion of clusters of increasing size in the cluster expansion; these larger clusters often dominate decoherence and therefore the pair approximation is not valid for analyzing concatenation sequences [49].

We make a comparison between our computed results, shown in Fig. 6.15, for

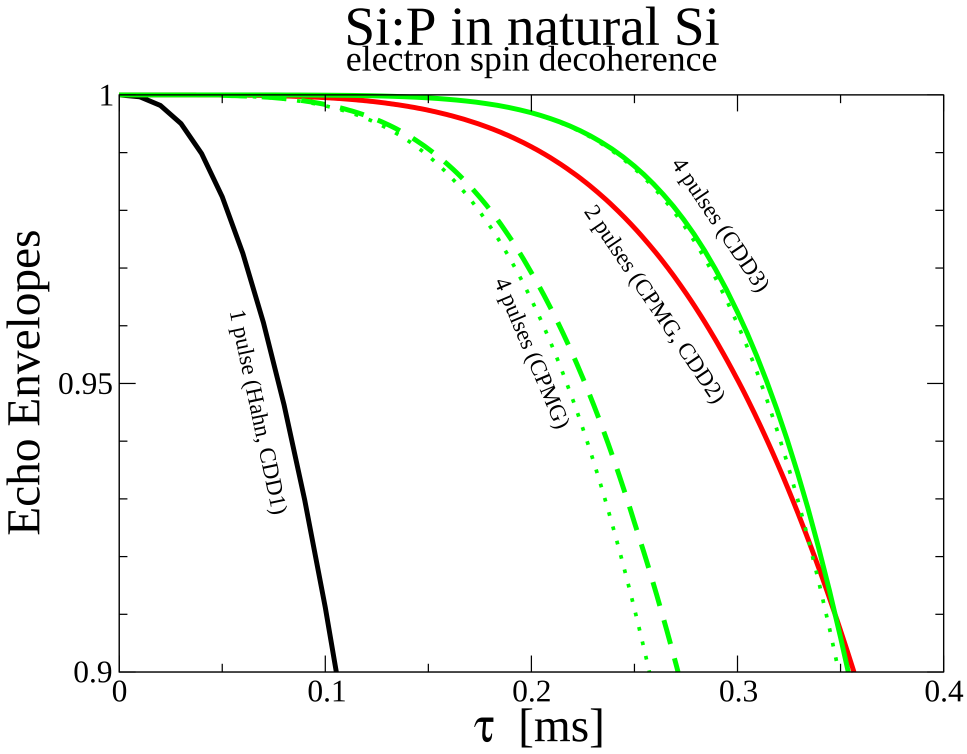

Figure 6.15: Echo decay of an electron bound to a P donor in natural Si with an applied magnetic field along the [100] lattice direction for different types of dynamical decoupling pulse sequence as a function of the time τ between pulses. Each concatenation level (CDD1, CDD2, and CDD3) improves the coherence of the qubit as a function of τ, at least for small τ. For comparison, the even-pulsed CPMG series (CDD2 being among them) yields progressively worse coherence as a function of τ (but better as a function of the overall sequence time). The dotted lines give corresponding results to the lowest order in the intra-bath perturbation.

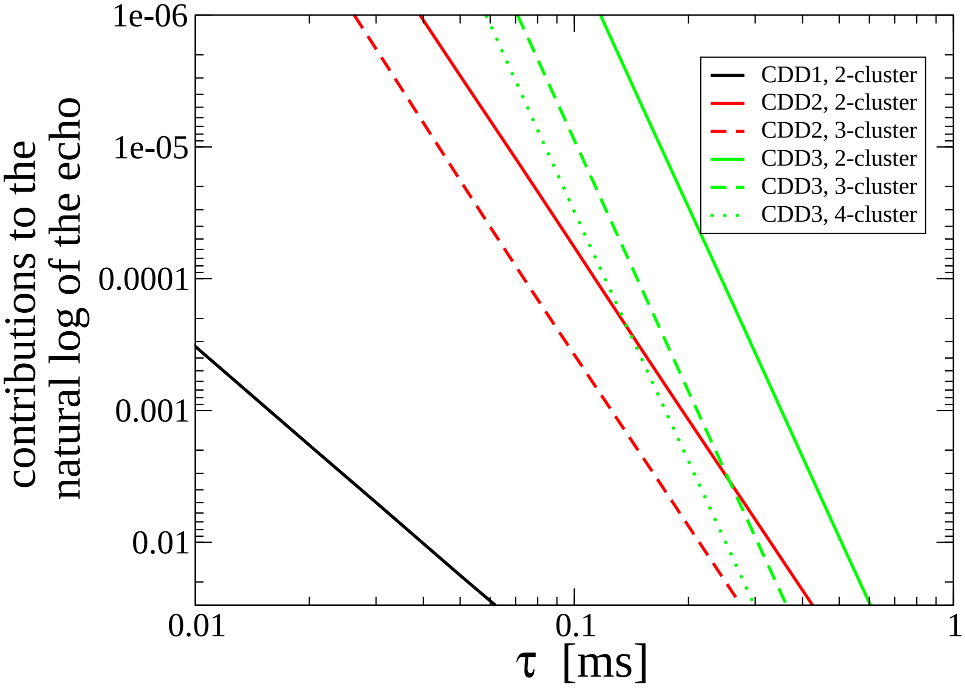

Figure 6.16: Contributions from different sized clusters for the concatenated echo decays in the Si:P system of fig. 6.15. The minimum required cluster size required to yield the appropriate lowest order result in the cluster expansion increases with each concatenation, and the larger clusters tend to dominate the decoherence.

the CDD and CPMG pulse sequence echoes of an electron bound to a P donor in natural Si. These are plotted as a function of the time τ between pulses. For the CPMG pulse sequence with 2ν pulses, the total sequence time is $t = 4\nu\tau$. With an increasing number of CPMG pulses, the coherence as a function of τ is diminished, but, as noted in Ref. [42], the coherence as a function of t tends to improved. For the CDD pulse sequence with l levels of concatenation, the total sequence time is $t = 2^{l+1}\tau$. With each level of concatenation, coherence as a function of either τ or t tends to improve. Figure 6.15 shows only the first 90% of the decay as a way to avoid sections of these curves that do not converge in the cluster expansion. Dotted lines in this figure show the results when using the lowest order of the intra-bath perturbation for cluster contributions. The deviation of these perturbative results from the convergent cluster expansion results correlates with the onset of the divergence in the cluster expansion as expected assuming that the intra-bath perturbation provides the reason for the cluster expansion convergence.

Contributions from different cluster sizes are shown for the CDD series in Fig. 6.16. We must increase the size of clusters that we include for each level of concatenation. The larger clusters of these concatenated pulses are seen to dominate the decoherence (concatenation of level l is dominated by cluster of size $l + 1$), invalidating the pair approximation used in Refs. [43, 44].

A comparison between different pulse sequences is shown in Fig. 6.17 for a quantum dot electron in GaAs. Again, the CPMG series decreases in performance as a function of τ (but not t) but the CDD series shows successive improvements, at short times, as a function of either τ or t. Contributions from different cluster

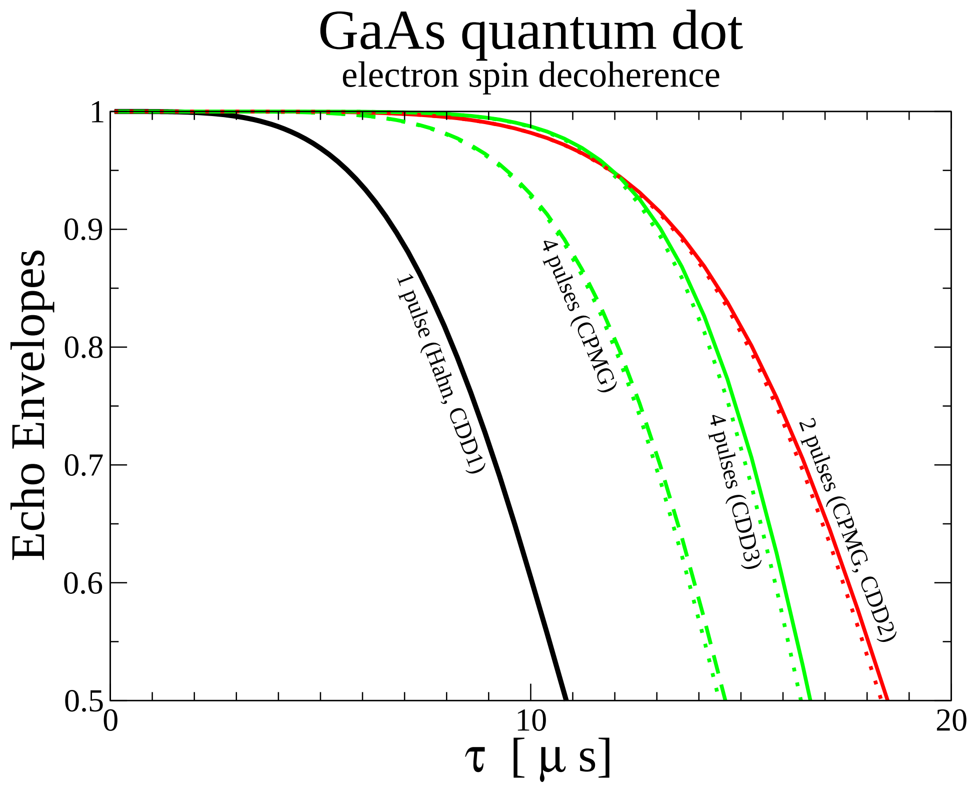

Figure 6.17: Echo decay of a quantum dot electron in GaAs with an applied magnetic field along the [110] lattice direction for different types of dynamical decoupling pulse sequence as a function of the time τ between pulses. Each concatenation level (CDD1, CDD2, and CDD3) improves the coherence of the qubit as a function of τ, at least for small τ. For comparison, the even-pulsed CPMG series (CDD2 being among them) yields progressively worse coherence as a function of τ (but better as a function of the overall sequence time). The dotted lines give corresponding results to the lowest order in the intra-bath perturbation. The quantum dot in this example has a Fock-Darwin radius of $\ell = 25$ nm and quantum well thickness of $z_0 = 8.5$ nm.

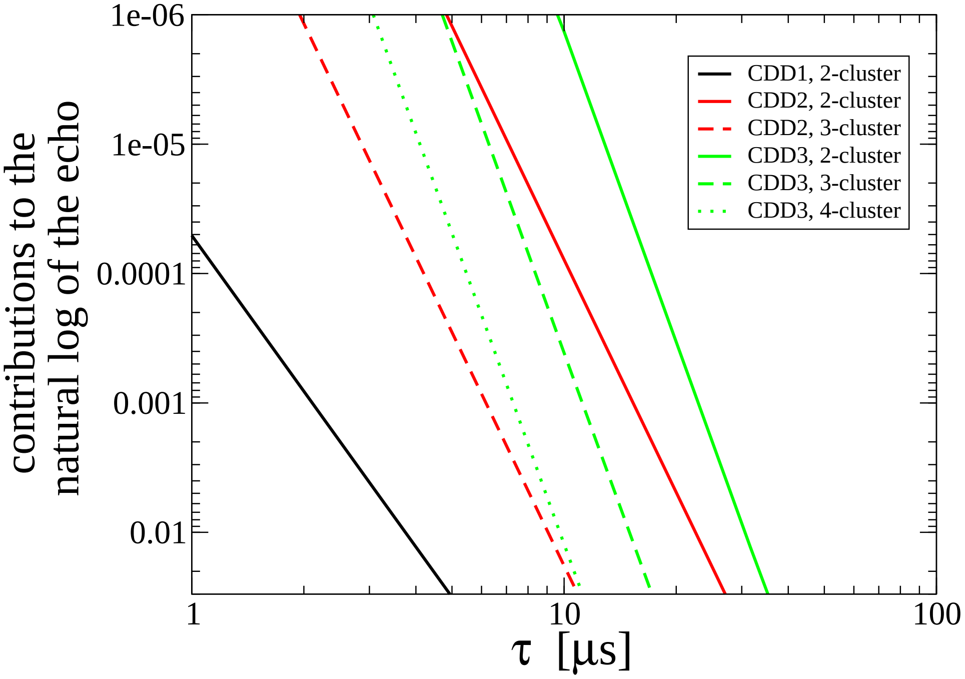

Figure 6.18: Contributions from different sized clusters for the concatenated echo decays in the Si:P system of fig. 6.17. The minimum required cluster size required to yield the appropriate lowest order result in the cluster expansion increases with each concatenation, and the larger clusters tend to dominate the decoherence.

sizes are shown for the CDD series in Fig. 6.18. Again we see that a concatenation of level l is dominated by clusters of size $l + 1$.

We did not include HF-mediated interactions in any of these results (Sec. 3.2.4). This is justified in the case of the Hahn echo where the effect of HF-mediated interactions are fully reversed (apart from a small visibility loss) in the pair approximation. However, using CDD sequences, where higher order cluster contributions must be taken into account, there may be significantly contributing processes that involve a combination of HF-mediated and dipolar (or other local) intra-bath interactions. This should be considered in future work.

6.4 Nuclear Spin Memory

The motivation for developing a solid state quantum computer architecture using localized spins as qubits arises primarily from the presumably long quantum coherence times for spins even in the strongly interacting solid state environment. In this respect, nuclear spins are ideal since both spin relaxation (i.e. T_1) and spin coherence (i.e. T_2) times are very long for nuclear spins, as compared with electron spins, due to their weak coupling to the environment. The application of a strong magnetic field further enhances nuclear coherence by suppressing, at least, the leading order relaxation and decoherence processes caused by direct HF coupling between nuclear spins and any surrounding electron spins due to the large mismatch between electron and nuclear spin Zeeman energies. In this section we again assume the limit of a strong applied magnetic field. We also neglect, somewhat uncritically, all effects of any direct HF coupling between electron spins and nuclear spins assuming our system to be entirely a nuclear spin system. The existence of localized electron spins in the environment will further suppress the nuclear spin coherence, and therefore, our theoretical values for nuclear spin quantum memory lifetimes should be taken as upper bounds.

Nuclear storage of quantum information in a solid state environment is most naturally placed on donor nuclei that are easily distinguishable from the surrounding intrinsic nuclei. We note that it is imperative that the memory is stored in a nucleus which is distinct from the surrounding nuclei in some manner so that the stored information can be recovered. Several quantum computing architecture proposals [26, 27] exploit the long-term quantum information storage capabilities which donor nuclei spins can possess. In this section, we present theoretical calculations of the T_2 dephasing of donor nuclear spins in two solid-state environments of interest for quantum computing: Si:P and GaAs:P. Specifically, we present coherence versus time information in the context of single-pulsed Hahn and periodic Carr-Purcell-Meiboom-Gill (CPMG) pulse sequence.

We again apply the cluster expansion technique of Ch. 4. In the localized electron qubit problems of the previous sections, the strong HF qubit-bath coupling relative to the dipolar (or other) intra-bath coupling aided the convergence of the cluster expansion due to the applicability of the intra-bath perturbation. For the case of the donor nucleus qubit, the qubit-bath coupling is due to intra-nuclear dipolar coupling with the same order of magnitude as the intra-bath coupling. For this reason, we will only be able to obtain convergent cluster expansion results for the initial part of the decay. We therefore focus on the initial decay and our plots show memory-loss as a function of time rather than exhibiting full, formally exact, decay curves.

We again use the secular part of the dipolar interaction for the intra-bath Hamiltonian (ignoring, as we stated earlier, interactions with any electrons in the system) [Eqs. (3.5) and (3.6)]. The qubit-bath interactions are also due to dipolar coupling. However, in this instance we disregard the flip-flop interactions which are suppressed via energy conservation as a result of the applied magnetic field and differing gyromagnetic ratios between the qubit and spins in the bath. Instead, we consider just the $I_{nz}I_{mz}$ term which will contribute to dephasing:

$$\begin{aligned} \hat{\mathcal{H}}_{qb} &\approx \sum_n A_n \hat{I}_{nz} \hat{S}_z && (6.24) \\ A_n &= \gamma_{\mathrm{D}} \gamma_n \hbar \frac{1 - 3\cos^2\theta_n}{R_n^3}, && (6.25) \end{aligned}$$

where $\hat{S}_z$ is a nuclear spin operator for the P donor nucleus, γ_{D} is the gyromagnetic ratio of the donor nucleus, R_n is the distance of nucleus n for the P donor, and θ_n is the angle of the vector from the P donor to nucleus n relative to the applied magnetic field.

We have performed cluster expansion calculations to successively approximate echoes for two different systems. In both systems, we have a P donor atom with $\gamma_{\mathrm{D}} = \gamma_{\mathrm{P}} = 1.08 \times 10^4 (\mathrm{s\ G})^{-1}$, and we have chosen the applied magnetic field to point along one of the conventional axes directions (e.g., $B||[001]$). In our figures, we plot "memory loss" versus total echo time (2τ) where we define memory loss as one minus the echo envelope, $1 - v_E(\tau)$, and we only show results where the cluster expansion is rapidly convergent.

We show Hahn and CPMG echo results for GaAs:P in Fig. 6.19; in this system, $\gamma_n = 4.58, 8.16, 6.42\times 10^3 (\text{s G})^{-1}$ for ^{75}As, ^{71}Ga, and ^{69}Ga, respectively, and all differ from γ_{P}. In the lowest order τ approximation of the GaAs:P Hahn echo,

$$\begin{aligned} \ln\left(v_{\text{Hahn}}(\tau)\right) &\approx -\left(\frac{\tau}{260\ \mu\text{s}}\right)^4 && (6.26) \\ &\approx -\left(t/520\ \mu\text{s}\right)^4. && (6.27) \end{aligned}$$

In Ref. [42] we showed that the log of the CPMG echo with a even number of pulses as a function of inter-pulse time scales as the number of pulses squared. With ν equal to half the number of applied pulses, then, the lowest order τ approximation of the GaAs:P CPMG echo is

$$\begin{aligned} \ln\left(v_{\text{CPMG}}(\tau)\right) &\approx -\nu^2\left(\frac{\tau}{195\ \mu\text{s}}\right)^6 \\ &= -\nu^{-4}\left(\frac{t}{780\ \mu\text{s}}\right)^6. && (6.28) \end{aligned}$$

The corresponding exact (convergent) results plotted in Fig. 6.19 do not visibly differ from Eq. 6.26 or Eq. (6.28) respectively; therefore, this approximation is valid in the region in which the cluster expansion converges. This short time approximation equation may serve as a useful educated guess (estimate) at times beyond cluster expansion convergence. If we do extrapolate Eq. (6.28) equations and define T_2 as the time in which the extrapolated echo reaches $1/e$, then we have $T_2 = \nu^{0.67} \times 780\ \mu\text{s}$ for even CPMG echoes. This gives a factor of 6.5 increase of nuclear spin coherence times relative to the electron spin quantum dot coherence times reported in Ref. [42] and Sec. 6.3. The behavior beyond the point of convergence may be

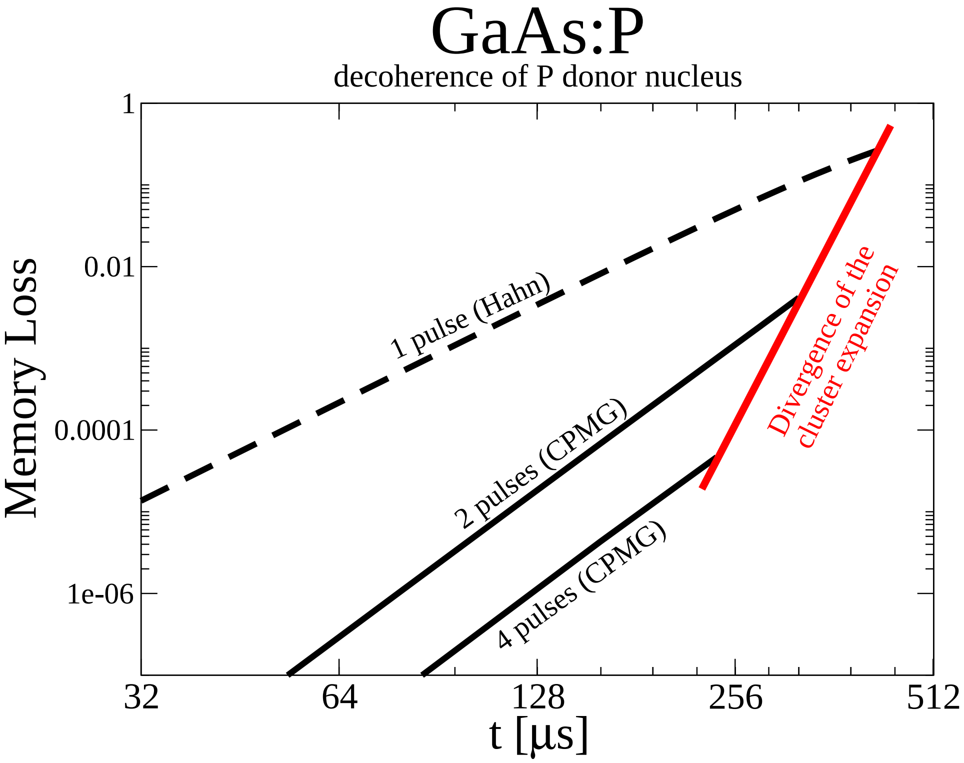

Figure 6.19: Numerical results of nuclear spin quantum memory loss for a ^{31}P donor nucleus that replaces an As atom in bulk GaAs. We define memory loss as one minus the normalized echo and plot this in a log-log scale as a function of the total echo time. The dashed line gives the Hahn echo results and the solid lines give CPMG echo results for two and four pulses. At some point for each type of echo sequence, the cluster expansion fails to converge.

an interesting theoretical question in itself. Are the curves well-behaved? Do they oscillate? Is it feasibly possible to obtain theoretical results in a regime in which cluster contributions *increase* with cluster size? These interesting and important questions are unfortunately beyond the scope of this work.

We additionally show Hahn and CPMG echo results for Si:P in Figs. 6.20 and 6.21; $\gamma_n = 5.31 \times 10^3 (\mathrm{s~G})^{-1}$ for ^{29}Si which also differs from γ_{P}. Unlike GaAs, Si has stable isotopes (^{28}Si, ^{30}Si) with zero spin. Among its stable isotopes, only ^{29}Si, which has a natural abundance of 4.67% and a spin of 1/2, has a non-zero spin. Isotopic purification can reduce the amount of ^{29}Si and thereby diminish SD caused by the nuclear spin bath. For generality, we define f to be the fraction of Si that is the ^{29}Si isotope. Figure 6.20 shows results in a natural Si bath ($f = 0.0467$), while Fig. 6.21 shows, for comparison, results in a bath of Si isotopically purified to $f = 0.01$.

The lowest order τ approximation of the Si:P Hahn echo yields

$$\begin{aligned} \ln\left(v_{\text{Hahn}}(\tau)\right) &\approx -f^2 \left(\frac{\tau}{1.05~\mathrm{ms}}\right)^4 && (6.29) \\ &\approx -f^2 \left(t/2.1~\mathrm{ms}\right)^4 . && (6.30) \end{aligned}$$

The f^2 dependence simply arises from the fact that, in this approximation, all contributions are from pairs of nuclei. With ν equal to half the number of applied pulses and again using the result of Ref. [42] for the scaling of even CPMG echoes with the number of applied pulses, the lowest order approximation to the Si:P CPMG

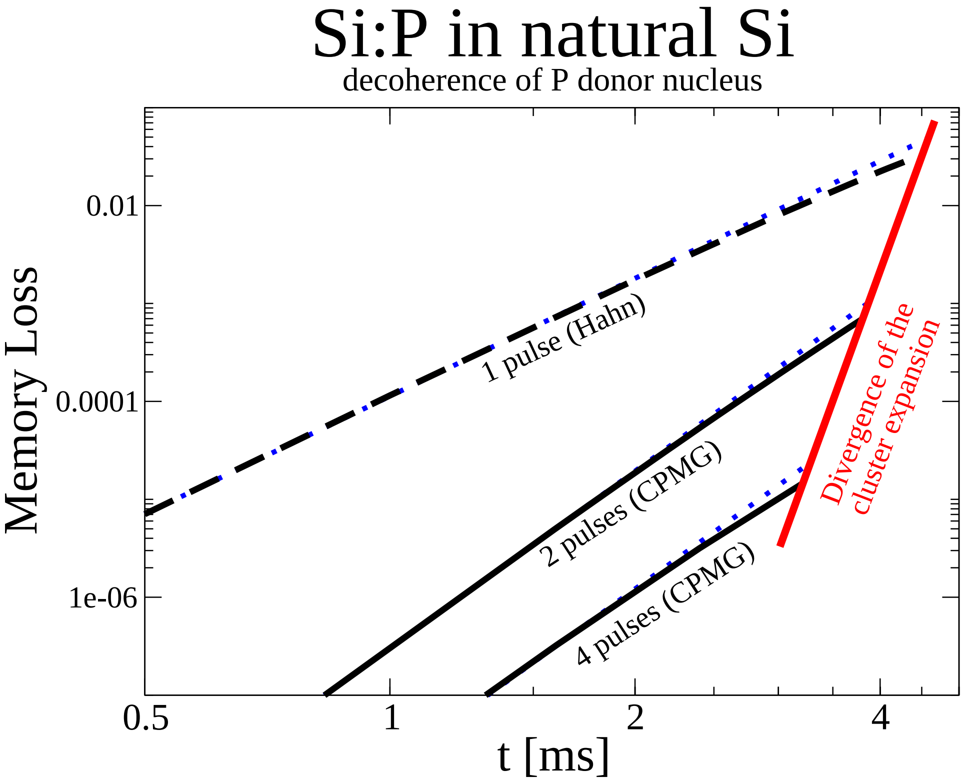

Figure 6.20: Numerical results of nuclear spin quantum memory loss for a ^{31}P donor nucleus in bulk Si. We define memory loss as one minus the normalized echo and plot this in a log-log scale as a function of the total echo time. The dashed line gives the Hahn echo results and the solid lines give CPMG echo results for two and four pulses. Dotted lines give corresponding results, for comparison, obtained from the lowest order expansions provided by Eqs. (6.29) and (6.31). At some point for each type of echo sequence, the cluster expansion fails to converge.

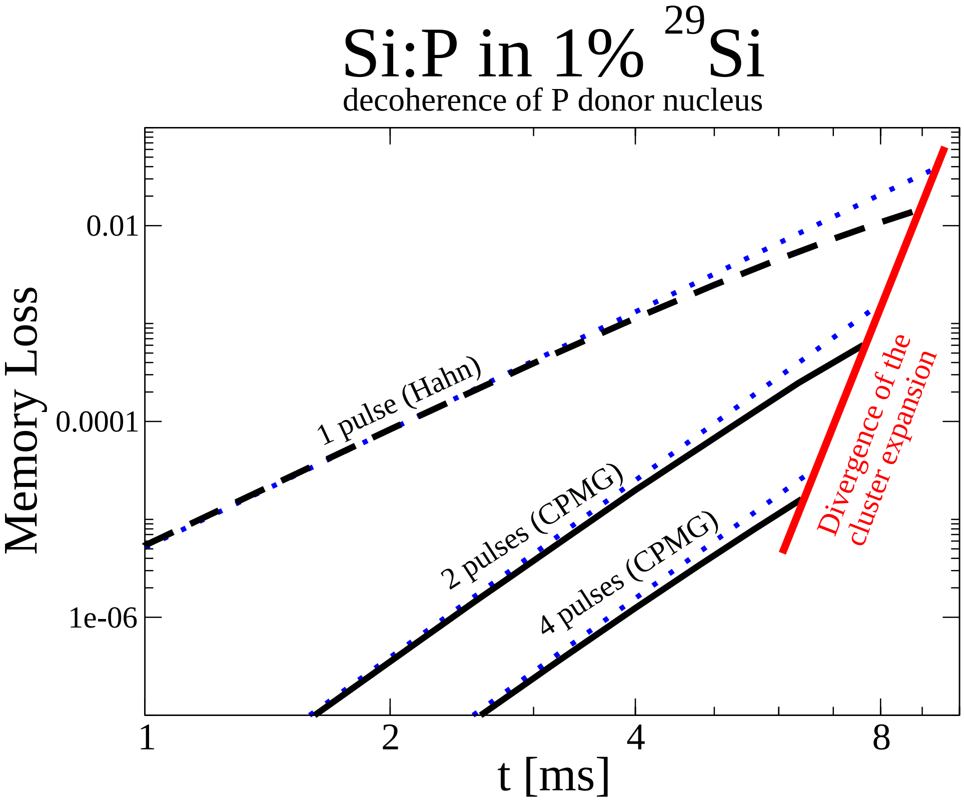

Figure 6.21: Equivalent to Fig. 6.20 except that results are shown for Si purified to 1% ^{29}Si. Lowest order result given by Eqs. (6.29) and (6.31) are shown by the dotted lines. Isotopic purification enhances coherence as predicted in these equations.

echo yields

$$
\begin{aligned}
\ln\left(v_{\mathrm{CPMG}}(\tau)\right) &\approx -\nu^2 f^2 \left[\left(\frac{\tau}{1.35\text{ ms}}\right)^6 + f\left(\frac{\tau}{0.70\text{ ms}}\right)^6\right] \\
&= -\nu^{-4} f^2 \left(\frac{t}{5.4\text{ ms}}\right)^6 \\
&\quad -\nu^{-4} f^3 \left(\frac{t}{2.8\text{ ms}}\right)^6 . \qquad (6.31)
\end{aligned}
$$

Dotted lines in Figs. 6.20 and 6.21 show the lowest order τ approximation [Eqs. (6.29) and (6.31)] for the respective echoes. The exact (convergent) results exhibit a slight disagreement with the lowest order approximation as the cluster expansion nears the point of its divergence.

As with Eqs. (6.26) and (6.28), the above equations may serve as a useful educated guess (estimate) at times beyond cluster expansion convergence. Initially, at least, Figs. (6.20) and (6.21) show that Eqs. (6.29) and (6.31) provide conservative estimates. If we do extrapolate these equations and define T_2 as the time in which the extrapolated echo reaches $1/e$, then we have, for natural Si, $T_2 = \nu^{0.67} \times 12$ ms for even CPMG echoes. For a small number of pulses, $\nu \sim 1$, this gives about factor of 5 increase of nuclear spin coherence times relative to the electron spin quantum dot coherence times reported in Ref. [42] and Sec. 6.3; this comparison factor increases as we increase the number of pulses because electron spin decay-time [42] scales with a smaller power of ν ($\nu^{0.53}$). In the range of cluster convergence, where we have confidence in the accuracy of our results for the model that we have used, we observe high fidelity memory retention with a low loss of 10^{-6} up to $1-2$ ms for two or four-pulse CPMG sequences in natural Si and nearly up to 4 ms for 1% purified Si.

By implementing CPMG pulse sequences with just a few even number of pulses, high fidelity (with loss below 10^{-6}) qubit retention times are theoretically observed on the order of 100 μs for GaAs systems and on the order of milliseconds for Si:P systems. We emphasize that although we are unable to achieve convergence beyond the initial decay which affects the accuracy of our extrapolated estimate for T_2, itself, we accurately estimate the initial-time coherent memory loss (i.e., the loss of the first $10^{-4} - 10^{-6}$ fraction of coherence) which is the most important ingredient for quantum computation considerations.

Chapter 7

Conclusion

In conclusion, we describe a quantum approach for the decoherence problem of a solid-state spin qubit in a nuclear spin bath and have studied the effects of concatenated and periodic dynamical decoupling pulse sequence both numerically and by classifying them perturbatively. In contrast to former theories, our method requires no *ad hoc* stochastic assumption on the complex dynamics of the environment responsible for decoherence. Hence it provides an important example where direct integration of the environmental equations of motion provides a systematic understanding of the loss of coherence which needs to be controlled for quantum information applications.

The most important theoretical accomplishment of our work is the development of the first *fully quantum microscopic* theory for the localized electron spin decoherence due to the spectral diffusion induced by nuclear spin bath dynamics. Our results are formally exact, and our numerical calculations, when the cluster expansion is convergent, provide an essentially exact quantitative description of the echo decay for various pulse sequences in various systems. The significance of our quantum theory lies in the fact that, unlike all other theoretical descriptions of SD spanning the last 50 years, we do not make any *ad hoc* phenomenological stochastic approximation in dealing with the non-Markovian spin dynamics in the

SD phenomena. We solve the problem essentially exactly using a quantum cluster decomposition technique, which is then theoretically justified by carrying out calculations to higher orders and tested further by comparing results from the time and intra-bath perturbation theories. A completely independent verification of our theory and results in the lowest order (the pair approximation) now appears in the literature [40, 43]. A linked-cluster expansion using a diagrammatic approach has also been developed [45] as an equivalent to our cluster expansion; the diagrammatic approach offers additional insight into the processes that cause decoherence but requires separate analyses for each of the many processes that are automatically incorporated into our cluster expansion.

7.1 Discussion

We compare the effects of periodic (PDD) versus concatenated (CDD) dynamical decoupling pulse sequences that are based upon the simple Hahn echo. We show that CDD results in successive low-order cancellations of both the time and intra-bath perturbations (one or both of these are generally applicable where the cluster expansion is convergent); for this reason, concatenated sequences far exceed the performance of periodic pulse sequence in maintaining qubit coherence. Our calculations show that increasing repetitions of the PDD sequence will increase the overall coherence time over the entire sequence but comes at the price of needing to apply pulses more frequently. Increasing the level of concatenation, on the other hand, can have the effect of increasing the time between pulses that is needed in order to maintain coherence. Concatenated sequences do have their limitations, however, even with the ideal pulses studied in this work. For the systems we have investigated, it tends to only improve performance when the delay between pulses is short compared to the intra-bath interaction time-scale. Furthermore, each level of concatenation requires the inclusion of larger clusters in the cluster expansion; these larger clusters often dominate the decay and expedite the point of diminishing returns for CDD. Therefore, the pair approximation estimates [43] for the echo decay of CDD are overly optimistic.

Our numerical studies of spin bath decoherence provide important tests for DD strategies and take these strategies beyond the level of pure abstract formalism [14, 18] and small toy models [47]. We note that it is a gross oversimplification to characterize these decoherence problems by a simple T_2 time. Their decay is often not characterized by a simple exponential because the decoherence process is non-Markovian. Furthermore, the coherence time for a particular qubit-bath system will generally depend upon the implemented DD strategy in non-trivial ways. It is traditional to define T_2 as the characteristic decay time of the Hahn echo in order to distinguish it from the time-scale of inhomogeneous broadening, T_2^*, when measuring an ensemble of qubits; however, it is more appropriate to define the T_2 time with respect to the free induction decay (free evolution decoherence of a single qubit with no inhomogeneous broadening) which is dominated by HF-mediated interactions [40]. In this work, we only consider the echo decay for various DD pulse sequences (including the Hahn echo) where the effects of HF-mediated interactions are at least partially reversed. We can broadly define T_2 as the total sequence time, for a given pulse sequence, at which the echo decay reaches a value of $1/e$ (or the time at which an extrapolation of the short time behavior reaches $1/e$). Using this definition, we find the Hahn echo T_2 to be about 100 μs for the Si:P system and about 10 μs for the GaAs quantum dot system. But, this T_2 can be enhanced indefinitely (up to tens of milliseconds) in the Si:P system through the isotopic purification of Si (i.e., by removing ^{29}Si nuclei from the system) whereas in the GaAs quantum dots, $T_2 \sim 10$ μs is essentially an absolute upper limit (when using simple Hahn echo refocusing) since *all* Ga and As nuclei isotopes have free spins contributing to the spectral diffusion and isotopic purification is impossible. It is important to emphasize here that although spin polarizing the nuclei (e.g., through the dynamic nuclear polarization technique) would, in principle, suppress the nuclear induced SD decoherence of electron spin, in practice, this would lead only to rather small enhancement of electron spin coherence since the presence of even a few nuclei with the "wrong" spin would cause nuclear pair flip-flop processes [82]. Nuclear spins have much longer coherence times than the those of localized electrons. We find the Hahn echo T_2 to be about 1 ms for a P donor in both Si and GaAs.

Finally, we comment on the fact that the SD process is quite a generic and general phenomenon in *any* spin decoherence problem with coupled spin dynamics (e.g. electron and nuclear spins, different types of nuclear spins, etc.) where the dynamics of one spin species has nontrivial (i.e., non-Markovian) temporal effects on the evolution of the spin dynamics of the other species. For example, a trivial (but not often emphasized in the literature) consequence of SD consideration is that in systems (e.g., Si:P; GaAs quantum dots) of interest to quantum computer architectures, the single flip of the localized electron spin will immediately decohere *all* the nuclear spins in its vicinity. Thus, the nuclear spin T_2 time in these systems can at most be the T_1 time for the electron spin! The typical low-temperature T_1 time for electron spins in the GaAs quantum dots has been measured to be 1 ms or so, and therefore the nucleus spin T_2 time would at most be 1 ms in the GaAs quantum dots, at least in the neighborhood of the localized electrons in the dot. The same consideration applies to the Si:P system. We believe that the general quantum theoretical techniques developed in this paper will be helpful in the studies of the temporal dynamics of other coupled spin systems wherever one spin species could act as a "decoherence bath" for the other system.

7.2 Future Work

This work could be extended in a number of different ways. Our methods can easily be applied to a variety of physical systems. Models could be improved to give a more accurate account of the various interactions in physical systems of interest. It is trivial to include any local, qubit-independent, intra-bath interactions (such as the dipolar or the indirect exchange interactions). However, the HF-mediated interaction, which is long-ranged and is a qubit-bath as well as intra-bath interaction, may require a more appropriate treatment. This interaction does not pose any problem for our cluster decomposition or the cluster expansion in principle, but it complicates our perturbative descriptions and computations because it is not compatible with a near neighbor approximation. The HF-mediated interaction has been included in a pair approximation for free induction decay [40] where it was found to be the dominant cause of decoherence; apart from a typically small visibility loss, the effect of the HF-mediated interaction is completely reversed in the pair approximation. On the other hand, because it is necessary to consider higher-order clusters in CDD sequences, it may be necessary to treat these interactions in order to more accurately test the DD enhancement gained from concatenation.

Our techniques could also be used to examine other promising pulse sequences. For example, Ref. [83] presents a sequence of π-pulses that gives optimal decoupling from a bosonic bath in a simple model; in the context of the solid-state spin baths that we study in this work, this particular sequence could simply be tested using our formalism (easily adaptable to any π-pulse sequence) or one could search for an optimized sequence that would suppress the cluster contributions of our cluster expansion. Finally, it would be desirable to adapt our formalism to treat non-ideal π-pulses (such as a perturbation to treat finite-width pulses), other types of pulses, or generally circumvent the restriction of treating only dephasing-type interactions of the qubit (i.e., make it possible to treat $\hat{S}_{x,y}$ as well as $\hat{S}_z$ qubit spin operators).

This work has made it possible to study the decoherence of a solid-state qubit interacting with a large, complex, dynamical spin bath using a microscopic approach that is formally exact and fully quantum mechanical. It is quite general but has some limitations (in particular, we can only treat dephasing-type interactions with the qubit and we must assume that the bath is initially uncorrelated). Our work holds promise to greatly benefit the study of quantum information in solid-state spin systems (or perhaps may be extended to other areas), and provides a starting place for future work to go beyond the limitations of this formalism.

Bibliography

[1] I. Zutic, J. Fabian, and S. Das Sarma, Rev. Mod. Phys. **76**, 323 (2004).

[2] P.W. Shor, Phys. Rev. A **52**, R2493 (1995); A.M. Steane, Phys. Rev. Lett. **77**, 793 (1996).

[3] J. Preskill, Proc. Roy. Soc. Lond. A **454**, 385 (1998); P. Aliferis, D. Gottesman, and J. Preskill, Quant. Information and Computation **6**, 97 (2006); K.M. Svore, D.P. DiVincenzo, and B.M. Terhal, quant-ph/0604090 (2006); T. Szkopek *et al.*, IEEE Trans. Nano. **5**, 42 (2006); D. Gottesman, quant-ph/0701112 (2007).

[4] M.A. Nielsen and I.L. Chuang, chapters 2, 4, and 8 in *Quantum Computation and Quantum Information* (Cambridge University Press, Cambridge, U.K., 2000).

[5] R. Raussendorf and H.J. Briegel, Phys. Rev. Lett. **86**, 5188 - 5191 (2001)

[6] P.W. Shor, Siam. J. Comput. 26 1484-1509 (1997).

[7] L. Grover, Proceedings, 28th Annual ACM Symposium on the Theory of Computing (STOC), May 1996, pages 212-219.

[8] R.P. Feynman, Int. J. Theor. Phys. **21**, 467, 1982.

[9] S. Hallgren, Proc. 34th ACM Symposium on Theory of Computing, 653 (2002); S. Hallgren, Proc. 37th ACM Symposium on Theory of Computing, 468 (2005); A. Schmidt and U. Vollmer, Proc. 37th ACM Symposium on Theory of Computing, 475 (2005); Y. Inui, F.L. Gall, quant-ph/0412033 (2004); C.M.M. Cosme and R. Portugal, quant-ph/0703223 (2007); T. Decker and P. Wocjan, quant-ph/0703195 (2007).

[10] X. Hu, R. de Sousa, and S. Das Sarma, cond-mat/0108339 (2001).

[11] U. Haeberle and J. Waugh, Phys. Rev. **175**, 453 (1968).

[12] W. Rhim, A. Pines, and J. Waugh, Phys. Rev. Lett. **25**, 218 (1970).

[13] L.M.K. Vandersypen and I.L. Chuang, Reviews of Modern Physics, **76**, 1037 (2004).

[14] L. Viola and S. Lloyd, Phys. Rev. A **58**, 2733 (1998).

[15] L. Viola, E. Knill, and S. Lloyd, Phys. Rev. Lett. **82**, 2417 (1999).

[16] Lian-Ao Wu, M.S. Byrd, and D.A. Lidar, Phys. Rev. Lett. **89**, 127901 (2002).

[17] L. Viola and E. Knill, Phys. Rev. Lett. **94**, 060502 (2005).

[18] K. Khodjasteh and D.A. Lidar, Phys. Rev. Lett. **95**, 180501 (2005).

[19] K. Khodjasteh and D.A. Lidar, quant-ph/0607086 (2006).

[20] O. Kern and G. Alber, Phys. Rev. Lett. **95**, 250501 (2005).

[21] M.S. Byrd, D.A. Lidar, Lian-Ao Wu, and P. Zanardi, Phys. Rev. A **71**, 052301 (2005).

[22] E.L. Hahn, Phys. Rev. **80**, 580 (1950).

[23] W. Magnus, Commun. Pure Appl. Math. **7**, 649 (1954).

[24] J.S. Waugh, L.M. Huber, and U. Haeberlen, Phys. Rev. Lett. **20**, 180 (1968).

[25] H.Y. Carr and E.M. Purcell, Phys. Rev. **94**, 630 (1954); S. Meiboom and D. Gill, Rev. Sci. Instrum. **29**, 6881 (1958).

[26] B.E. Kane, Nature (London) **393**, 133 (1998).

[27] A.J. Skinner, M.E. Davenport, B.E. Kane, Phys. Rev. Lett. 90, 087901 (2003); Xuedong Hu and S. Das Sarma, Phys. Stat. Sol. (b) **238**, 260 (2003); S. Das Sarma *et al.*, Solid State Communications **133**, 737 (2005); R. de Sousa, cond-mat/0610716 (2006).

[28] J.M. Taylor, C.M. Marcus, M.D. Lukin, Phys. Rev. Lett. **90**, 206803 (2003); Changxue Deng and Xuedong Hu, IEEE Trans. Nano. **4**, 35 (2005).

[29] B. Herzog and E.L. Hahn, Phys. Rev. **103**, 148 (1956); A.M. Portis, *ibid.* **104**, 584 (1956).

[30] G. Feher and E.A. Gere, Phys. Rev. **114**, 1245 (1959).

[31] W.B. Mims and K. Nassau, Bull. Am. Phys. Soc. **5**, 419 (1960); W.B. Mims, K. Nassau, and J.D. McGee, Phys. Rev. **123**, 2059 (1961).

[32] J.R. Klauder and P.W. Anderson, Phys. Rev. **125**, 912 (1962).

[33] G.M. Zhidomirov and K.M. Salikhov, Sov. Phys. JETP **29**, 1037 (1969).

[34] M. Chiba and A. Hirai, J. Phys. Soc. Jpn. **33**, 730 (1972).

[35] R. de Sousa and S. Das Sarma, Phys. Rev. B **68**, 115322 (2003).

[36] A.M. Tyryshkin and S.A. Lyon (private communication); A.M. Tyryshkin, S.A. Lyon, A.V. Astashkin, and A.M. Raitsimring, Phys. Rev. B **68**, 193207 (2003); A.M. Tyryshkin, J.J.L. Morton, S.C. Benjamin, A. Ardavan, G.A.D. Briggs, J.W. Ager, S.A. Lyon, J. Phys.: Condens. Matter **18**, S783 (2006).

[37] E. Abe, K.M. Itoh, J. Isoya and S. Yamasaki, Phys. Rev. B **70**, 033204 (2004).

[38] J.R. Petta (private communication); J.R. Petta *et al.*, Science, **309**, 2180 (2005).

[39] W.M. Witzel, R. de Sousa, and S. Das Sarma, Phys. Rev. B **72**, 161306(R) (2005).

[40] Wang Yao, Ren-Bao Liu, and L. J. Sham, Phys. Rev. B **74**, 195301 (2006).

[41] W.M. Witzel and S. Das Sarma, Phys. Rev. B **74**, 035322 (2006).

[42] W.M. Witzel and S. Das Sarma, Phys. Rev. Lett. **98**, 077601 (2007).

[43] Wang Yao, Ren-Bao Liu, and L. J. Sham, Phys. Rev. Lett. **98**, 077602 (2007).

[44] Ren-Bao Liu, Wang Yao, and L. J. Sham, cond-mat/0703690 (2007).

[45] S. K. Saikin, Wang Yao, and L. J. Sham, cond-mat/0609105 (2006).

[46] R. de Sousa and S. Das Sarma, Phys. Rev. B **67**, 033301 (2003).

[47] Wenxian Zhang, V. V. Dobrovitski, Lea F. Santos, Lorenza Viola, B. N. Harmon, cond-mat/0701507 (2007); Wenxian Zhang, V. V. Dobrovitski, Lea F. Santos, Lorenza Viola, B. N. Harmon, cond-mat/0703453 (2007).

[48] W.M. Witzel and S. Das Sarma, cond-mat/0701480 (2007).

[49] W.M. Witzel and S. Das Sarma, in preparation.

[50] C.P. Slichter, *Principles of Magnetic Resonance*, 3rd ed. (Springer-Verlag, Berlin, 1990).

[51] J.L. Ivey and R. L. Mieher, Phys. Rev. B **11**, 849 (1975).

[52] J.-M. Jancu, R. Scholz, F. Beltram, and F. Bassani, Phys. Rev. B **57**, 6493 (1998).

[53] D. Klauser, W.A. Coish, and D. Loss, cond-mat/0604252, Adv. Solid State Phys. **46** (2006).

[54] C. Deng and X. Hu, Phys. Rev. B **73** 241303(R) (2006); C. Deng and X. Hu, cond-mat/0608544 (2006).

[55] N. Bloembergen and T.J. Rowland, Phys. Rev. **97**, 1679 (1955).

[56] N. Shenvi, R. de Sousa, and K.B. Whaley, Phys. Rev. B **71**, 224411 (2005).

[57] W.A. Coish and D. Loss, Phys. Rev. B **70**, 195340 (2004).

[58] P.W. Anderson, Phys. Rev. **99**, 623 (1955).

[59] R.F. Shulman, J.M. Mays, and D.W. McCall, Phys. Rev. **100**, 692 (1955).

[60] R.F. Shulman, B.J. Wyluda, and H.J. Hrostowski, Phys. Rev. **109**, 808 (1958).

[61] R.K. Sundfors, Phys. Rev. **185**, 458 (1969).

[62] C. Kittel, *Introduction to Solid State Physics*, 7th ed. (Wiley, New York, 1996).

[63] A. Abragam, *The Principles of Nuclear Magnetism* (Oxford University Press, London, 1961), Chap. IV, Eq. (63).

[64] E. Abe, A. Fujimoto, J. Isoya, S. Yamasaki and K.M. Itoh, cond-mat/0512404 (2005)

[65] W.B. Mims, Phys. Rev. B **5**, 2409 (1972).

[66] A. Schweiger and G. Jeschke, *Principle of Pulse Electron Paramagnetic Resonance* (Oxford University Press, Oxford, (2001).

[67] S.A. Dikanov and Y.D. Tsvetkov, *Electron Spin Echo Envelope Modulation (ESEEM) Spectroscopy* (CRC Press, Boca Raton, 1992).

[68] A. Ferretti, M. Fanciulli, A. Ponti, and A. Schweiger, Phys. Rev. B **72**, 235201 (2005).

[69] E.J. Reijerse and S.A. Dikanov, J. Chem. Phys. **95**, 836 (1991).

[70] W.M. Witzel, Xuedong Hu, S. Das Sarma, cond-mat/0701341 (2007).

[71] S. Saikin and L. Fedichkin, Phys. Rev. B **67**, 161302(R) (2003).

[72] D. Loss and D.P. DiVincenzo, Phys. Rev. A **57**, 120 (1998); D.P. DiVincenzo *et al.*, Nature (London) **408**, 339 (2000).

[73] J. Levy, Phys. Rev. Lett. **89**, 147902 (2002); D. Bacon, K.R. Brown, and K.B. Whaley, Phys. Rev. Lett. **87**, 247902 (2001); R. Hanson and G. Burkard, Phys. Rev. Lett. **98** 050502 (2007); Y.S. Weinstein and C.S. Hellberg, Phys. Rev. Lett. **98** 110501 (2007).

[74] J. M. Taylor, H.-A. Engel, W. Dur, A. Yacoby, C. M. Marcus, P. Zoller, and M. D. Lukin, Nature Physics **1**, 177 (2005).

[75] A.V. Khaetskii, D. Loss, and L. Glazman, Phys. Rev. Lett. **88**, 186802 (2002).

[76] Wenxian Zhang, V. V. Dobrovitski, K. A. Al-Hassanieh, E. Dagotto, and B. N. Harmon, Phys. Rev. B **74**, 205313 (2006).

[77] J.M. Taylor, M.D. Lukin, Quant. Inf. Proc. **5**, 503 (2006).

[78] *CRC Handbook of Chemistry and Physics*, 70th ed., E-82 (CRC Press, Boca Raton, FL, 1989).

[79] D. Paget, G. Lampel, B. Sapoval, and V.I. Safarov, Phys. Rev. B **15**, 5780 (1977).

[80] J.R. Petta *et al.*, Physica E **34**, 42 (2006); E. A. Laird, J. R. Petta, A. C. Johnson, C. M. Marcus, A. Yacoby, M. P. Hanson, and A. C. Gossard, cond-mat/0512077 (2005); J.M. Taylor, J.R. Petta, A.C. Johnson, A. Yacoby, C.M. Marcus, M.D. Lukin, cond-mat/0602470 (2006).

[81] W.M. Witzel and S. Das Sarma, in preparation.

[82] S. Das Sarma, Rogerio de Sousa, Xuedong Hu and Belita Koiller, Solid State Commun. **133**, 737 (2005).

[83] Götz S. Urig, Phys. Rev. Lett. **98**, 100504 (2007).